# PHOTONIC TOPOLOGICAL METAMATERIALS

by

BIAO YANG

A thesis submitted to the University of Birmingham for the degree of DOCTOR OF PHILOSOPHY

Metamaterials Research Centre

School of Physics & Astronomy

College of Engineering and Physical Sciences

University of Birmingham

October 2017

# Abstract

Topology, a mathematical concept associated with global perspectives, was found to represent geometric aspects of physics. To date, various topological phases have been proposed and classified. Among them, topological gapless phases focusing on the degeneracies of energy bands serving as the singularities in the momentum space, attract much attention. Especially in the three-dimension, various topological semimetals have been proposed. With unit topological charge ±1, Weyl degeneracies have laid the foundation. Also, they show loads of exotic properties, such as Fermi arcs and chiral anomalies. Being relied on the band topology theory, topological gapless phases have also been transferred into classic systems, such as photonics, acoustics and mechanics.

Here, we experimentally investigated photonic Weyl systems in the photonic continuum media, where electromagnetic intrinsic degrees of freedom play key roles in constructing the state space. Firstly, we researched chiral hyperbolic metamaterials, a type-II Weyl metamaterials, from which we directly observed topological surface-state arcs. Then, we report the discovery of ideal photonic Weyl systems, where helicoid structure of nontrivial surface states has been demonstrated. Finally, we construct photonic Dirac points, through analysing eigen reflection field, we found the correlation of topological charges in momentum and real spaces.

*Physics like iced latte*

*Bitter*

*Cold*

*And tasty*

*——to my family*

# Acknowledgement

First and foremost, I would thank my supervisor Shuang Zhang. He has been always very passionate and patient to teach me. From him I learned how to find and solve problems. No matter how complicated the physics is, he always tried to make it easy to understand. I also thank him for showing me this fantastic field – topological photonics. When I decided to continue my PhD four years ago, I have no ideal about topology and at that time topological photonics just emerged. During the four-year experience, he has offered me a very open and free environment so that I can focus on what I am interested in.

I would like to thank all group members from metamaterials research centre. Every day we have very enjoyable coffee time, and many interesting discussions on both physics and life. Especially, I want to thank Dr Mark Lawrence, he helped me a lot on the beginning study of topology physics and improving my English language. I also want to thank Prof Weimin Ye, Dr Qinghua Guo, Dr Wenlong Gao, Dr Hongchao Liu, Dr Mitchell Kenney, Dr Teun-Teun Kim, Dr Guixin Li, Dr Shiyi Xiao, Dr Fu Liu, Dr Shumei Chen, Dr Hongwei Jia, Dr Erchan Yang, Dr Wenhui Wang, Dr Changxu Liu, Dr Jensen Li, Dr Miguel Navarro-Cia, Mr Yaoting Wang, Mr Dongyang Wang, Mr Lingbo Xia, Mr Daniel Frese and Mr Lingxiao Zhu.

Collaboration with Dr Ben Tremain, Miss Lauren Barr and Prof Alastair Hibbins from University of Exeter is very smooth. I also thank them for supporting us in the near-field scanning measurement.

Finally, I want to acknowledge Chinese Scholarship Council and School of Physics & Astronomy for their financial supporting to make this possible.

# Selected publication list

[1] **Yang, B.**, Lawrence, M., Gao, W., Guo, Q. & Zhang, S. One-way helical electromagnetic wave propagation supported by magnetized plasma. Scientific Reports 6, 21461 (2016).

[2] **Yang, B.** et al. Direct observation of topological surface-state arcs in photonic metamaterials. Nature Communications 8, 97 (2017).

[3] **Yang, B.** et al. Discovery of ideal Weyl points with helicoid surface states. arXiv:1709.06065 [cond-mat.mtrl-sci] (2017).

[4] Guo, Q., **Yang, B.** et al. Three dimensional photonic Dirac points in metamaterials. Phys. Rev. Lett. 119, 213901 (2017).

# Contents

# List of Figures

# List of Abbreviations

| | |
|---|---|
| Chiral Hyperbolic Metamaterials | CHM |
| Double Hyperbolic Metamaterials | DHM |
| Equi-Frequency Contours | EFC |
| Topological Surface-state Arcs | TSA |
| Topological Surface-state Ellipsoid | TSE |
| Printed Circuit Board | PCB |
| Splitting Resonator Ring | SRR |
| Vector Network Analyzer | VNA |
| Perfect Electric Conductor | PEC |
| Left/Right Circular Polarization | LCP/RCP |
| Time-reversal Symmetry | T |
| Inversion Symmetry | P |
| First Brillouin Zone | FBZ |

# Chapter 1. Introduction to topological gapless phases

## 1.1 Topology and symmetry

*Topology*

In mathematics, topology is a branch concerned with the properties of objects that are insensitive under continuous transformation, such as stretching, crumpling and bending. There always exist integers used to characterize different classes of topological objects. The two simplest and intuitive examples are sphere and torus, as shown in ***Figure 1.1.*** The number of holes (genus), as the topological integer here, exhibits that they cannot be smoothly transformed into each other.

The well-known Gauss-Bonnet theorem,

$$\chi = \frac{1}{2\pi}\int_S KdA\,, \qquad [1\text{-}1]$$

with $K$ being the Gaussian curvature, $A$ being the area, shows the way how to calculate Euler Characteristic ( $\chi$ ), which is related to the genus ($g$) as,

$$\chi = 2 - 2g\,. \qquad [1\text{-}2]$$

For a surface of sphere with radius $R$, Euler characteristic is easily checked as,

$$\chi = \frac{1}{2\pi}\int_S KdA = \frac{1}{2\pi}\int_S \frac{1}{R^2}dA = 2\,. \qquad [1\text{-}3]$$

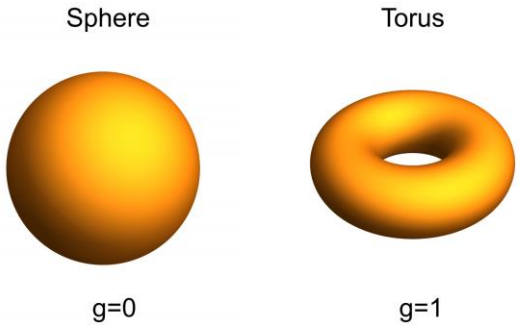


***Figure 1.1 The surfaces of a sphere (g=0) and a torus (g=1) are topologically distinct.***

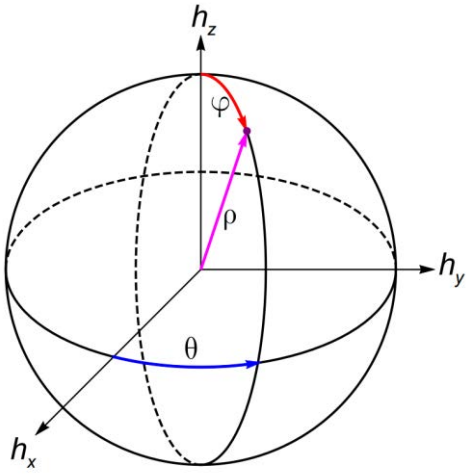


***Figure 1.2 Spherical coordinate.***

A more complicated case is the obstruction that one cannot define non-vanishing continuous tangent vector field on a two-dimension (*2D*) sphere - $S^2$, so called hairy ball theorem. If we work in a three-dimension (*3D*) spherical coordinate, as showed in

***Figure 1.2***, and define $\hat{\theta}$ as the tangent vector field, then the north pole and south pole are ill-defined. However, there is no such problem happens on the surface of torus, as shown in ***Figure 1.3***.

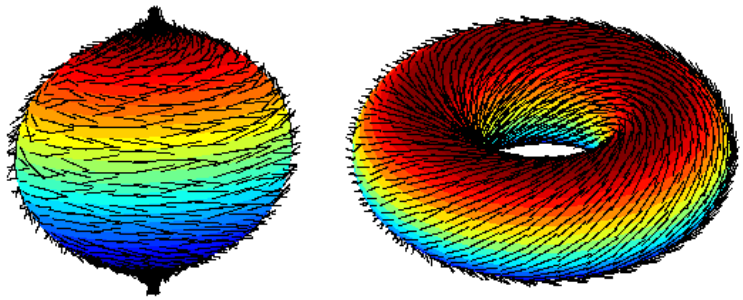

***Figure 1.3 A failed attempt to comb a hairy ball, leaving a tuft at each pole, on the other hand, a hairy doughnut (2-torus) is quite easily combable. [From wikipedia]***

In physical systems, topological invariant (similar to genus as mentioned above) measures the global phase structure of bulk wave functions [1-5], in which Bloch states behave like the tangent vector field as we mentioned above. For the $U(1)=\exp(i\phi)$ gauge, this relation is guaranteed by the isomorphism,

$$U(1) \simeq SO(2) \qquad [1\text{-}4]$$

Berry curvature works similarly as the Gaussian curvature. Physicists have transferred the curvature concepts from Euclidean space into abstract Hilbert space, on which topological band theory was built. The Berry curvature is defined as an anti-symmetric second-rank tensor derived from the Berry connection $A$ via,

$$\Omega_{n,\mu\upsilon}(R)=\frac{\partial}{\partial R^{\mu}}A_{n,\upsilon}(R)-\frac{\partial}{\partial R^{\upsilon}}A_{n,\mu}(R) \qquad [1\text{-}5]$$

where, $n$ is the band number and $R^{j}$ with $j=\mu,\nu$ is the coordinate of parameter space.

In differential geometry, the Berry curvature is a two-form after exterior derivative of the one-form Berry connection, $\Omega=dA$. When considering the momentum space as the parameter space, the Berry curvature is odd under time-reversal symmetry $\Omega(\vec{k})=-\Omega(-\vec{k})$ while even under inversion symmetry $\Omega(\vec{k})=\Omega(-\vec{k})$. Obviously, if both symmetries are present, Berry curvature vanishes everywhere.

*Symmetry*

Symmetry transformations are the foundation for the fundamental theories of modern physics. In the topological phase researching, most of them are symmetry protected or demanded. For example, time reversal symmetry protection plays the key role in the discovery of *2D/3D* topological insulator through Kramers double degeneracy theorem [6-8], while the realization of Weyl semimetal phase demands for either breaking time reversal/ inversion symmetry. According to the symmetry representation theorem by Wigner [4], any symmetry transformation in quantum mechanics can be represented on the Hilbert space by an operator that is either unitary, or anti-unitary. For example, when operating on the imaginary unit $i=\sqrt{-1}$, unitary operator acts like $TiT^{-1}=i$ while for

anti-unitary one $TiT^{-1} = -i$ . Both time-reversal and particle-hole symmetry are anti-unitary. The other symmetries, such as crystalline symmetry, are unitary. In condensed solids, totally there are *230* space groups, *73* of them are the product groups of point groups and translation groups, called symmorphic groups. The rest groups (*230-73=157*) are nonsymmorphic, consisting of two operations: glide mirror and screw rotation. Nonsymmorphic groups have attracted much attention in the topological phase seeking because they always support high even-dimension degeneracy [9]. Generally, there are three types of degeneracy [10], which can be classified as:

1. The first type of degeneracy is due to the non-commutation relation between symmetry operations, which leads to the presence of high order degeneracy.

2. The second type of degeneracy occurs for the eigenstates belonging to different irreducible representation of a symmetry group.

3. The third type of degeneracy originates from the anti-unitary symmetry operators.

Note that unitary symmetries, which commute with the Hamiltonian, allow us to bring the Hamiltonian into a block diagonal form. So far, with classifying the symmetry properties of these irreducible blocks, which do not exhibit any unitary symmetries, there are ten classes with considering the following set of discrete symmetries [4]:

$$\begin{array}{llll} \textit{time-reveresal} & T^{-1}HT = H & T = U_T K & U_T U_T^* = \pm 1 \\ \textit{particle-hole} & C^{-1}HC = -H & C = U_C K & U_C U_C^* = \pm 1 \\ \textit{chiral} & S^{-1}HS = -H & S = U_S & U_S^2 = 1 \end{array} \qquad [1\text{-}6]$$

where $K$ is the complex conjugation operator. As it turns out, this set of symmetries is exhaustive. Chiral symmetry (the product $S = T \cdot C$), however, corresponds to a unitary symmetry operation for the single particle Hamiltonian $H$. But in this case, the unitary symmetry $U_T \cdot U_C^*$ does not commute, but anti-commutes with $H$. Generally, internal symmetries, including time-reversal symmetry, particle-hole and chiral symmetry, are more stable. Hence, the assumption of translation invariance is not at all necessary for those topological gapped phases classified into the ten *AS* (Altland and Zirnbauer) symmetry classes [11]. However, topological gapless phases, to some extent, are protected by translation symmetries. Because those topological chargers usually are separately located in the momentum space, the distances between them should be good quantum numbers, which ask for translation symmetry.

Interplay between symmetry and topology lays the foundation of symmetry protected topological phases.

## 1.2 Topological gapless phases

Weyl points are the momentum space counterparts of magnetic monopoles defined in real space. As mentioned before, Dirac points can decouple into two Weyl points, one of them behaves like source of Berry flux and the other is the sink. Away from the Weyl point, energy band has linear/conical dispersion along all directions (as shown in ***Figure*** 1.4). As a very simple nontrivial continuum model, Weyl Hamiltonian can be written as,

$$H=h_x\sigma_x+h_y\sigma_y+h_z\sigma_z \qquad [1\text{-}7]$$

where $\sigma_{x,y,z}$ are three traceless Pauli matrices.

Its energy dispersion is $E_\pm=\pm\left|\vec{h}\right|$. Without loss of generality, when $E=h_r$, the equi-frequency contour is a sphere with radius of $h_r$.

The eigenstates are [12],

$$\left|u_-\right\rangle=\begin{bmatrix}-\sin\left(\frac{\varphi}{2}\right)e^{-i\theta}\\ \cos\left(\frac{\varphi}{2}\right)\end{bmatrix},\left|u_+\right\rangle=\begin{bmatrix}\cos\left(\frac{\varphi}{2}\right)e^{-i\theta}\\ \sin\left(\frac{\varphi}{2}\right)\end{bmatrix} \qquad [1\text{-}8]$$

where we used the spherical coordinate defined as,

$$\begin{cases}h_x=\rho\sin\varphi\cos\theta\\ h_y=\rho\sin\varphi\sin\theta\\ h_z=\rho\cos\varphi\end{cases} \qquad [1\text{-}9]$$

We choose an open covering $\left(U_N,U_S\right)$ of the sphere, where two open sets are the north hemisphere $U_N$ and south hemisphere $U_S$. The intersection being $U_N\bigcap U_S$ can be reduced to a circle. We define local trivializations of the filled band bundle by,

$$\left|u_{-,N}\right\rangle=\begin{bmatrix}-\sin\left(\frac{\varphi}{2}\right)e^{-i\theta}\\ \cos\left(\frac{\varphi}{2}\right)\end{bmatrix},\left|u_{-,S}\right\rangle=\begin{bmatrix}-\sin\left(\frac{\varphi}{2}\right)\\ \cos\left(\frac{\varphi}{2}\right)e^{i\theta}\end{bmatrix} \qquad [1\text{-}10]$$

Obviously, $\left|u_{-,N}\right\rangle$ is ill-defined on the south point, where $\left|u_{-,N}\right\rangle=\begin{bmatrix}-e^{-i\theta} & 0\end{bmatrix}^T$ and $e^{-i\theta}$ can be arbitrary.

On the equator Berry connection can be defined as,

$$A=i\left\langle u_{-,N}\right|\frac{d}{d\theta}\left|u_{-,N}\right\rangle=\frac{1}{2} \qquad [1\text{-}11]$$

Integrating along the equator one can obtain Berry phase,

$$\gamma=\oint_{equator}\frac{1}{2}d\theta=\pi \qquad [1\text{-}12]$$

Intuitively, the nontrivial topological phase as a Mobius strip is shown in ***Figure 1.4***. After travelling along the black lane $2\pi$, one meets the cyan lane rather than the black one, which corresponds to the extra $\pi$ phase accumulated. In contrast, after $4\pi$ rotation, one arrives at the original point. Most of exotic observables related to the topological phases arise from the fundamental properties. Globally, the total Berry flux is $2\pi$ . The corresponding topological invariant/chirality is 1, so called Chern number defined in the momentum space.

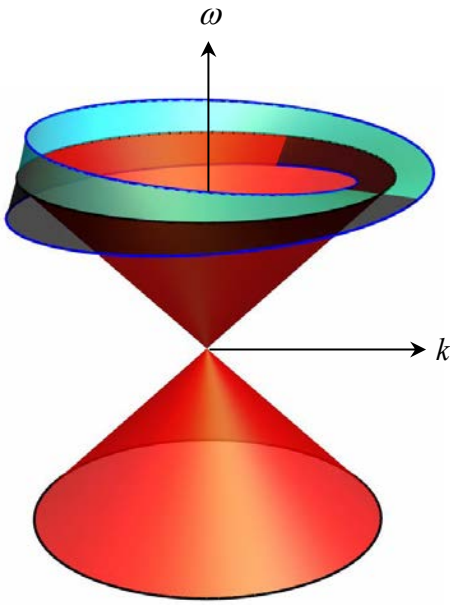


***Figure 1.4 Weyl dispersion and Möbius-highway describing nontrivial topological phase.***

For a general Weyl Hamiltonian taking the form like,

$$H\left(\vec{k}\right)=\sum k_i v_{ij}\sigma_j \qquad [1\text{-}13]$$

where $i,j\in\{x,y,z\}$ and $v_{ij}$ are the group velocities. Topological charge here is $c=\mathrm{sgn}\left[\det\left(v_{ij}\right)\right]=\pm 1$.

When one consider the $\vec{h}=\left(h_x,h_y,h_z\right)$ parameter as magnetic field $\vec{B}=\left(B_x,B_y,B_z\right)$, the case describes single spinful electron in magnetic field [1]. For spin-*1* particle, such as photon, we can define the eigenmodes as left/right circular polarized,

$$\vec{E}_{R/L}=\vec{E}_{\varphi}\pm i\vec{E}_{\theta}=\frac{1}{\sqrt{2}}\left(\hat{\varphi}\pm i\hat{\theta}\right) \qquad [1\text{-}14]$$

Similar calculation shows us Berry curvature $\Omega = \vec{h} \Big/ \left|\vec{h}\right|^3$ with topological charge being $\pm 2$.

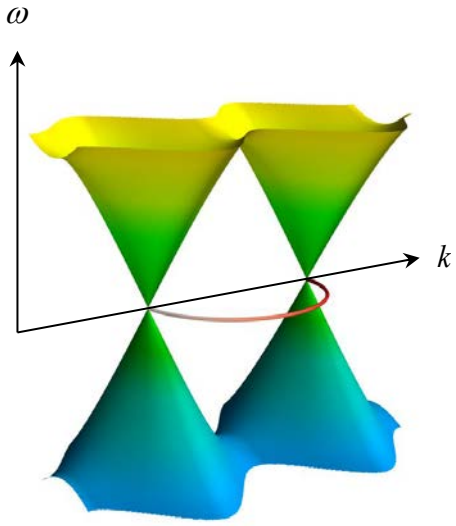


***Figure 1.5 Weyl points and Fermi arcs.***

On the surface of a Weyl system, there existing surface states taking form of Fermi arcs connecting two projections of opposite Weyl points as shown in ***Figure 1.5*** [5,13-15]. Under continuous transformation, two compensated Weyl nodes emerge to be a Dirac point in three-dimension space. And, Dirac points bridge gapless and gapped topological phases [5].

## 1.3 Topological photonics

In 2005, Haldane and Raghu [16,17] proposed the possible realization of topological phases in photonic system. Then, the research group [18,19] from MIT experimentally observed one-way electromagnetic wave propagation with applying an external magnetic field. Since then, topological photonics emerged and attracted great deal of

attentions [20]. In the two-dimension photonics, apart from the photonic integer quantum Hall effect [21], photonic topological insulators have also been proposed [22-24] and experimentally observed [25,26].

Soon after, three-dimension topological photonics arises. Photonic Weyl system has been realized in gyroid photonic crystals [27,28], where a triple degeneracy splits into two/four Weyl points with breaking time-reversal symmetry/inversion symmetry. Weyl points are also proposed in other photonic crystals [29,30]. Especially in optical band [31], laser written waveguide array supports type-II Weyl points, which show strong resemblance to Floquet photonic topological insulator [32]. Within metamaterial approach [33-35], topological surface-state arcs have been directly observed [36].

Based on spatial symmetries, three-dimension photonic Dirac points are proposed [37,38]. In the nonsymmorphic crystals, it is easy to find even order degeneracies on the Brillouin zone boundary, thus where Dirac points exist. From electromagnetic intrinsic degrees of freedom, three-dimension photonic Dirac points are also proposed in metamaterials [39], where two longitudinal modes and two transverse modes construct four-dimension state space. The other topological gapless phases include double Weyl points [15], spin-*1* Weyl points [40,41] and nodal line [42].

Three-dimension photonic topological gapped phases are also proposed. With breaking time-reversal symmetry, single Dirac cone surface state is found to exist in a photonic topological crystalline insulator [43] protected by glide mirror symmetry. Under

electromagnetic duality symmetry, three-dimension photonic topological insulator is proposed [44]. However, the underlying physics and corresponding experimental observations are still open questions [45,46].

Topological photonics has paved a new way regarding on the electromagnetic wave manipulation and novel photonic device design. With scattering-immune one way energy transport supported by surface/edge states, topological photonics is very promising in the application of information processing, imaging systems and near-field sensing.

In this thesis, we present the realization of photonic gapless phases in metamaterials. The outline of the thesis is as follows. *Chapter 2* [36] reports the direct observation of photonic topological surface-state arcs in a chiral hyperbolic metamaterial. Furthermore, we demonstrate the topological surface wave propagates down a three-dimension step without any back-scattering. In *chapter 3* [47], ideal photonic Weyl systems are presented. With perfect band representation, ideal Weyl system offers a clean platform regarding on more fundamental exotic properties, such as helicoid structure of topological surface states. *Chapter 4* [39] shows the construction of three dimension photonic Dirac points based on electromagnetic intrinsic degrees of freedom, where we found the relation of topological charges in momentum and real spaces.

# Chapter 2. Observation of photonic topological surface-state arcs in type-II Weyl metamaterials

The discovery of topological phases introduces new perspectives and platforms for the study of fundamental quasi-particles, such as Dirac [48], Majorana [49] and Weyl fermions [50,51], in condensed matter physics. However, nontrivial surface states arcs, as characteristic topological features, playing an important role in identifying Dirac and Weyl semimetals, have not yet been observed in classical systems. In this chapter, with designing photonic Weyl metamaterials and using near-field scanning measurements, we report the direct observation of a photonic analogue to Fermi arcs connecting topologically distinct bulk states in chiral hyperbolic metamaterials. Furthermore, we demonstrate backscattering-immune transport of nontrivial surface states acrossing a physical step. Our work paves the way to achieve 'Fermi arcs' (surface state arcs in Weyl systems) in topological photonics and offers a deeper understanding of topological gapless phases in classical systems. This chapter includes passages from the publication [36].

## 2.1 Introduction

Topology, describing properties of classes of systems that are invariant under continuous smooth transformations, was found to govern macroscopic physics since the discovery of Integer Quantum Hall Effect [52]. From then on, topologically ordered matters including topological insulators and superconductors [2,3], Dirac semimetals [48,53] and Weyl semimetals [13,14,50,51] have appeared and attracted much attention due to their exotic properties. Weyl semimetals exhibiting conical dispersion along arbitrary direction can be further classified into type-I [13] and type-II [54] with respect of keeping Lorentz symmetry or not. In type-I Weyl semimetal, Weyl point occurs at the Fermi level resulting in a point-like Fermi surface. In the type II Weyl semimetals, which has been intensely researched very recently, the Weyl point emerges from a contact of an electron and a hole pocket at the boundary resulting in a highly tilted Weyl cone (***Figure 2.1***a and b), and related Fermi surface undergoes a Lifshitz transition, giving rise to a new kind of chiral anomaly and other new physics. Around both Weyl points, they unveil a linear dispersion relation in all three momentum space directions, which can be described by the reduced two-component massless Weyl equation. At Weyl points, the bands are doubly degenerate, thus the Berry connection and Berry curvature are ill-defined, where Weyl nodes behave like sources/sinks of quantized Berry flux in momentum space. Integration of Berry curvature around one of the Weyl

nodes gives its topological charge which protects the stability of Weyl semimetals. If both time reversal symmetry and inversion symmetry are present, the stability will lose due to two Weyl points with opposite topological charges merge each other and the Berry curvature integration vanishes. The sum of topological charges for a whole system must be zero to satisfy gauge invariance, due to the Nielsen-Ninomiya theorem [55].

On the boundary of a bulk sample, there are gapless surface states being protected by chiral topological charge associated with the Weyl nodes, or bulk-surface correspondence. These surface states, taking the form of Fermi arcs connecting the projection of bulk Weyl nodes on the surface, show characteristic signatures of topological order of Weyl semimetal. In condensed matter, several groups have reported experimental observation of Fermi arcs through angle-resolved photoemission spectroscopy (ARPES) measurement for both types of Weyl points [50,51,56]. However, Fermi arcs have not yet been experimentally verified in photonics. Even point degeneracy of photonic type-I Weyl semimetal was seen by microwave angle-resolved transmission measurement in double gyroid photonic crystal consisting of layered slabs of ceramic-filled plastics with drilled periodic holes along three mutual-orthogonal directions [28].

In this chapter, we report experimentally observed evidences on photonic Fermi arcs and the identification of photonic Type II Weyl phases. Finally, real space

electromagnetic field propagation along a cuboid configuration will visually show robustness of topological phase, for the first time we see somethings which are difficult to realize in other systems. Different from angle-resolved photoemission spectroscopy (ARPES), the method mainly used here is near field scanning by using microwave xyz-stage and vector network analyzer (VNA). With high resolution of band structure retrieving from Fourier transformation, near field scanning shows great potential in the future topological matter research. It is advantageous in resolving multiple fine band structure details because of its very dense momentum coverage. Working at photonic system has another merit. Weyl nodes do not need to locate nearly at the 'chemical potential', optical frequency can be adjusted easily to find the Weyl frequency.

## 2.2 Design of chiral hyperbolic metamaterials

In order to obtain a Weyl semimetal, and to be able to probe this accordingly, either time-reversal symmetry or inversion symmetry have to be broken. In classic electromagnetic realm, it is more feasible to break inversion symmetry instead of time-reversal symmetry to avoid using lossy magnetic materials and external magnetic field [21]. Chiral hyperbolic metamaterials with breaking inversion symmetry represents one of the first candidates for the experimental realization of a photonic type-II Weyl phases [33,35].

Under $\omega_0 = 1/3, A = 1, l = 1, L = 3, \alpha = l/L, \beta = A/L, a = b = 0.2$ as defined in ***section***

*2.7*, it is characterized by very simple band structures with two nontrivial type-II Weyl points, which are related to each other with time reversal symmetry owning the same chirality (***Figure 2.1***c, W1s). Their partners with opposite chirality are located at a lower frequency (***Figure 2.1***c, W2s). In addition, chiral hyperbolic metamaterials also shows the possibility of topological phase transitions realized through delicate tuning of the non-local effect [35]. The intermediate topological phase between type-I and type-II Weyl degeneracies has been proposed in magnetized plasma by breaking time reversal symmetry [34,57].

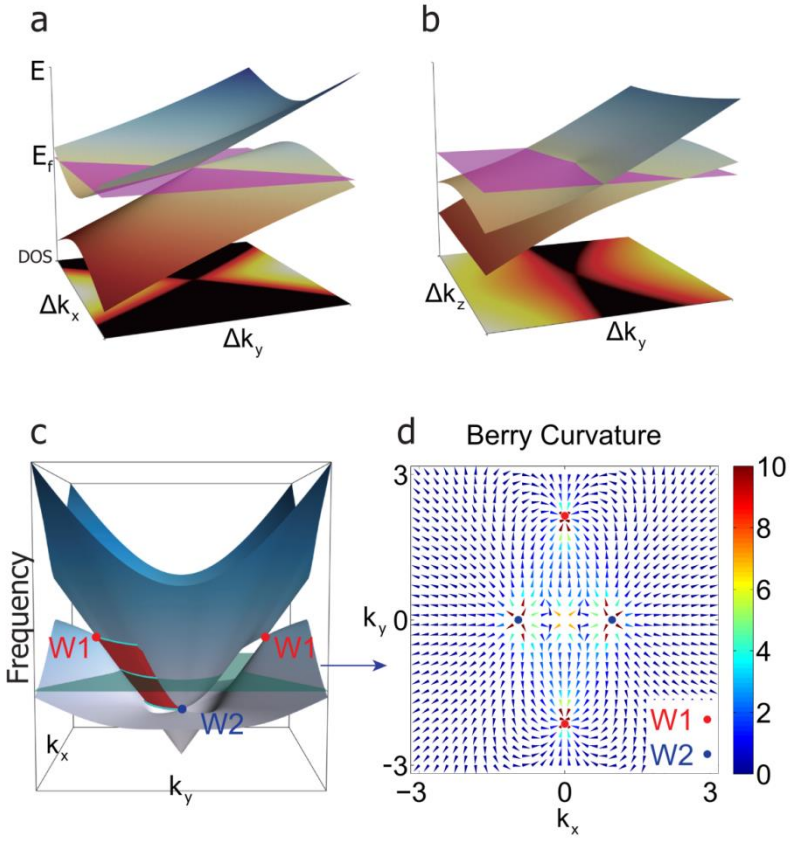


***Figure 2.1Bulk and surface states in chiral hyperbolic metamaterials (CHM).[36]***

Schematic view of energy dispersion near Type-II Weyl point for CHM with respect to (a) *x*-*y* and (b) *y*-*z* momentum space. Bottom planes show momentum resolved Density of States (DOS) at the 'Fermi energy' EF, and EF indicated by a purple plane. (c) Effectively modelled band structures of bulk ($7^{th}$ and $8^{th}$ bands) and surface states for the CHM. Red spots W1 indicate one pair of type-II Weyl points. Blue spots W2 (one is hidden) are the chiral partners of the red ones W1. One surface state between two topological partners is indicated by the red surface, upon which the cyan lines highlight 'Fermi arcs' at three different frequencies. The other surface state, which is not plotted, can be obtained after time reversal operation of the present one. (d) Berry curvature calculated for the $7^{th}$ band from effectively modelled Hamiltonian. W1s serve as two sources while W2 are two sinks. All units are arbitrary units. Simulated band with realistic structure is shown in ***Figure 2.2***.

When studying the existence of Weyl points (degeneracies) in computation, a degenerate point might turn out to be separated with a tinier gap upon increasing computational precision (such as mesh size or step size in CST microwave studio software). However, Berry curvature does not sensitively depend on the computational precision; singularities always show up as long as bands are nontrivially degenerate, as showed in ***Figure 2.1***d for the $7^{th}$ band. Clearly, we can see four Weyl points behaving as sources/sinks of Berry flux, in which W1s are a pairs of type-II Weyl points. W2s, separated by nontrivial gaps, serve as chiral partners of W1s.

We have designed chiral hyperbolic metamaterials constructed from layer-stacking of the two-dimensional meta-structure sheets along the *z*-axis, where each sheet is made of three different layers as shown in ***Figure 2.2***a and b (each layer has 75 unit cells). The layered structure and low operating frequency (at 5 - 10GHz) greatly facilitates the fabrication of sample. Deep-subwavelength property of metamaterials makes the

sample-assembly more robust against slight misalignment. It also enables the possibility of near field scanning on the surfaces with less electromagnetic field localization in each unit cell. In our experiment, the scan step is set as 2mm which is half of length of cubic unit cell ($4mm^3$). Thus each unit cell works as electromagnetic 'atoms', the average effect of these 'atoms' is measured, which is the key spirit of metamaterials.

To realize hyperbolic feature of this chiral hyperbolic metamaterials, metallic wires are arranged along *y* direction (as shown in ***Figure 2.2***a). The attached metallic crosses contribute to increasing local capacitances and resonances, thus suppressing strong non-local effect induced by metallic wires [58]. We also make sure the metallic wires narrow enough, close to PCB fabrication limit (width is 200um), to increase the inductance and further blocking non-local effect. All these efforts together show us slightly tilted longitudinal mode dispersion curve (see ***Figure 2.2***e). This hyperbolic layer singly behaves as an anisotropic hyperbolic metamaterials. We use metallic coils (inductors) to break inversion symmetry. They are designed along *x* direction with 2.5 turns (***Figure 2.2***a). Because of the finitude of turns, a little bit bi-anisotropic effect, which will slightly shift the Weyl points away from *y* axis (***Figure 2.2***d) without gapping Weyl degeneracies, is inevitably induced [59]. In other words, electric fields along *x* direction can excite magnetic fields not just along *x* direction, vice versa. However, Weyl points are still located on $k_z=0$ which is protected both by time-reversal and $C_2$ rotation symmetry along *z* direction. The length and helical area of the springs, which

are tightly related to the resonance frequency, have been optimized for experimental purpose. ***Figure 2.2***a shows unit cell of chiral hyperbolic metamaterials as we described above, which is assumed to be periodically buried in a background materials-FR4 with dielectric constant of 4.1. Thickness of copper layer is 35um and copper can be regarded as perfect electric conductor (PEC) in the operating frequency range, which ideally means the system is lossless. ***Figure 2.2***b shows sample fabricated with traditional printed circuit board (PCB) technology. There is a 1mm-thick-blank FR4 layer between the chiral-layer and hyperbolic layer to avoid shorting-contact between inter-layer-metallic structures.

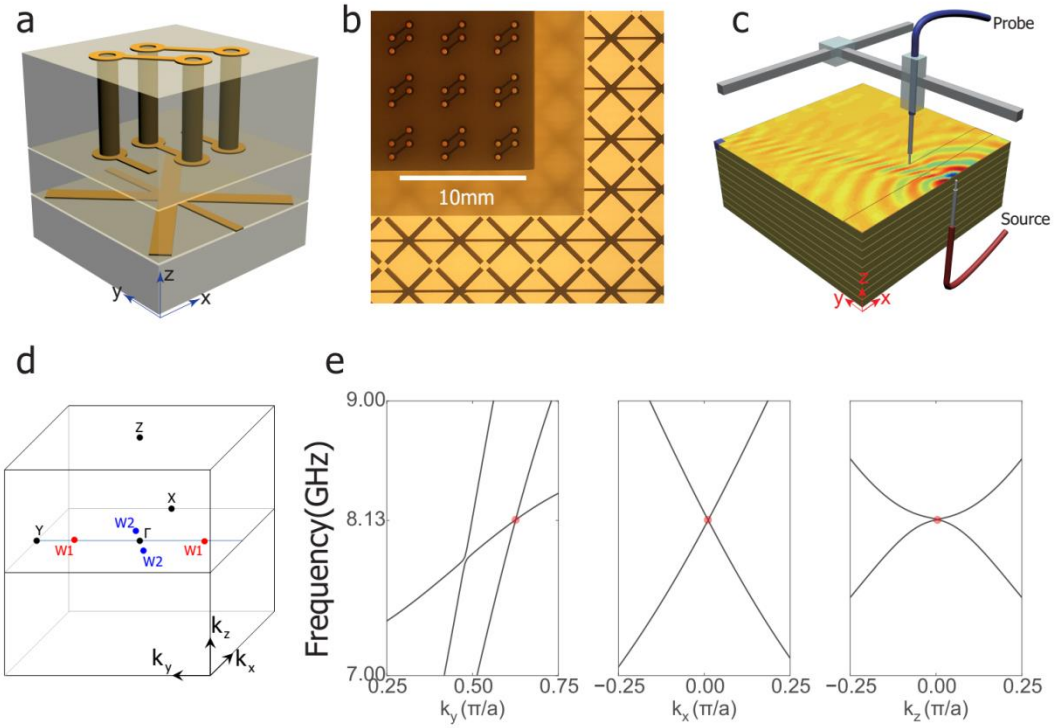


***Figure 2.2 Photonic type-II Weyl semimetal realized within a chiral hyperbolic metamaterials (CHM).[36]***

(a) Cubic unit cell of CHM with side length *a=4 mm*, consisting of three

layers, bottom hyperbolic layer (1mm), middle blank layer (1mm) and top chiral layer (2mm). Each helix has 2.5 turns, with its axis along the *x*-direction. Its length and cross-sectional area are optimized to give a fundamental resonance frequency around 5 GHz. The blank layer (FR4) between the chiral and hyperbolic layer is designed to avoid shorting contact between them. (b) Tri-layer sample fabricated with printed circuit board technology. There are 75 unit cells ($4 \times 4$ mm$^2$) along the in-plane directions on each layer. On the hyperbolic layer, metallic lines go through the whole layer along *y* direction. (c) Experimental setup and layer-stacking geometry. The field pattern represents the real experimental data scanned under *X* (polarized source) – *Z* (polarized probe) configuration at 5.82 GHz. Surface wave is excited by one antenna source, another antenna serves as probe scanning the propagating near field. (d) Bulk Brillouin zone and locations of Weyl points for W1: (±0.01,±0.62) $\pi/a$ and W2: (±0.30,±0.14) $\pi/a$. (e) shows simulated linear degeneracies around one type-II Weyl point (W1, frequency at 8.13 GHz) with realistic structure designed in CST microwave studio.

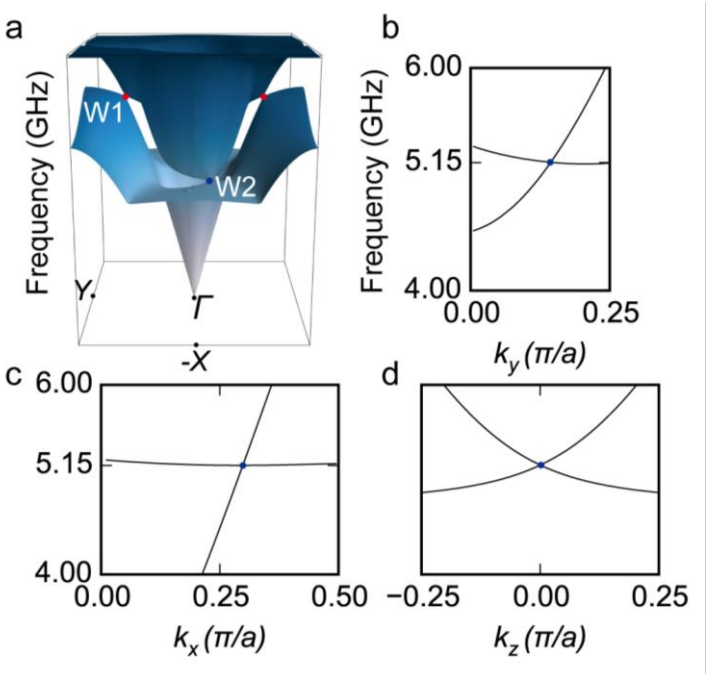


***Figure 2.3 Dispersion relations simulated from realistic structures by CST Microwave Studio.[36]***

(a) Energy dispersion on $k_x$ - $k_y$ plane with $k_z$ = 0, the Weyl points are marked with red and blue spheres (one W2 is blocked). (b), (c) and (d) show linear dispersions along three orthogonal directions in the vicinity of

W2. From (a), we can see four Weyl points similar to the prediction by the effective medium model in ***Figure 2.1***c. Due to bi-anisotropic effect, those Weyl points in the real structures slightly shift away from the high symmetry axis. However, they cannot annihilate each other because the chiral partners (W1 and W2) are located at different frequencies. Thus from this perspective, they are very robust against weak perturbations. In (c), one band along $k_x$ direction is almost flat and the group velocity approaches to zero. This is due to the strong resonance induced by chiral helixes. The simulation is performed with eigen-mode solver in CST micro studio.

The CST simulated dispersion on $k_x$ - $k_y$ plane with respect of $k_z = 0$ is shown in ***Figure 2.3***a. Furthermore, linear band crossing around W2 is presented in the ***Figure 2.3***b, c and d, from which we can see W2 behaves like a transition between type-I and type-II Weyl points.

## 2.3 Near field scanning measurement setup

Experimental setup is shown in ***Figure 2.2***c. A pair of antennas is placed as source and probe, respectively. Polarizations of both source and probe are determined by orientation of the antennas, which can be adjusted independently. The near field scanning data on the chiral hyperbolic metamaterials is collected using vector network analyzer (VNA) equipped with a *xyz* stage. The large flat top surface is ideal for near field scanning. In terms of side scanning, because there is a little cutting tolerance for each board, we do our best to make sure the sample is flat enough at least from one side view. The distance between probe and sample surface is kept around 1mm. The flatness tolerance of sample surface, especially for side surface, is controlled below 0.5mm.

Under surface near field scanning, bulk state intensity is greatly suppressed thus the surface states can be easily seen, provided that the surface states can be effectively excited by source with appropriate polarizations. The excitation proportion between surface state and bulk state also depends on the vertical distance between source and scanned surface. The shape of these surface state arcs depends on the boundary conditions of the Weyl metamaterials. In this experiment we focus on measuring the 'Fermi arcs' between air and chiral hyperbolic metamaterials, which is easy and feasible compared with other materials such as perfect electric conductor (PEC). Because of the highly anisotropic nature of type-II Weyl metamaterials and other non-rotational symmetric effects involved in the sample design, the scanned near field intensity varies sensitively with the measurement condition like source/probe polarization and sample orientation. Orthogonal polarization combination (such as $X$ polarized source and $Z$ polarized probe) shows great advantages in surface state measuring. Technically, it is easier to probe normal component of electric field compared with tangential components. Our near field scanning measurements on top/side surface geometries with different polarizations can provide complementary information to fully reveal the band structure of chiral hyperbolic metamaterials.

The measurement is performed in the microwave regime using a vector network analyzer (VNA) to sweep the frequency (5 – 10 GHz), with a near-field antenna connected to the excitation/detection port. The antenna consists of a coaxial cable with a

length (1 mm) of outer conductor and sheath stripped away, leaving the central conductor (with core diameter 1 mm) exposed, which can provide efficient coupling to large-momentum surface modes owing to the broad range of momenta present in the exponentially decaying near field both for bulk and surface states. The antenna also provides a method of measuring the amplitude and phase of the near-field of the modes with sub-wavelength resolution. The probe is most sensitive to field components parallel to its orientation.

The sample is fabricated by a commercial printed circuit board (PCB) company. Two-sample assemblies for different measurements are shown in ***Figure 2.4***. In order to clearly extract bulk and surface states from the chiral hyperbolic metamaterials, a 300 $mm^3$ block is built, which is assembled by 75 periods of tri-layers along the *z* direction. Each tri-layer consists of three sub-layers: chiral (2 mm-thick), blank (1 mm-thick) and hyperbolic layer (1 mm-thick). We scanned both top surface and side surface with probe and source antennas as shown in ***Figure 2.4***a. Both antennas can be bent to orient them in arbitrary directions to meet our different polarization requirements. ***Figure 2.4***b shows the step configuration for verifying back scattering-immune propagation. In total, four blocks are used to construct the step. The interface in the middle may introduce slight scattering for the surface wave. In the measurement, we scanned normal components of three different surfaces (top, side and lower) with probe step of 4 mm.

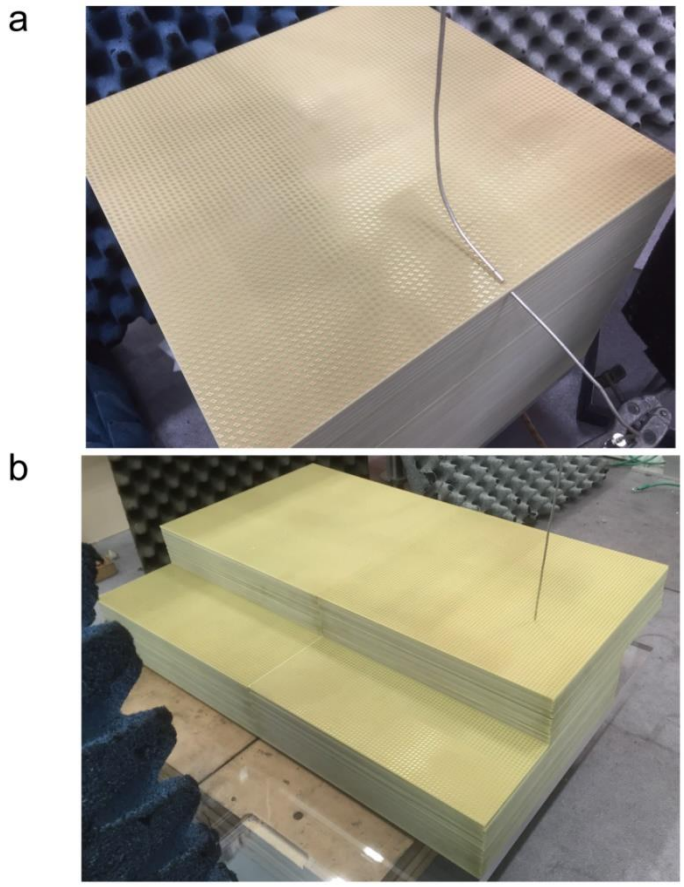


***Figure 2.4 Different sample configurations and experiment setups.[36]***
(a) A bulky material is built with 75 periods along the *z*-direction, which was used to measure the top and side topological surface-state arcs by scanning the field distribution on both surfaces. In the figure there are two probes, one of them acts as the source and the other one is the probe. (b) A step configuration is built to test the non-triviality of surface waves propagation. Four blocks are used to construct the step. The step width, height and length are 104 mm (both for upper and lower surfaces), 60 mm and 600 mm, respectively.

## 2.4 Direct observation of photonic topological surface-state arcs

The near field scans are first conducted on both top (*xy*) and side (*yz*) surfaces of chiral hyperbolic metamaterials with the same polarized source and probe, i.e. *Z* (polarized

source) - *Z* (polarized probe) for top, and *X* (polarized source) - *X* (polarized probe) for side. After the Fourier transformation of the near field spatial distribution, we obtain ***Figure 2.5***a and b presenting the 'Fermi surfaces' (both bulk and surface states, i.e. the equi-frequency contours) at 5.46 GHz for the top and side surfaces, respectively. As can be seen, 'Fermi arcs' are tangent and terminated to their corresponding bulk modes in both top and side cases. Due to the unavoidable slight misalignment of the sample's layer-by-layer assembly, the 'Fermi arc' on the side surface is not as clear as the one on the top. ***Figure 2.5***c and d show the top- and side-scanned Fermi surface at 8.13 GHz respectively, at which frequency Weyl point W1 appears and 'Fermi arcs' are too weak to be observed. From ***Figure 2.5***c, one can see a resemblance to the modelled density of states (DOS) in ***Figure 2.1***a, a feature that provides verification of type-II Weyl dispersion. As previously discussed, the misalignment of the helix axis with the underlying lattice results in a shift of the Weyl points away from the $k_y$ axis. However, this shift is too small to be observed in our experiment due to limited k-space resolution, which is determined by the maximum size of sample scanned. In ***Figure 2.5***d, a similar DOS 'crossing' can be seen from the side surface scan, as schematically showed in ***Figure 2.1***b. Due to the limitations of the equipment, W2 Weyl points locate at a relatively low frequency (5.15GHz), which cannot be clearly recognized in this work. These measured bulk/surface band structures are consistent with the simulations (CST Microwave Studio) in terms of the 'Fermi surfaces' and their locations in the

momentum space, as shown in ***Figure 2.5.*** The deviations between the measurements and calculations regarding the exact shape and size of each 'Fermi surface' may arise from the sample fabrication errors and misalignment of layer stacking. Additional comparisons between experiment and simulation results at different frequencies are given in ***Figure 2.6***.

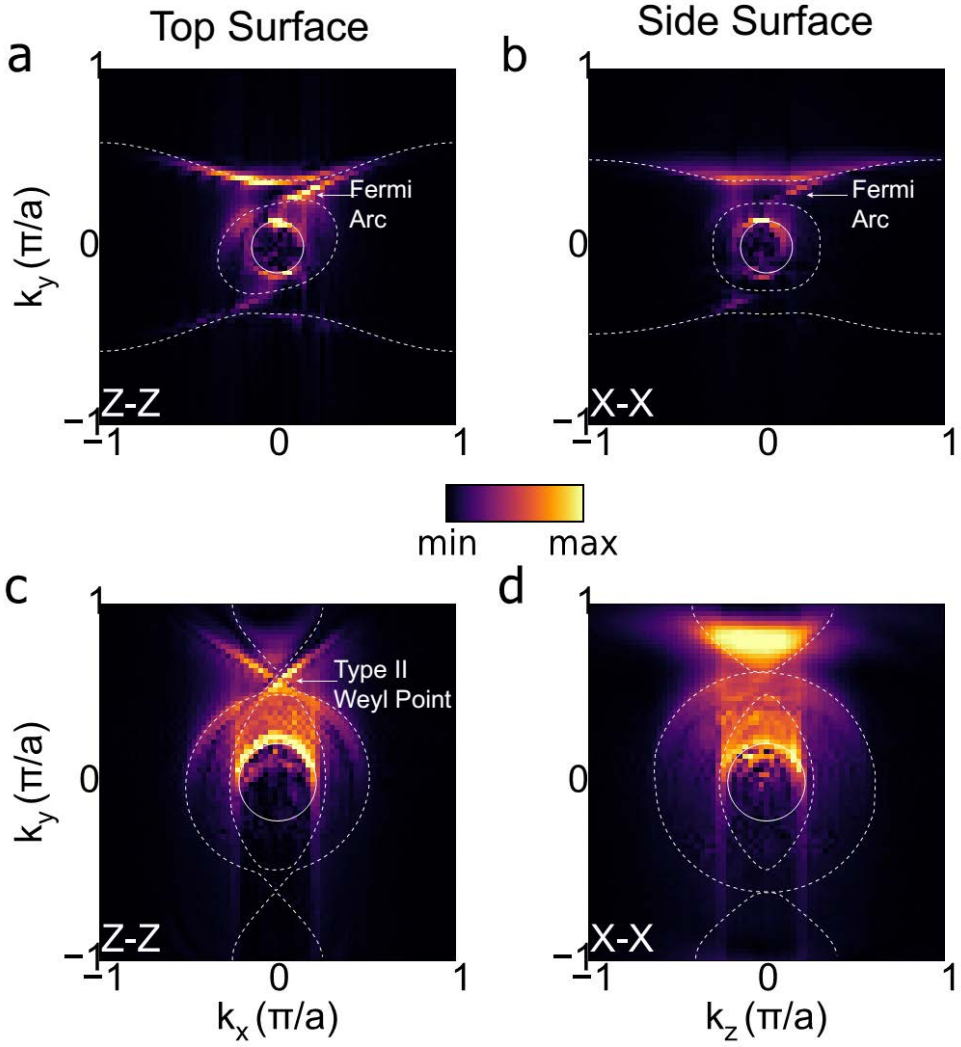


***Figure 2.5 Photonic 'Fermi surfaces' at two different frequencies. [36]***
Scanned with the configuration of *Z* (polarized source) - *Z* (polarized probe, E field) on the top surface at (a) 5.46 GHz and (c) 8.13 GHz. Scanned with the configuration of *X* (polarized source) - *X* (polarized

probe, E field) on the side surface at (b) 5.46 GHz and (d) 8.13 GHz. Solid circles indicate air-light cone. Data in $k_y < 0$ range are back-scattered from $y$-maximum boundary. Dashed curves present simulation results from microwave CST studio. 'Fermi arcs' and type II Weyl points are indicated by the white arrows. The crosses in (c) and (d) show another characteristic feature of type II Weyl semimetal as showed in Fig. 1(a) and (b) DOS planes.

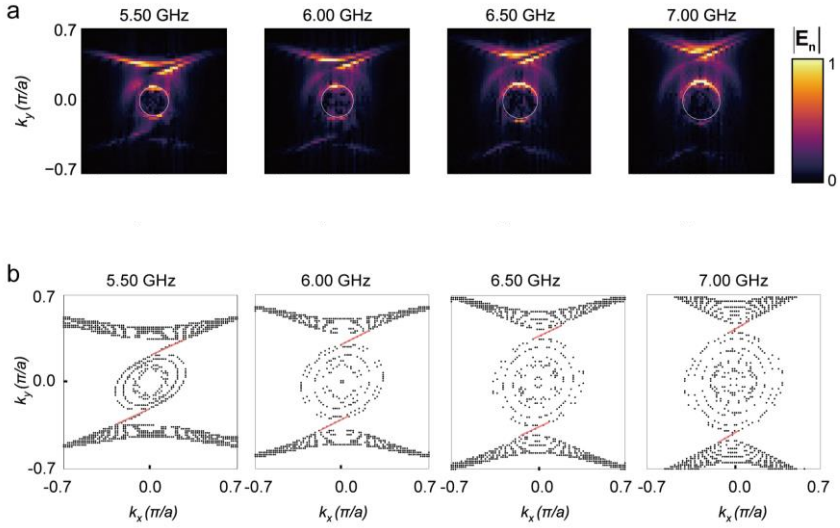


***Figure 2.6. Experimental and simulated equi-frequency contours with respect to different frequencies scanned on the top surface.[36]***

(a) shows the experimental results with the polarization configuration that is a $Z$ - polarized source detected by a $Z$ - polarized probe. In all panels, the normal components of the electric fields are normalized to the same reference value. White circles represent the light cone. Topological surface-state arcs serve to bridge the nontrivial gap. From 5.50 GHz to 7.00 GHz, the experiment results show strong resemblance with simulation results shown in (b), which are simulated in CST using supercell with length of 20 unit cells along the $z$ - direction. Red line segments highlight the topological surface-state arcs. (a) and (b) panels share the same $k_x$ - $k_y$ range.

As mentioned above, our near field scanning measurements on the top and side surface configurations with different polarization combinations can provide complementary information for revealing the topological features of chiral hyperbolic metamaterials.

***Figure 2.7***a and b show a surface wave on the top surface with *X* (polarized source) - *Z* (polarized probe) configuration. Both real space and momentum space show the strong excitation of surface state in the nontrivial gap by the antenna source. The intensity contribution from bulk bands, on the other hand, is largely suppressed and decay rapidly away from the source position (*x = 150, y = 0*). When the surface wave impinges on a surface edge invariant along *y* direction, the topologically nontrivial surface wave is expected to travel around the right-angle edge and continue propagating on the side surface (*y*-*z* plane). ***Figure 2.7***c shows the results when an *x*-polarized probe scans the side surface with the source placed at top surface ($x = 10$, $y = 0$). One can observe that the bulk modes are dramatically weakened by edge backscattering but the surface wave is not, which can also be confirmed by its bright topological 'Fermi arcs' as shown in ***Figure 2.7***d compared with ***Figure 2.5***b.

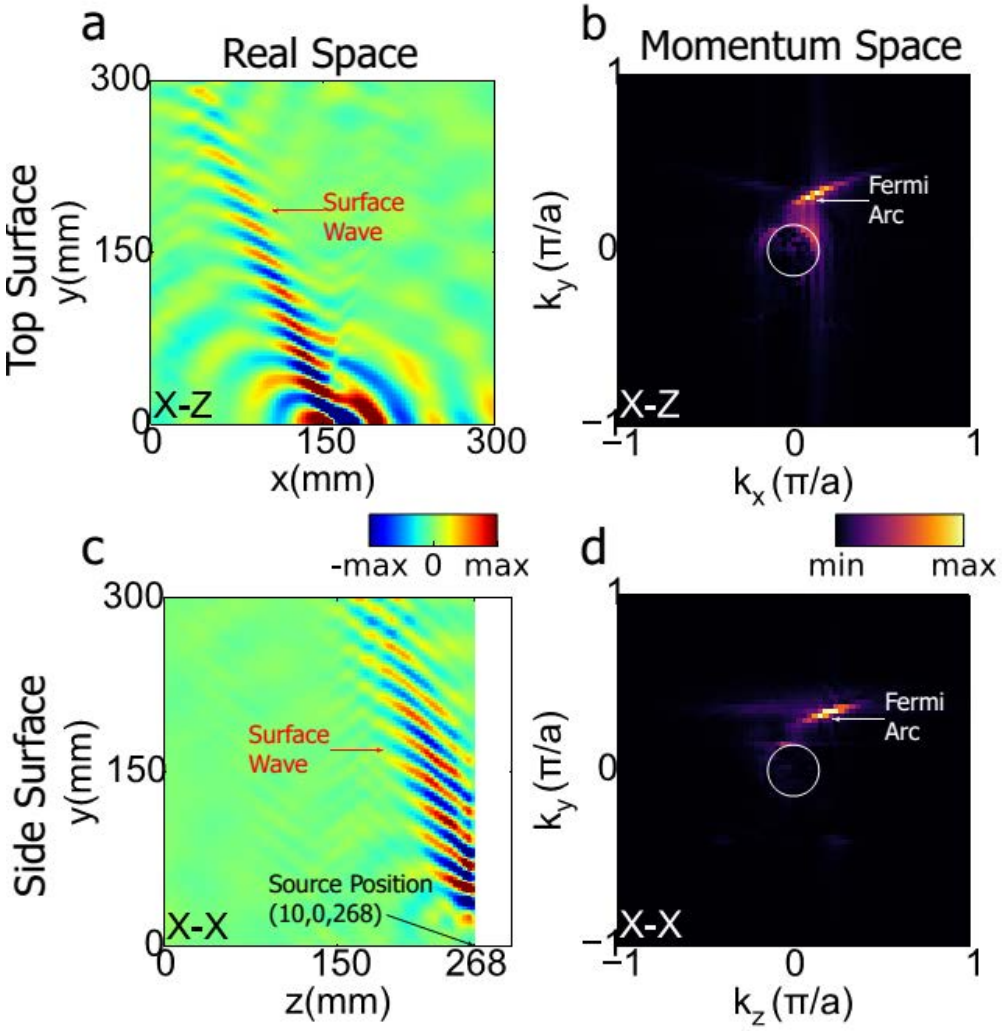


***Figure 2.7 Topologically protected surface waves and corresponding 'Fermi arcs'.***

Top surface scan taken with the *X* (polarized source) - *Z* (polarized probe, E field) configuration at 5.46 GHz. (a) Real-space instantaneous field. (b) Momentum space amplitude field, being Fourier transformed from (a). Side surface scan with respect of *X* (polarized source) - *X* (polarized probe, E field) configuration at 5.46 GHz. (c) and (d) present the same plot as (a) and (b) but on the side surface. The excitation source position for the side surface scan is positioned on top surface with coordinate indicated in unit of 'mm'. Solid circles indicate air-light cone, which are far away from 'Fermi arcs', thus surface wave is being well localized.

## 2.5 Weyl point in energy-momentum space

Surface near-field scanning collects both bulk and surface state information. From the near-field pattern, we extract energy-momentum dispersion with different momentum cuts as shown in ***Figure 2.8***. The experimental results are presented in top rows and the simulation results are in the bottom for both top/side surface scans. In ***Figure 2.8***a, from right side to left side, there is a transition occurring at $k_x = 0$. Starting from $k_x = 0.2$, we can see a big gap labelled as gap-I in both experiment and simulation results. Below gap-I, a nontrivial surface state exists. When moving the momentum cuts from $k_x = 0.2$ to $k_x = 0.1$, a new gap labelled as gap-II appears. The nontrivial surface state here develops into a border between gap-I and gap-II. When $k_x = 0$, gap-I disappears and only gap-II survives, where one can see a type-II Weyl degeneracy. Further shifting the momentum cuts to negative $k_x$, gap-II remains and becomes larger. Shown in ***Figure 2.8***b, similar discussions can be made on side surface scan result. However, the presence of slight bi-anisotropic effect induces a tiny gap at $k_z = 0$, where nontrivial surface state serves to 'bridge' the nontrivial gap.

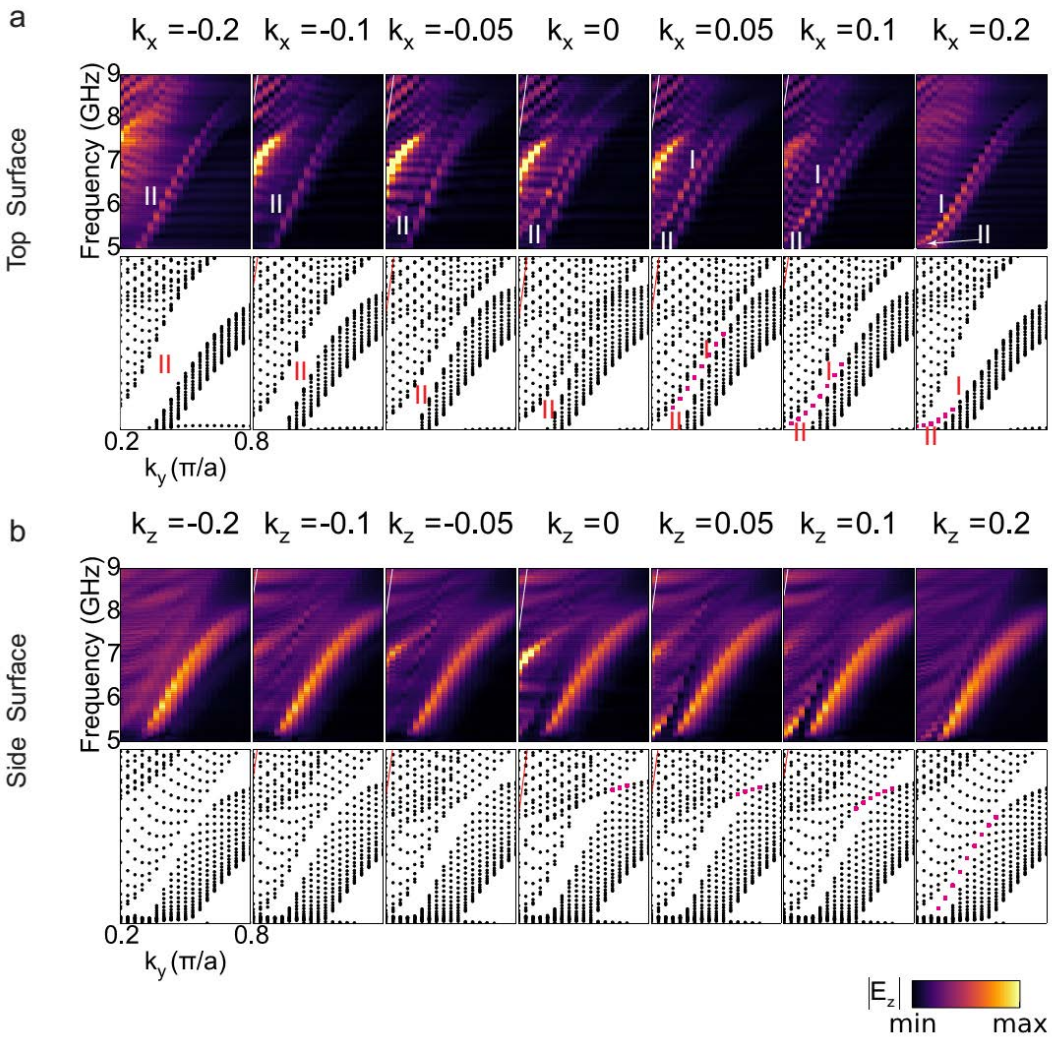


***Figure 2.8 Experiment and simulation results with respect of multi-momentum cuts.***

(a) Comparison between experiment and simulation results on top surface. (b) is similar to (a) but on side surface. Both white/red lines represent light cone. Red square dots indicate nontrivial surface states. The *k* components are in unit of $\pi/a$.

## 2.6 Topologically protected surface wave steps down

In order to demonstrate the topological protection of the surface state, a step configuration is created by stacking a metamaterial block on top of another with a 104

mm shift in the *x* direction, as shown in ***Figure 2.9***. A surface wave is launched at the upper surface, and the probe scans the normal field distribution in the upper, side and lower surfaces at frequency of 5.46 GHz. It is observed that the surface wave conformally bends around the step and keeps propagating forward without being reflected by the edges. It should be noted that since our probe antenna cannot reach the lower corner (built by side and lower surfaces) due to thick cladding layer of the antenna cable, there exists a discontinuity in the measured phase across the lower corner. This measurement of robust propagation of surface wave across the step serves as a direct observation of the topological protection of 'Fermi arcs'. From the 'step' experimental geometry, a surface wave 'periscope' could be proposed to promote imaging/sensing technology. The robust propagation of Fermi arc surface states may facilitate the design of integrated photonic circuits with three-dimensional topography.

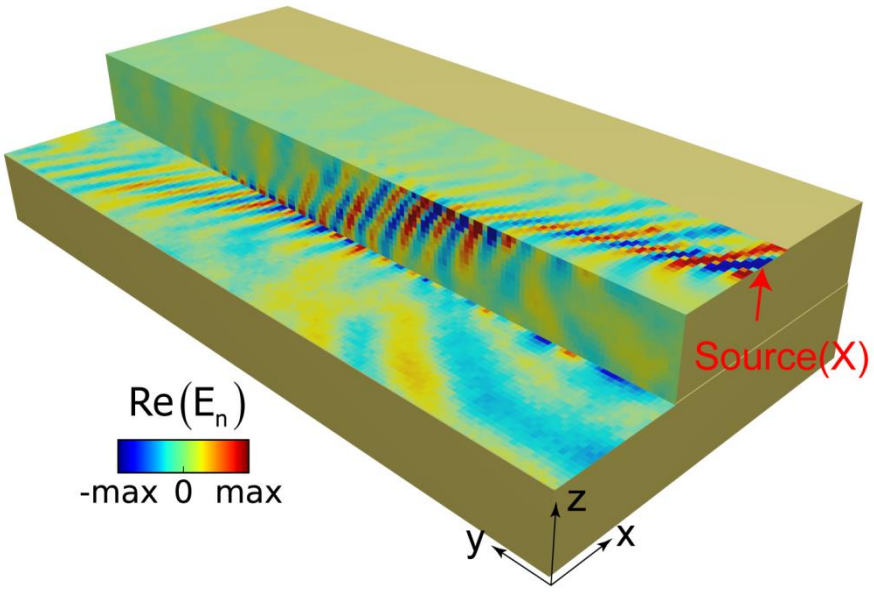


***Figure 2.9 Topologically protected surface wave steps down.[36]***
A backscattering-immune surface wave propagates on the three-dimension step geometry. The source (red arrow) is set with *x*-polarization, while the normal component of the electric field is probed for all surfaces. The step width, height and length are 104 mm (both for upper and lower surfaces), 60 mm and 600 mm, respectively. The normal electric field is normalized with respect to its maximum value.

## 2.7 Effective medium analysis

The realistic structure consists of a chiral layer (metallic springs oriented along *x* direction) and a hyperbolic layer (continuous metallic wires along the *y* direction). By considering the motion of electrons driven by external electromagnetic field on those metallic components [60,61], a Hermitian Hamiltonian can be obtained to describe the dispersive system,

$$H\psi = N^{-1/2}MN^{-1/2}\psi = E\psi \qquad [2\text{-}1]$$

where M and N are the matrices describing the dispersive properties of the effective model,

$$M = \begin{bmatrix} 0 & 0 & 0 & 0 & k_z & -k_y & 0 & -i\frac{\alpha}{\beta} & 0 \\ 0 & 0 & 0 & -k_z & 0 & k_x & 0 & 0 & -i\omega_p \\ 0 & 0 & 0 & k_y & -k_x & 0 & 0 & 0 & 0 \\ 0 & -k_z & k_y & 0 & 0 & 0 & 0 & 0 & 0 \\ k_z & 0 & -k_x & 0 & 0 & 0 & 0 & 0 & 0 \\ -k_y & k_x & 0 & 0 & 0 & 0 & 0 & 0 & 0 \\ 0 & 0 & 0 & 0 & 0 & 0 & 0 & i\omega_0^2\frac{1}{l\beta} & 0 \\ i\frac{\alpha}{\beta} & 0 & 0 & 0 & 0 & 0 & -i\omega_0^2\frac{1}{l\beta} & 0 & 0 \\ 0 & i\omega_p & 0 & 0 & 0 & 0 & 0 & 0 & 0 \end{bmatrix} \quad [2\text{-}2]$$

$$N = \begin{bmatrix} \varepsilon_x & 0 & 0 & 0 & 0 & 0 & 0 & 0 & 0 \\ 0 & 1 & 0 & 0 & 0 & 0 & 0 & 0 & 0 \\ 0 & 0 & \varepsilon_z & 0 & 0 & 0 & 0 & 0 & 0 \\ 0 & 0 & 0 & 1 & 0 & 0 & 0 & 1 & 0 \\ 0 & 0 & 0 & 0 & 1 & 0 & 0 & 0 & 0 \\ 0 & 0 & 0 & 0 & 0 & 1 & 0 & 0 & 0 \\ 0 & 0 & 0 & 0 & 0 & 0 & \omega_0^2\frac{A}{l^2\beta} & 0 & 0 \\ 0 & 0 & 0 & 1 & 0 & 0 & 0 & \frac{1}{\beta A} & 0 \\ 0 & 0 & 0 & 0 & 0 & 0 & 0 & 0 & 1 \end{bmatrix} \quad [2\text{-}3]$$

$$\psi = \begin{bmatrix} E_x \\ E_y \\ E_z \\ H_x \\ H_y \\ H_z \\ P_x \\ M_x \\ V_y / \omega_p \end{bmatrix} \qquad [2\text{-}4]$$

where $k$ is the wavevector, $\alpha = l / L, \beta = A / L$, $V_y = dP_y / dt$, $P$ and $M$ are electric and magnetic dipole moments, respectively.

In the model, we neglect the ohmic loss and the interactions between intra and inter layers. The slight bi-anisotropic effect mentioned above has also been neglected in the effective model for sake of simplicity, as bi-anisotropy merely shifts the Weyl points around in the momentum space and cannot gap them. $\omega_p$ indicates the effective plasma frequency for hyperbolic layers. $l$ and $A$ indicate effective length and area of the metallic helix, respectively. $L$ is the effective inductance. The resonance of chiral layers is controlled by $\omega_0$. Difference in $\varepsilon_x$ and $\varepsilon_z$ is due to the anisotropy induced by cross structures in hyperbolic layers. Spatial non-local effect is considered through introducing an even order (keeping time-reversal symmetry) $k_y$ fraction in the effective plasma frequency,

$$\omega_p = 1 + \frac{ak_y^2}{1 + bk_y^2} \qquad [2\text{-}5]$$

Energy dispersion and surface states on the top surface are calculated as shown in ***Figure 2.1***c with $\omega_0 = 1/3, A = 1, l = 1, L = 3, \alpha = l/L, \beta = A/L, a = b = 0.2$, and $\varepsilon_x = \varepsilon_z = 2$ (for simplicity, we keep $\varepsilon_x = \varepsilon_z$, the anisotropy is already induced by the helix along the *x* direction). In the effective media calculation, we set $\varepsilon_0 = \mu_0 = c = 1$, where *c* is the light velocity in vacuum.

Exactly accompanying with this effective Hamiltonian, the corresponding dispersive constitutive relation reads,

$$\begin{cases} \vec{D} = \ddot{\varepsilon}\vec{E} + i\ddot{\gamma}\vec{H} \\ \vec{B} = \ddot{\mu}\vec{H} - i\ddot{\gamma}\vec{E} \end{cases} \qquad [2\text{-}6]$$

where $\ddot{\varepsilon}, \ddot{\mu}, \ddot{\gamma}$ only have diagonal elements,

$$\ddot{\varepsilon} = \begin{bmatrix} \varepsilon_x + \dfrac{\alpha l}{\omega_0^2 - \omega^2} & 0 & 0 \\ 0 & 1 - \dfrac{\omega_p^2}{\omega^2} & 0 \\ 0 & 0 & \varepsilon_z \end{bmatrix} \qquad [2\text{-}7]$$

$$\ddot{\mu} = \begin{bmatrix} 1 + \dfrac{\beta A \omega^2}{\omega_0^2 - \omega^2} & 0 & 0 \\ 0 & 1 & 0 \\ 0 & 0 & 1 \end{bmatrix} \qquad [2\text{-}8]$$

$$\vec{\vec{\gamma}} = \begin{bmatrix} \frac{l\beta\omega}{\omega_0^2 - \omega^2} & 0 & 0 \\ 0 & 0 & 0 \\ 0 & 0 & 0 \end{bmatrix} \qquad [2\text{-}9]$$

## 2.8 Discussion

For the surface wave supported on the interface between air and chiral hyperbolic metamaterials, there is only a single surface mode existing in the gap as indicated by the gray line in ***Figure 2.10***a. Thus, when this surface mode is excited on the interface, it will propagate towards left direction and cannot be back-scattered by sharp corners, such as the rectangle step as showed in ***Figure 2.10***c. On the contrary, normal surface waves have two modes which are not orthogonal to each other as showed in ***Figure 2.10***b, and left-propagation wave can in general be scattered backwards (***Figure 2.10***d).

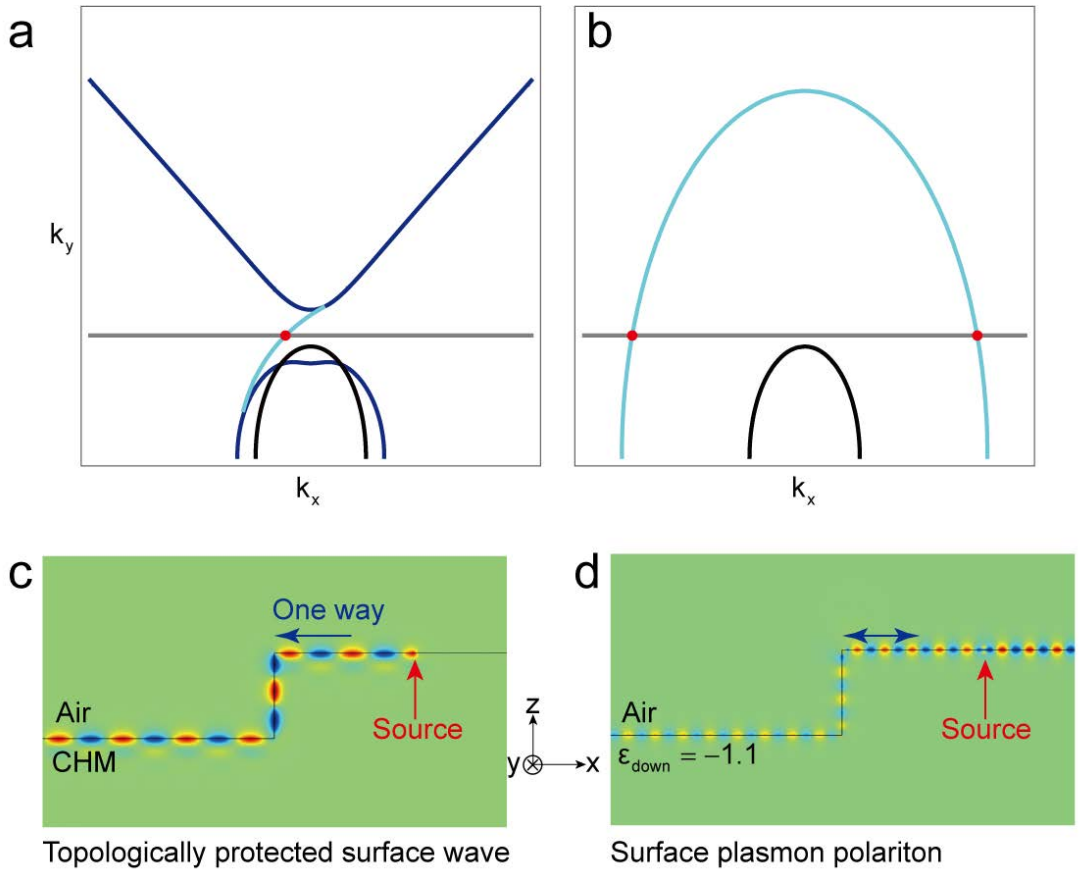


***Figure 2.10 Comparison between surface wave supported by chiral hyperbolic metamaterials and surface plasmon polariton. Cyan and black lines indicate surface states and air light cones, respectively. Panels a and b show the equi-frequency contour (EFC).***

The existence of Fermi arc surface states is guaranteed by the bulk-surface correspondence condition. Although the Fermi arcs must connect the projected opposite Weyl points, or the equifrequency frequency contours (EFC) that enclose the Weyl points, the allowed momenta (the exact location of Fermi arc in the momentum space) are determined by the boundary condition of electromagnetic wave, and therefore they are different for different surrounding media. This is illustrated by the plot of the Fermi arcs at the interface of a hyperbolic chiral medium with air and perfect electric

conductor (PEC) as the surrounding media, respectively. Note that for simplicity, the calculation is performed on an effective medium with constitutive relations defined as,

$$\varepsilon = \begin{bmatrix} 3 & 0 & 0 \\ 0 & 3 & 0 \\ 0 & 0 & -3 \end{bmatrix}, \mu = \begin{bmatrix} 1 & 0 & 0 \\ 0 & 1 & 0 \\ 0 & 0 & 1 \end{bmatrix}, \gamma = \begin{bmatrix} 1 & 0 & 0 \\ 0 & 0 & 0 \\ 0 & 0 & 0 \end{bmatrix} \quad [2\text{-}10]$$

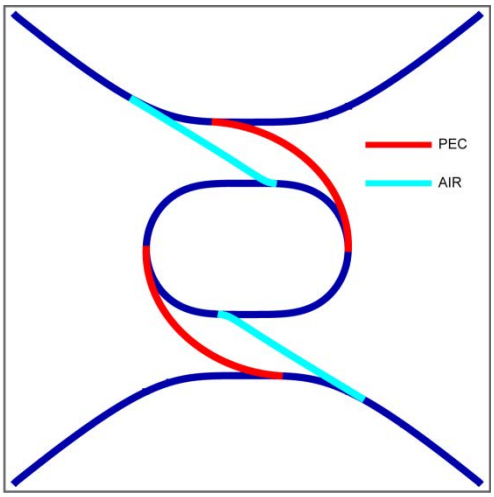


***Figure 2.11 Position of topological surface-state arcs depending on the surrounding media.***

If one wants to experimentally distinguish bulk and surface states, it is better to probe field inside the sample (chiral hyperbolic metamaterials). Obviously, it is impossible. However, we still can claim bulk/surface states by comparing experimental results with simulation results. In the CST microwave studio simulation, surface state is well localized around the boundary, while bulk state extends in the chiral hyperbolic metamaterials. ***Figure 2.12*** shows the simulation result.

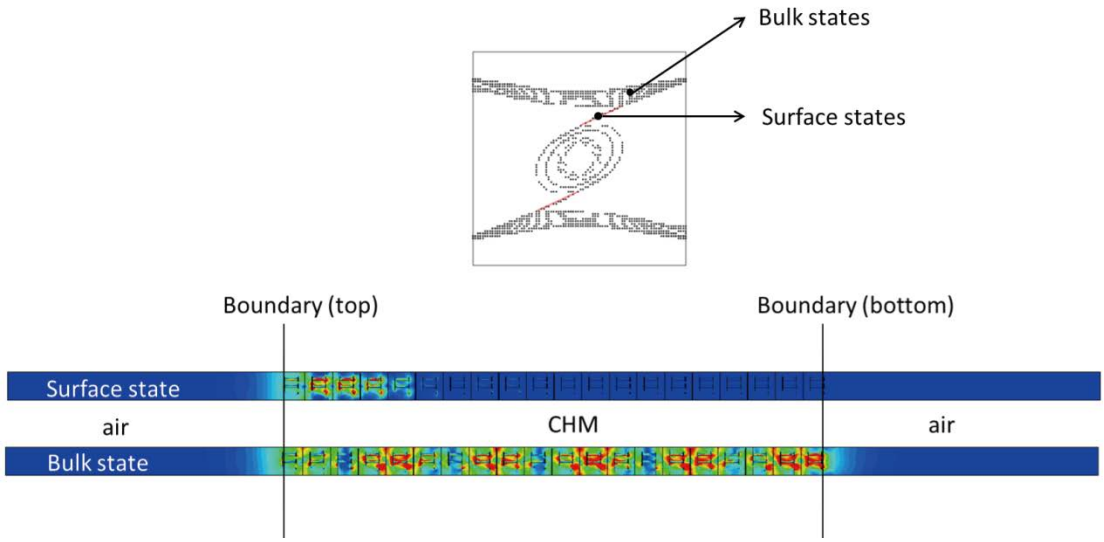


***Figure 2.12 Field distribution of bulk and surface states simulated with realistic structures in CST with eigen mode solver. The supercell consists of 20 unit cells.***

## 2.9 Conclusion

We have made a direct observation of photonic topological surface-state arcs at the surfaces of a photonic type-II Weyl metamaterial. Our work may well provide new insights and open new avenues to surface photonics. Owing to the robustness of topologically protected surface wave propagation and other practical advantages in photonic systems, such as artificially controllable structure design, we anticipate our observation to be a starting point for surface periscope imaging technology, near field sensing and directional information transmission in bulky integrated photonics.

# Chapter 3. Observation of ideal photonic Weyl system

Light cone, indicating the relativistic linear crossing of energy bands, located at the origin of (3+1) dimensional momentum-energy space, manifests fundamental behaviors of light. Weyl cone, exhibiting similar exotic properties, arbitrarily migrated away from the origin, has attracted extremely broad interests. Among them, discovery of a truly ideal Weyl system, whose Weyl nodes are symmetry related and not submerged by other complicated bulk bands, shows great significance both from practical application and fundamental research. In this chapter, we experimentally explore an ideal photonic Weyl system simply protected by a non-centrosymmetric point symmetry. Intriguingly, helicoidal structure of topological surface-state arcs and chessboard like Weyl nodes interference are mapped out through near field scanning measurement. The observation provides a prototype platform in discovering light-cone related properties and paves a systematic way towards realizations of photonic topological phases. This chapter includes passages from the publication [47].

## 3.1 Introduction

In Weyl system, energy bands are linearly cross at isolated points in the momentum space, which is an incarnation of the well-known light cone ($E = c\,p$) in terms of energy dispersion. Any unreachable phenomena related to the conical dispersion of light cone could be observed around Weyl energy in principle. In other words, Weyl systems also offer way to break down the bulwark of zero-frequency and open gates to explore exceptional electromagnetic performances, such as negative refraction, momentum filter [62], divergence maximum cross section [63] and so on.

Frankly, the discovery of Weyl nodes is not a tough work with either breaking time-reversal or inversion symmetry. However, realization of a truly ideal Weyl system [5,64,65], where all Weyl nodes are symmetry related, residing on the same energy with a large momentum separation and no non-topological bands near in a sufficiently large energy interval, is very challenging. Meanwhile, an ideal Weyl system is of the essence in both characterizing the underlying topological features and exploiting novel applications. For example, it has been predicted that the surface state around a Weyl node carries helicoidal structure [66] - a useful analogy is to the Riemann surface generated by a multi-valued function (***Figure 3.1***a). Without a clear system, its verification is impossible. Also, light cone related researches beyond traditional perspectives requests for a clear platform where equi-frequency contour (EFC)

possesses vanishing volume [63].

The way to find an ideal Weyl system is starting with symmetry analysis. The gapless excitation of Weyl nodes is protected by global topology rather than local symmetry, there is no residual momentum-conserving terms in a 2 × 2 Hamiltonian that can gap the linear crossing. But, imposed symmetry constraints serve to trim and tidy a Weyl system. Here, by analyzing electromagnetic coupling mechanism of metallic structures in crystalline lattice, termed as meta-crystal, we explore an ideal photonic Weyl system simply protected by $D_{2d}$ point symmetry. In total, there are only four Weyl points, which are the minimum number allowed under time-reversal symmetry. Through near field scanning measurement, we map out helicoidal structure of surface states. It is fundamental in unveiling the chirality of Weyl nodes, which is usually determined with deep insight of bulk states. Moreover, interference between isolated Weyl nodes (valleys) is observed through near field scanning measurement of the transmission field with respect of a point source excitation. This is another characteristic phenomenon attributed to the linear band crossing around Weyl node. Since wave having quadratic band dispersion with group velocity approaching to zero is always accidentally localized by disorders, even where EFC happens to consisting of isolated ellipsoids. In general, exploration of ideal Weyl system in photonics bears lots of accessible advantages, such as, exquisite adjustability of frequency, artificially designable structure and room temperature operation. These also imply that the robust topological phase can

be brought to application more realistically through topological photonics. Our discovery will offer a prototype platform, where those proposed intriguing applications that merit further studies in ideal Weyl systems can be feasibly verified.

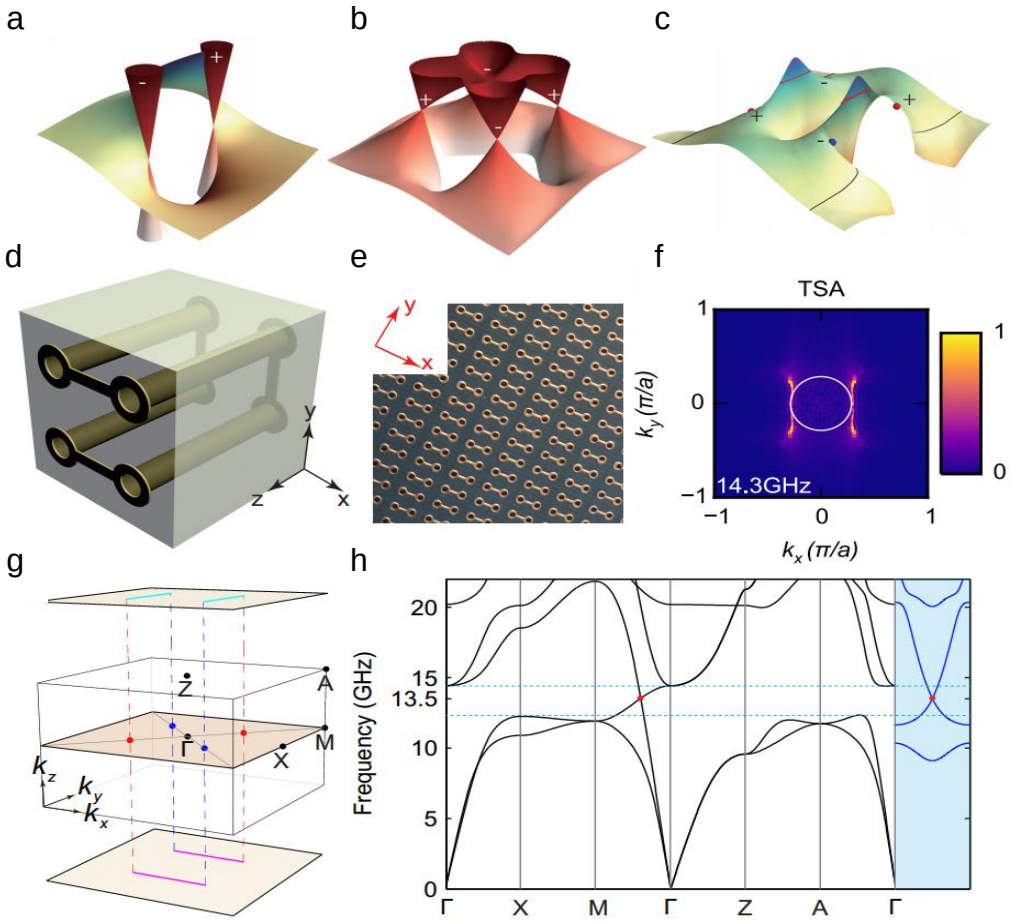


***Figure 3.1. Structure and band topology of the ideal photonic Weyl meta-crystal.***

(a) Map of helicoidal structure of topological surface state arcs between a pair of Weyl nodes, ideally illustrated by Riemann surface. (b) Four symmetry related ideal Weyl nodes in the ideal photonic Weyl meta-crystal, and their band dispersion in $k_x$-$k_y$ plane when $k_z = 0$. (c) Helicoid surface states on the interface between air and ideal photonic meta-crystal, simulated under a supercell configuration in CST microwave studio. ± indicates the corresponding topological charge ±1, respectively.

Black and red lines indicate topological surface-state arcs at 13.0 GHz and 14.3 GHz, respectively. (d) Unit cell consisting of saddle shaped metallic connective structure, which has non-centrosymmetric $D_{2d}$ point group symmetry. (e) Sample fabricated with printed circuit board technology, the view indicates the top surface. The bulk sample is assembled by layer-layer stacking along $z$ direction. There is a 1.5mm-thick blank layer (not shown) between two adjacent 3mm-thick structure-layers (d) to prevent short contacting from metallic coils. Consequently, the saddle coil structure can be seen as periodically buried in a background material with dielectric constant of 2.2 where the periods along $x$, $y$ and $z$ directions are $a_x = a_y = a = 3$ mm and $a_z = 4.5$ mm, respectively. (f) Bulk and surface Brillouin zone with four Weyl points located on ΓM. Top and bottom surface Fermi arcs are schematically showed. (g) CST simulated band structure along high-symmetry lines. Dashed cyan lines highlight the clean window where Weyl point (red point) resides. The most right shadowed panel presents linear degeneracy along $k_z$ direction when $k_x = k_y = 0.4\ \pi/a$. (h) Topological surface-state arcs at 14.3GHz, measured on the top surface with near field scanning method. White circle indicates air equi-frequency contour at 14.3 GHz.

## 3.2 Design of photonic ideal Weyl system

The designed ideal photonic Weyl meta-crystal belongs to the simple tetragonal lattice with symmorphic space group P-4m2 (No. 115). In each primitive cell, there contains a saddle-shaped connective metallic coil (***Figure 3.1***d and e), which possesses $D_{2d}$ ($\bar{4}2m$ in Hermann-Mauguin notation) point group symmetry [62,64]. Obviously, the system has excluded spatial inversion ($i$). These metallic elements support localized resonances with current distributions expandable into multipolar modes, such as toroidal dipole or anapole excitation. In an effective media model (see ***section 3.6***), these resonances collectively exhibit bi-anisotropic effect, leading to directionally dependent chirality response [67]. Weyl point usually arises from accidental degeneracy from two

orthogonal states, which further span a two dimensional spin-space. Here, the unavoidable crossing between a longitudinal mode and a transverse mode leads to the formation of a type-I Weyl point, as shown in ***Figure 3.1***h [35]. From irreducible representation analysis of point group, these two modes belong to two different classes with eigenvalues ± 1 of $C_2$ rotation along ΓM, where level repulsion is forbidden (see ***section 3.7***). The other three Weyl points can be obtained after symmetry operations of $D_{2d}$. For instance, three two-fold rotation symmetries ($C_2$ and $2C_2'$) combined with time-reversal symmetry guarantee that these four Weyl nodes locate on ΓM with exactly the same frequency, the so called three dimensional analogy of graphene as shown in ***Figure 3.2***. The corresponding chirality is labelled on ***Figure 3.1***b and c, where two mirror symmetries ($\sigma_x$ and $\sigma_y$) can reverse the corresponding topological charges. ***Figure 3.1***h shows the simulated band structure along high symmetry lines (as defined in ***Figure 3.1***g) in the first Brillouin zone (FBZ), where the shadow region shows the linear dispersion along $k_z$ [$-\pi/a_z$, $\pi/a_z$] with respect of $k_x = k_y = 0.40\ \pi/a$. Weyl degeneracies occurring in a relatively large energy window (between the two cyan dashed lines) devoid of other bulk bands greatly facilitates experimental identification. ***Figure 3.1***f depicts clear top topological surface-state arcs conducted at 14.3GHz, which connect the projected Weyl node pairs on the surface Brillouin zone and obey spatial symmetry ($C_2$) that is the symmetry preserved on the surface.

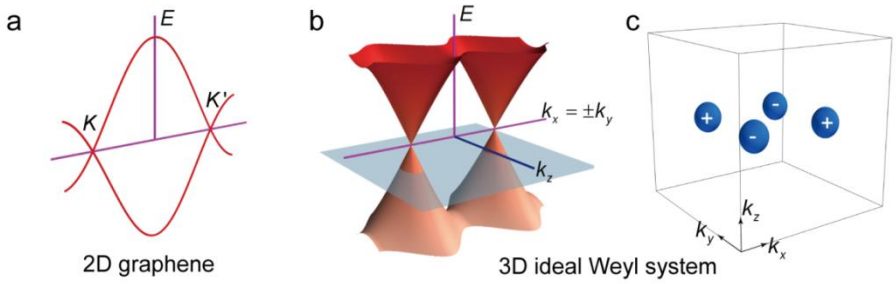


***Figure 3.2 Two-dimension graphene and three-dimension ideal Weyl systems.***

(a) Band structure of two-dimension graphene, two valleys *K* and *K'* are symmetry related. (b) Band structure of three-dimension ideal Weyl system, all Weyl nodes reside on the same energy. (c) Four-sphere like equi-frequency contour in momentum space when energy is subtly shifted away from the Weyl energy as highlighted with the plane in (b).

## 3.3 Weyl degeneracy confirmed by angle resolved transmission experiment

Firstly, we explore the ideal Weyl system by confirming linear band crossings around the Weyl energy through angle resolved transmission experiment [28]. In order to match the Weyl points with small in-plane momentum, a sample with special crystal-cutting is fabricated, as shown in ***Figure 3.3***a. ***Figure 3.3***b zooms in the shadow region in ***Figure 3.3***a, which shows the crystal orientation and unit-cell configuration close to the cutting boundaries. The length (along *a*), width (along *b*) and height (along *c*) of the sample are *300* mm, *100* mm and *300* mm, respectively. Two parameters ($\theta$ and $\varphi$) are defined as indicated in ***Figure 3.3***a (and inset) to enable the angle-resolved transmission measurement. With the specific crystal cutting, Weyl points in FBZ are projected along

$k_p$, which is defined in ***Figure 3.3***c. Obviously, two of them locate in the light circle (magenta circle) at the Weyl frequency (13.5 GHz). A plane wave illuminated directly from air on the sample can cover the two Weyl points in in-plane momentum space ($k_x$-$k_y$). Comparisons between simulation and experiment results are shown in ***Figure 3.4***a-c. In ***Figure 3.4***a with $\varphi=0$ degree, linear gapless energy dispersion is obtained and the density of states vanishes at Weyl frequency due to no other bands in energy. After rotating the sample with *30/60 degrees* ($\varphi$=*30/60 degree*) along *b* axis, there existing a complete gap as expected.

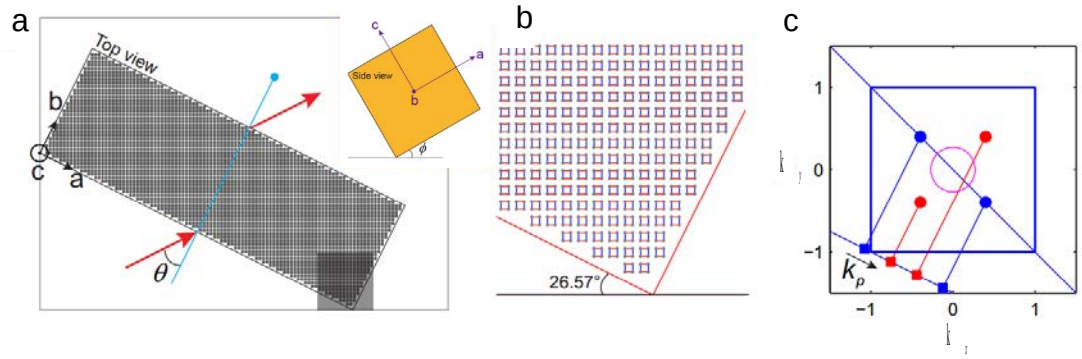


***Figure 3.3. Special sample cutting for angle resolved transmission measurement of the ideal Weyl system.***
(a) Schematic view of the sample fabricated with special crystal cutting. Top and side views are indicated. $\theta$ and $\varphi$ are rotation angles defined along the local coordinates *c* and *b*, respectively. (b) Zoomed-in view of the shadow region in (a) panel. The special crystal cutting angle is indicated. (c) Projection of Weyl points in momentum space with respect of the global coordinates (*x, y, z*). First Brillouin Zone is indicated by blue square.

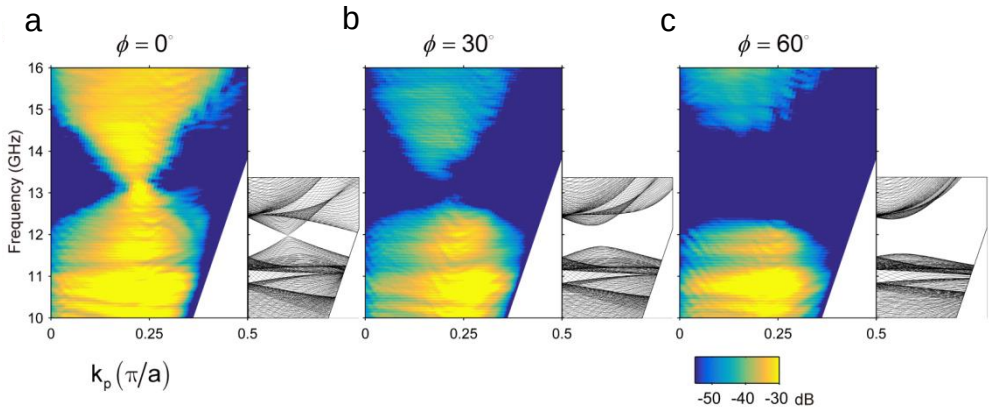


***Figure 3.4 Experiment and simulation results of angle resolved transmission measurement.***

(a) Band projections with $\varphi = 0$ degrees. Experiment and simulation results are showed in left and right panels, respectively. Magenta lines indicate light cone. (*b,c*) The same to (a) but with $\varphi = 30$ *degrees* and *60 degrees*.

## 3.4 Experimental observation of helicoid structure of topological surface-state arcs

Another direct manifestation of the topological aspects of Weyl system is the exotic topological surface states taking form of arcs as shown in ***Figure 3.1***f. Following a closed contour around an end point of the arcs one moves between the valence and conduction bands [66], which is the direct consequences of the chiral facts of Weyl nodes. After Weyl degeneracy measurement, we carry on exploring the helicoidal structure of topological surface-state arcs.

Two near-field scanning configurations with different purposes (***Figure 3.5***a and b) are used here. In setup 'a' (***Figure 3.5***a), the source is positioned at the center of the bottom surface, and the probe can raster-scan the top surface which aimed for probing both bulk

and surface mode, whereas the other one (setup 'b' as shown in ***Figure 3.5***b and c) for mainly detecting the surface states. These two setups provide complementary information for the observation of helicoid surface states. ***Figure 3.5***d shows scanned topological surface-state arcs in an extended Brillouin Zone under setup 'a', from which it is more concise and explicit to see how topological surface-state arcs across FBZ boundaries and connect to the neighbor Weyl nodes. In the measurement of both setups, we set the scanned step to be 1 mm (1/3 $a$), thus after Fourier transformation the surface momentum space range is $[-3\ \pi/a,\ 3\ \pi/a]^2$. All of equi-frequency contour (EFC) shown in later are cut from the corresponding extended Brillouin zone. Attached to the middle air equi-frequency contour (air circle), there is a quite bright topological surface-state ellipsoid. Compared with those topological surface-state arcs located near FBZ boundaries, it dominates the surface resonance with much higher intensity as shown in ***Figure 3.5***e measured under setup 'b'. There are two reasons: one is that it is easy to be excited through antenna source due to small wave vector; the other comes from its small attenuation constant in air side, thus the field is not well confined and can be coupled to the near-field probe more efficiently. For the same reason, topological surface-state arcs at 14.3 GHz can also be easily probed as shown in ***Figure 3.5***c and f from both real and momentum space perspectives, respectively. In addition, real space field distribution at 14.3GHz shows self-interference of topological surface-state arcs due to its finite length.

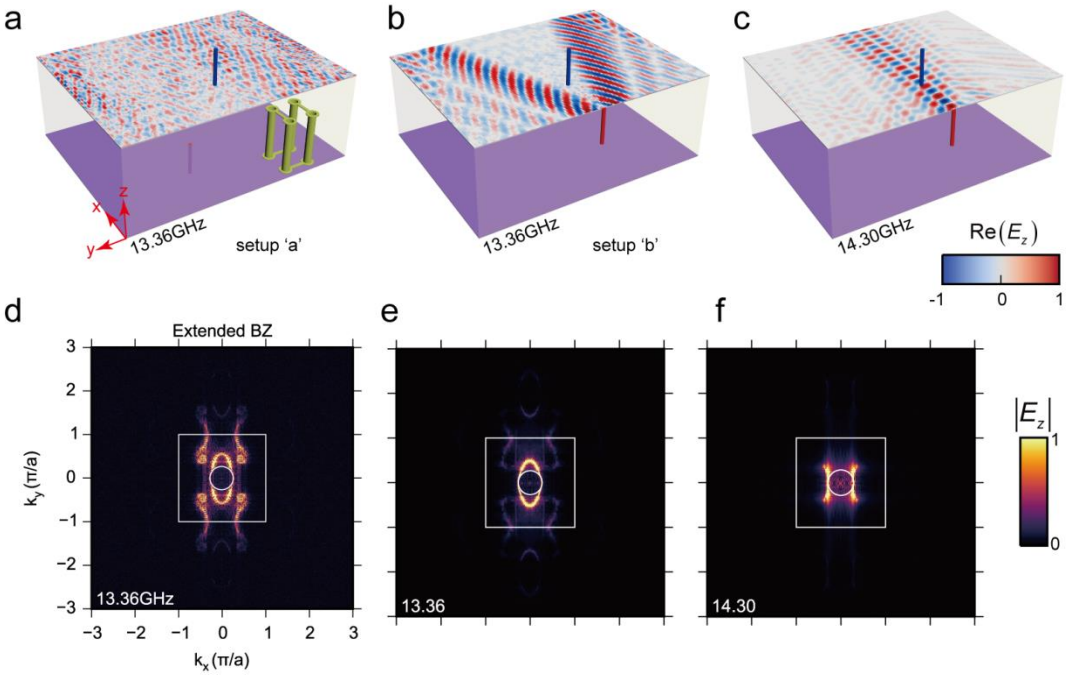


***Figure 3.5 Configuration of two near-field scanning systems.***

(a), (b) and (c) Two different experiment configurations for top surface scanning. The bottom surfaces are highlighted by purple plane. (a) indicates setup 'a' where the source is positioned on the bottom surface center, while (b/c) is the setup 'b' where the source is located on the top surface edge as shown. The structure orientation is indicated in inset. Thickness of samples in setup 'a' and 'b/c' are 10 and 20 $a_z$, respectively. The width and length for both cases are 210 mm and 270 mm. In (a/b) field distributions is taken from experiment at 13.36 GHz. (c) shows similar field distribution at 14.3 GHz. (d) Equi-frequency contour (EFC) scanned in setup 'a' at 13.36 GHz in an extended Brillouin zone. (e) and (f) EFCs scanned in setup 'b' with respect of 13.36 GHz and 14.30 GHz, respectively. The first Brillouin zone (FBZ) is indicated by the white solid square. The white circle is EFC of light cone at the corresponding frequency. In setup 'b', we set the scanned step to be 1mm. During the subsequent Fourier transformation, we mirrored and rotated one scanned field to construct a four times bigger one with source visually located at the center. This process greatly enhanced momentum space resolution, which is determined by maximum area used for Fourier transformation. For setup 'a', the scanned step is 1 mm. We also used four time bigger field to enhance resolution and eliminate the Fourier field imbalance induced by misalignment between the source and the bottom center.

Schematically, ***Figure 3.6***a shows the Riemann surface analogue to the helicoid surface states between two pair of Weyl nodes, while the helicoid structure of topological surface-state arcs measured under setup ‘a’ is thoroughly investigated by measuring a series of equi-frequency surfaces from 12.6 GHz to 14.0 GHz, as shown in ***Figure 3.6***b/d in experiment and ***Figure 3.6***c/e in simulation, respectively. With increasing frequency, the top surface Fermi arcs emerged from the Weyl node with positive (negative) topological charge rotate anti-clockwise (clockwise). The observed rotation of the helicoid surface state around a Weyl node can therefore be used to detect the chirality of the Weyl node. At lower frequencies, each topological surface-state arcs connects between the bulk states through the FBZ boundary, while the SSE expands gradually with the frequency. Around 13.56 GHz, the topological surface-state arcs and SSE join each other, which corresponds to the saddle point of the helicoid surface in ***Figure 3.6***a. Above this frequency, topological surface-state arcs and SSE reroute into a new configuration: a direct topological surface-state arcs connecting between the bulk states, and a SSE centered at the edge of the FBZ. With further increase of frequency, the SSE shrinks and disappears finally.

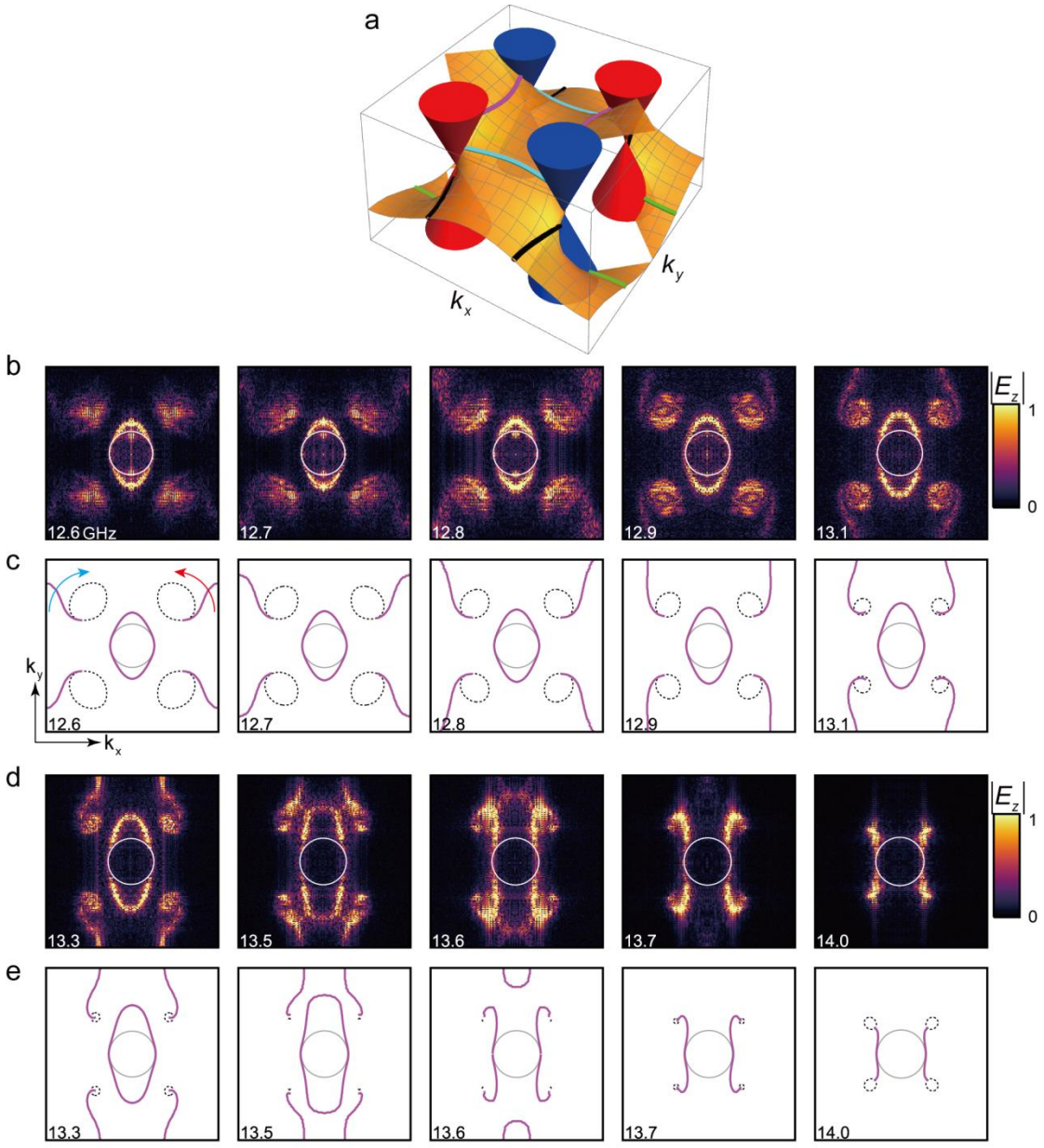


***Figure 3.6 Experimental observation of helicoidal structure of topological surface-state arcs in the ideal photonic Weyl system.***

(a) Map of helicoidal structure of topological surface-state arcs between a pair of Weyl nodes, ideally illustrated by Riemann surface. ± indicates the corresponding topological charge ±1, respectively. (b) and (d) Equi-frequency contour (EFC) ($|E_z|$) measured under setup 'a' from 12.6 GHz to 14.0 GHz. (c) and (e) Bulk (black dashed) and surface (magenta dashed) states simulated in CST microwave studio, correspondingly. Anti-clockwise (red) and clockwise (cyan) arrows indicate topological surface-state arc rotation directions with increasing of frequency

corresponding to positive and negative Weyl nodes, respectively. Central solid circle indicates air equi-frequency contour (air circle) with respect of the frequency labelled. The plotted range for each panel is $[-\pi/a, \pi/a]^2$.

## 3.5 Chessboard like Weyl node interference

Slightly away from the Weyl frequency, the equi-frequency contour of the bulk state consists of four very small spheres for ideal type-I Weyl system (***Figure 3.2***c). It is expected that the interference between them show chessboard like interference pattern in the real space. In application, this observable serves as a spatial-frequency filter with respect of antenna source excitation. To confirm this, interference pattern using setup 'a' at three different frequencies slightly above the Weyl frequency are measured. As shown in ***Figure 3.7***a-c, around the center of the sample, the field pattern forms a periodic square lattice, which slightly increases with the frequency. The plots of the real part of the field in ***Figure 3.7***d-f show that the phase of the field exhibits a checkerboard configuration, which is consistent with the theoretical prediction. Their EFCs (***Figure 3.7***g, h and i), obtained by the Fourier Transform of the complex field pattern, show four circles with radius increasing with frequency. Apparently, the increase of the lattice constant of the field in the real space with frequency is due to the shift of the bulk EFCs towards the origin of the momentum space at higher frequency.

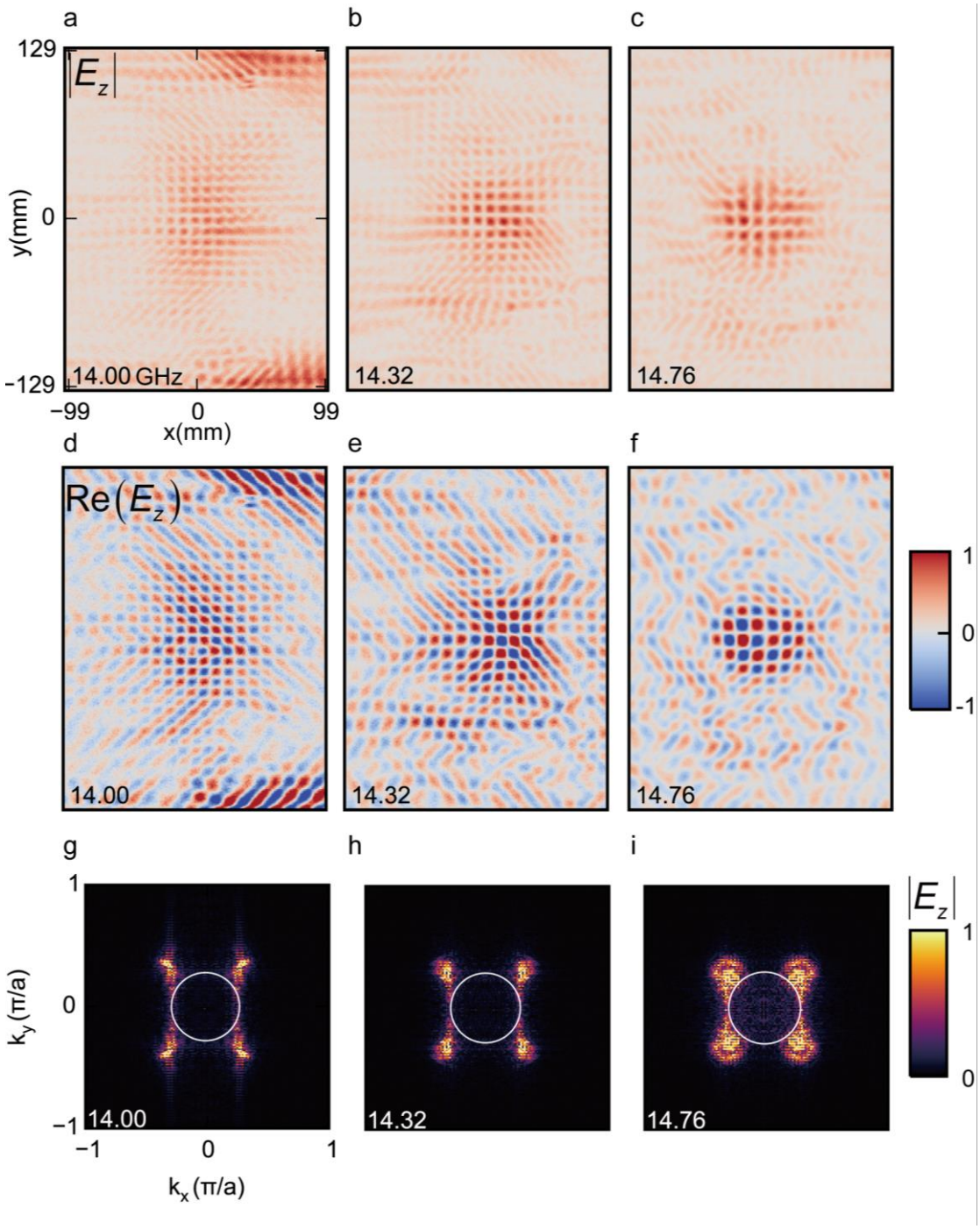


***Figure 3.7 Chessboard like interference between four Weyl nodes.***

(a), (b) and (c) Interference pattern illustrated in amplitude measured under setup 'a' at 14.00, 14.32 and 14.76 GHz. (d-f) similar to (a-c) showing instantaneous field distribution chequered with blue and red. (g), (h) and (i) are the corresponding Fourier transformation. White circle indicates light circle at the corresponding frequency.

## 3.6 Effective medium analysis

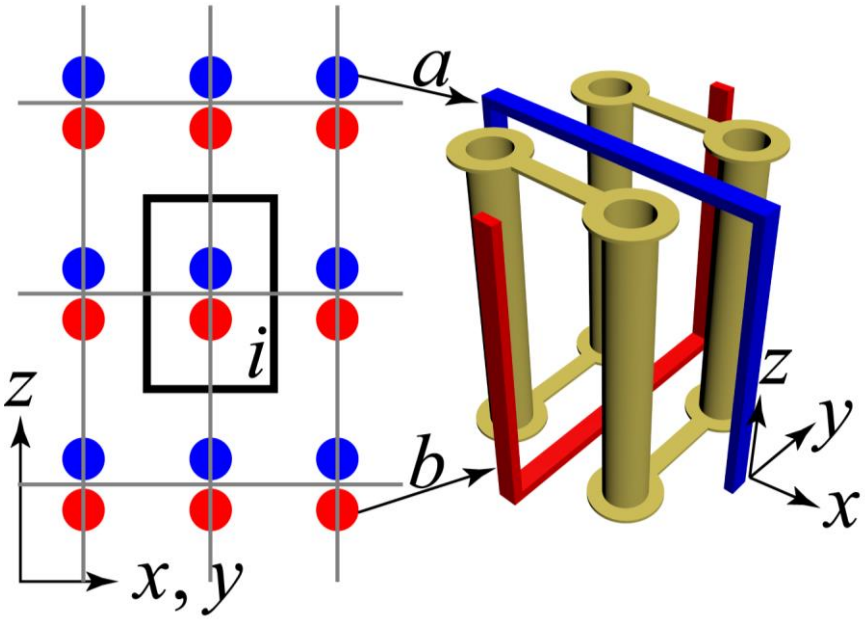


***Figure 3.8 Effective media model simplification.***
The period along *x*, *y* and *z* directions are $a_x=a_y=3mm$ and $a_z=4.5mm$, respectively, where the unit cell is highlighted by black solid rectangle (projected along *x/y* direction). Right hand side inset explains how the realistic structure can be effectively simplified to be two splitting resonator rings (SRRs) colored by red and blue. Each SRR can be regarded as an orbital or sub-lattice to describe the low energy excitation around Weyl points.

The realistic photonic ideal Weyl semimetal consists of periodically buried saddle metallic coils in the substrate materials with dielectric constant of 2.2. Further analyzing its electromagnetic response, we regard it as two splitting resonance rings, which behave like two particles on each lattice, as schematically showed in ***Figure 3.8***.

For the red ring, we have,

$$\begin{cases} E_y \to iH_x \\ H_x \to -iE_y \end{cases} \qquad [3\text{-}1]$$

For the blue ring, we have,

$$\begin{cases} E_x \to iH_y \\ H_y \to -iE_x \end{cases} \qquad [3\text{-}2]$$

By considering the motion of electrons driven by external electromagnetic field on those metallic components [60,61], we obtain,

$$\begin{aligned} red &: -i\omega I + \omega_0^2 q = \frac{1}{L}\left(E_y l + Ai\omega H_x\right) \\ blue &: -i\omega I + \omega_0^2 q = \frac{1}{L}\left(E_x l + Ai\omega H_y\right) \end{aligned} \qquad [3\text{-}3]$$

where $I$ indicates electric current, $L$ is the inductance on the SRRs and $\omega_0 = \frac{1}{\sqrt{LC}}$ with capacitance $C$ is the resonance frequency.

Combing theses with Maxwell equations, a Hermitian Hamiltonian can be obtained to describe the dispersive system,

$$H\psi = N^{-1/2} M N^{-1/2} \psi = E\psi \qquad [3\text{-}4]$$

where,

$$M = \begin{bmatrix} 0 & 0 & 0 & 0 & k_z & -k_y & 0 & 0 & 0 & -i\frac{l}{A} \\ 0 & 0 & 0 & -k_z & 0 & k_x & 0 & 0 & -i\frac{l}{A} & 0 \\ 0 & 0 & 0 & k_y & -k_x & 0 & 0 & 0 & 0 & 0 \\ 0 & -k_z & k_y & 0 & 0 & 0 & 0 & 0 & 0 & 0 \\ k_z & 0 & -k_x & 0 & 0 & 0 & 0 & 0 & 0 & 0 \\ -k_y & k_x & 0 & 0 & 0 & 0 & 0 & 0 & 0 & 0 \\ 0 & 0 & 0 & 0 & 0 & 0 & 0 & 0 & 0 & i\omega_0^2\frac{L}{lA} \\ 0 & 0 & 0 & 0 & 0 & 0 & 0 & 0 & i\omega_0^2\frac{L}{lA} & 0 \\ 0 & i\frac{l}{A} & 0 & 0 & 0 & 0 & 0 & -i\omega_0^2\frac{L}{lA} & 0 & 0 \\ i\frac{l}{A} & 0 & 0 & 0 & 0 & 0 & -i\omega_0^2\frac{L}{lA} & 0 & 0 & 0 \end{bmatrix} \quad [3\text{-}5]$$

$$N = \begin{bmatrix} 1 & 0 & 0 & 0 & 0 & 0 & 0 & 0 & 0 & 0 \\ 0 & 1 & 0 & 0 & 0 & 0 & 0 & 0 & 0 & 0 \\ 0 & 0 & 1 & 0 & 0 & 0 & 0 & 0 & 0 & 0 \\ 0 & 0 & 0 & 1 & 0 & 0 & 0 & 0 & 1 & 0 \\ 0 & 0 & 0 & 0 & 1 & 0 & 0 & 0 & 0 & 1 \\ 0 & 0 & 0 & 0 & 0 & 1 & 0 & 0 & 0 & 0 \\ 0 & 0 & 0 & 0 & 0 & 0 & \omega_0^2\frac{L}{l^2} & 0 & 0 & 0 \\ 0 & 0 & 0 & 0 & 0 & 0 & 0 & \omega_0^2\frac{L}{l^2} & 0 & 0 \\ 0 & 0 & 0 & 1 & 0 & 0 & 0 & 0 & \frac{L}{A^2} & 0 \\ 0 & 0 & 0 & 0 & 1 & 0 & 0 & 0 & 0 & \frac{L}{A^2} \end{bmatrix} \quad [3\text{-}6]$$

and,

$$\psi = \begin{bmatrix} E_x \\ E_y \\ E_z \\ H_x \\ H_y \\ H_z \\ P_x \\ P_y \\ M_x \\ M_y \end{bmatrix} \qquad [3\text{-}7]$$

where $P$ and $M$ are electric and magnetic dipoles, respectively.

In the model, we neglect the ohmic loss and the interactions between intra and inter layers. The correspond constitutive matrices are,

$$\ddot{\varepsilon} = \begin{bmatrix} 1+\frac{l^2}{L}\frac{1}{\omega_0^2-\omega^2} & 0 & 0 \\ 0 & 1+\frac{l^2}{L}\frac{1}{\omega_0^2-\omega^2} & 0 \\ 0 & 0 & 1 \end{bmatrix}$$

$$\ddot{\mu} = \begin{bmatrix} 1+\frac{A^2}{L}\frac{\omega^2}{\omega_0^2-\omega^2} & 0 & 0 \\ 0 & 1+\frac{A^2}{L}\frac{\omega^2}{\omega_0^2-\omega^2} & 0 \\ 0 & 0 & 1 \end{bmatrix}$$

$$\ddot{\xi} = \begin{bmatrix} 0 & \frac{lA}{L}\frac{\omega}{\omega_0^2-\omega^2} & 0 \\ \frac{lA}{L}\frac{\omega}{\omega_0^2-\omega^2} & 0 & 0 \\ 0 & 0 & 0 \end{bmatrix} \qquad [3\text{-}8]$$

We defined them in Maxwell's equation as,

$$\begin{bmatrix} \vec{D} \\ \vec{B} \end{bmatrix} = \ddot{M} \begin{bmatrix} \vec{E} \\ \vec{H} \end{bmatrix} = \begin{bmatrix} \ddot{\varepsilon} & i\ddot{\xi} \\ -i\ddot{\xi} & \ddot{\mu} \end{bmatrix} \begin{bmatrix} \vec{E} \\ \vec{H} \end{bmatrix} \qquad [3\text{-}9]$$

Here, we have already set $\varepsilon_0 = \mu_0 = c = 1$ for simplicity purpose. From the Maxwell's divergence condition,

$$\begin{cases} \nabla \cdot \vec{D} = 0 \\ \nabla \cdot \vec{B} = 0 \end{cases} \qquad [3\text{-}10]$$

One can easily derive that the electromagnetic-coupling-longitudinal mode (EM-LM)

dispersion along $\Gamma M$ direction is described by,

$$\det\begin{bmatrix} \varepsilon_{11} & i\xi_{12} \\ -i\xi_{21} & \mu_{11} \end{bmatrix} = 0 . \qquad [3\text{-}11]$$

The electromagnetic field corresponding to this novel longitudinal mode looks like,

$$\begin{aligned} E_x &= E_y \neq 0 \\ H_x &= H_y \neq 0 \\ E_z &= H_z = 0 \end{aligned} \qquad [3\text{-}12]$$

which is different from normal electric longitudinal mode only having non-zero components in electric field.

Substituting Eq. [3-8] into Eq. [3-11], we get the dispersion of EM-LM is,

$$\omega = \frac{\sqrt{l^2 + L\omega_0^2}}{\sqrt{L - A^2}} \qquad [3\text{-}13]$$

which is a exactly flat band without any dispersion.

An example band dispersion is shown in ***Figure 3.9*** with parameters of $l = 1, A = 0.9, L = 1, \omega_0 = 2$. In crystal, the inter-unit-cell interaction usually bends the longitudinal mode to be dispersive, as schematically shown in ***Figure 3.9*** with respect of the dashed lines. Consequently, the Weyl point will subtly shift away from the original one (solid dot) as indicated by the small circle. Our design possesses dispersive EM-LM

with negative group velocity constructing four type-I Weyl nodes. Interestingly, four symmetry related type-II Weyl nodes can be obtained by adjusting the inter-unit cell interaction.

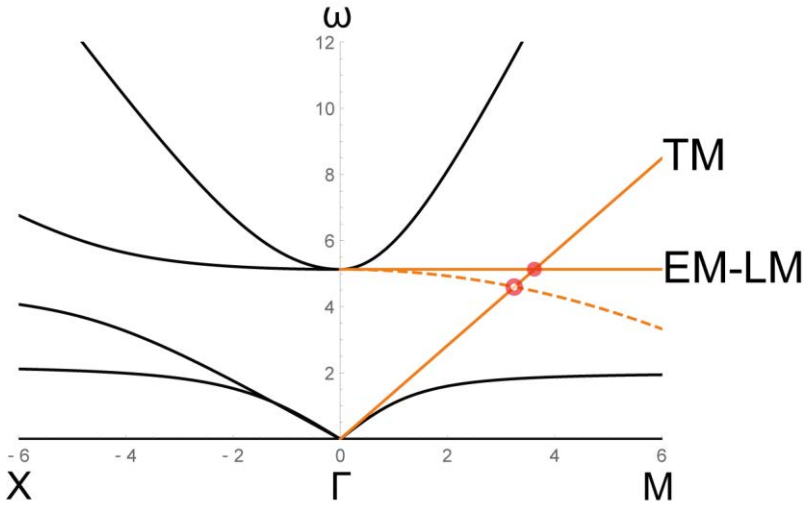


***Figure 3.9 Band structure along X-Γ-M calculated with effective media model.***

TM and EM-LM indicate transverse modes and electromagnetic-coupling-longitudinal mode (EM-LM), respectively. Their crossing is Weyl point (solid dot). In realistic structure crystal non-local effect makes the longitudinal mode dispersive with negative group velocity (dashed line) and moves the crossing to a new position, as indicated by the white dot.

## 3.7 Eigen electric field and symmetry analysis

As mentioned above, the Weyl state space is spanned by two modes, which are transverse mode (TM) and electromagnetic-coupling-longitudinal mode (EM-LM). For the transverse mode, most part of the electric field will be perpendicular to $\vec{k}_{\Gamma M}$, while in EM-LM the electric field majorly orient along $\vec{k}_{\Gamma M}$. After analyzing eigen electric

field simulated in CST, the prediction is confirmed as shown in ***Figure 3.10***. The transverse mode can be regarded as right circular polarized (RCP), with increasing phase, the electric field rotates clockwise. Overall, most of the energy concentrates on the margin of in the primitive unit cell. Comparatively, electric energy density of EM-LM is higher in the center (saddle like metallic structure) region, as shown in ***Figure 3.10***c. Magnetic fields (H fields) show similar behaviors and are not shown.

The saddle like structure possesses $D_{2d}$ point group, along $\Gamma M$ a two-fold rotation is preserved. Here, the transverse mode and EM-LM are belong two different classes of the two-fold rotation symmetry. Thus, the band repulsion between them is forbidden. As shown in ***Figure 3.10***b and c, they have different eigenvalues,

$$\begin{aligned} R_{\Gamma M}(\pi) E_{TM} &= -E_{TM} \\ R_{\Gamma M}(\pi) E_{EM-LM} &= E_{EM-LM} \end{aligned} \qquad [3\text{-}14]$$

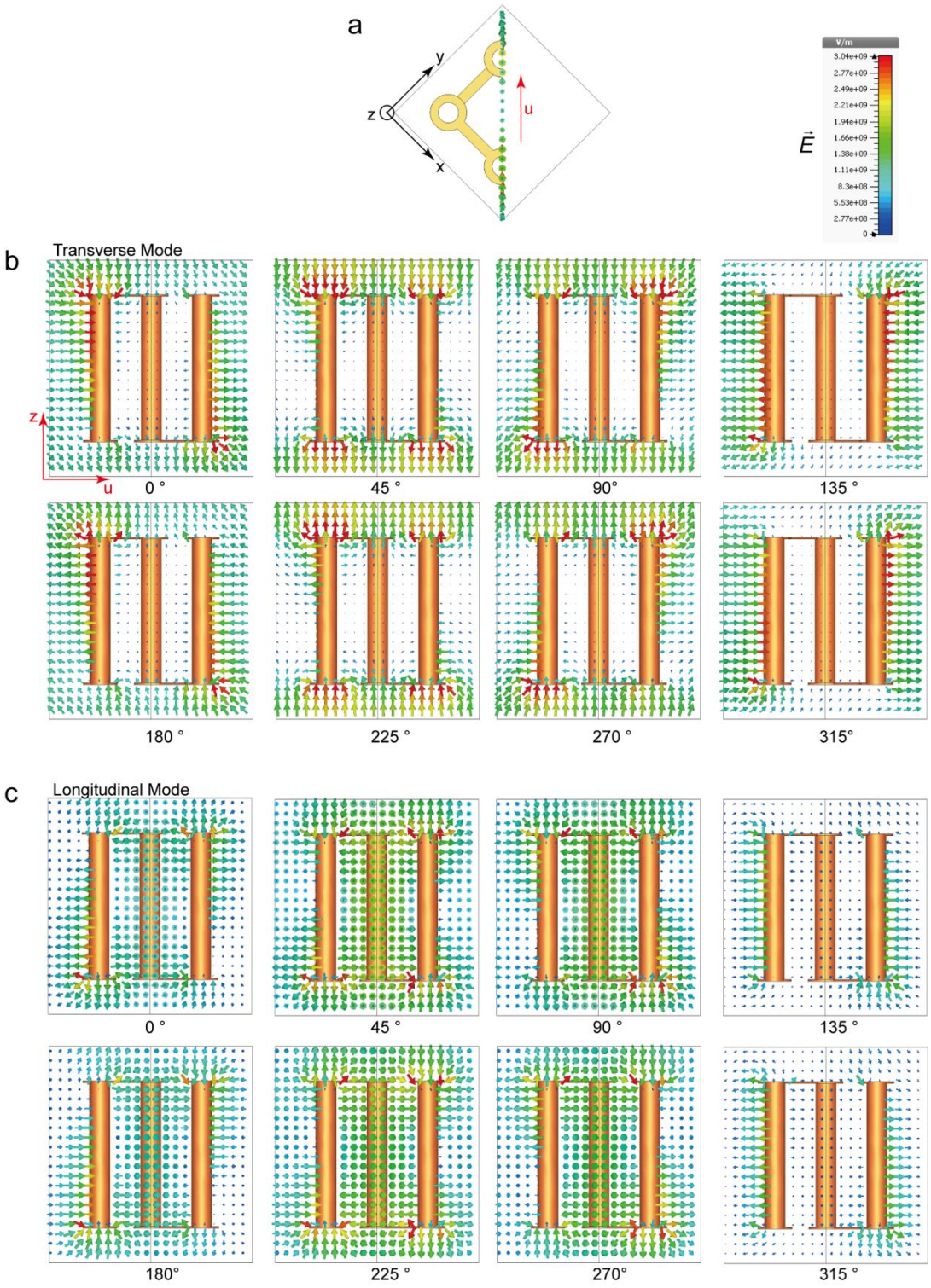


***Figure 3.10 Eigen electric field profiles for both transverse and longitudinal mode.***

(a) Cutting plane of the primitive unit cell, on which electric field is exported. (b) Eigen-electric field profile of transverse mode with respect

of different phases from 0-315 degree in the step of 45 degree. (c) Similar to (B) but for the electric-magnetic coupling longitudinal mode (EM-LM).

## 3.8 Energy-momentum map measured from near field scanning

Having confirmed the helicoid nature of the surface state arcs, we now look into the dispersion of the bulk and surface states along four representative momentum cuts, which provide further insight into the bulk-surface correspondence hosted by the ideal Weyl meta-crystal. Two of the band dispersions are taken along two straight momentum cuts passing through the Weyl points in the horizontal and vertical direction, by fixing $k_y = 0.4\pi / a$ (cut-I) and $k_x = 0.4\pi / a$ (cut-III), respectively (***Figure 3.11***c). Along the horizontal momentum cut, it is observed that a surface state connects directly between the two Weyl points within the BZ (***Figure 3.11***a, cut-I), which is reminiscent of the bearded edge state connection between the Dirac points in graphene. On the other hand, along the vertical momentum cut, the two Weyl points are connected by a surface state crossing the boundary of BZ (***Figure 3.11***a, cut-III), which reminds of the edge state connection in graphene along the zigzag edge [68,69]. For the other two momentum cuts slightly tilted from the horizontal and vertical directions, since they do not pass through the Weyl points, a complete band gap opens up in each band structure. In each case, it is observed that a single surface state connects between the upper and lower bulk bands across the bandgap, indicating the nontrivial topology of the band structures. The

numerically simulated dispersion relation along all the four momentum cuts (***Figure 3.11***b) agree very well with the experimental results (***Figure 3.11***a), further revealing the intriguing bulk surface correspondence present in the Weyl system.

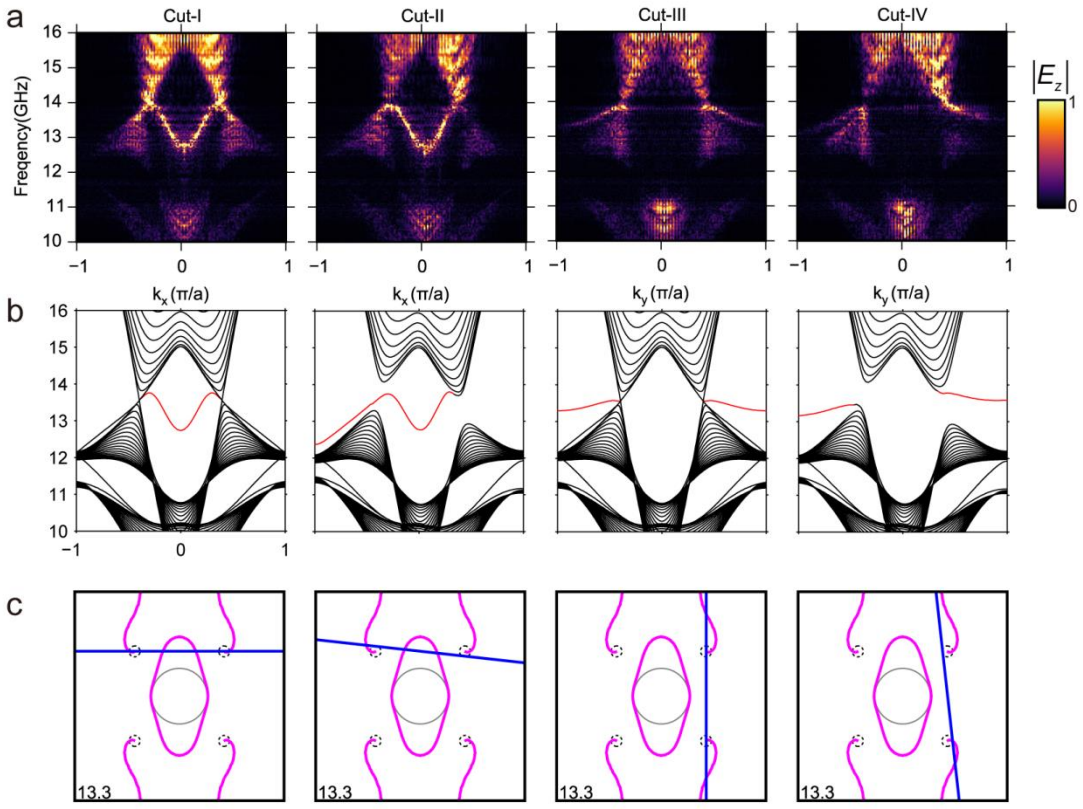


***Figure 3.11 The measured and simulated dispersions along four different momentum cuts.***

(a) The measured band structures along the momentum cuts indicated by (c). (b) The simulated band structures where the surface states are drawn in red. Surface states in cut-I and cut-III show strong resemblance to the bearded and zigzag edge states of graphene nanoribbon, respectively. (c) The numerically calculated equi-frequency contour at 13.3 GHz where the momentum cuts (in blue) for the dispersions shown in (a) and (b) are indicated.

## 3.9 Tight binding analysis

The tetragonal lattice consists of two inequivalent orbitals A and B displaced along *z* axis by $2\delta$ as shown in ***Figure 3.8***. In *x*-*y* plane the 3D meta-crystal can be viewed as a stack of bilayer square lattice. The Hamiltonian including intra-layer as well as inter-layer hopping reads [70],

$$\begin{aligned} H = & \sum_{i,(a\leftrightarrow b)} \lambda_a a_{r_i}^{\dagger} a_{r_i} + \sum_{i,(a\leftrightarrow b)} \left( \lambda_{a,\mu} a_{r_i}^{\dagger} a_{r_i+p_\mu} + H.c. \right) \\ & + \sum_i \left( \xi a_{r_i}^{\dagger} b_{r_i} + H.c. \right) + \sum_i \left( \xi_{\pm\mu} a_{r_i}^{\dagger} b_{r_i \pm p_\mu} + H.c. \right) \end{aligned} \qquad [3\text{-}15]$$

Where $\mu = x, y, z$ , $i$ specifies each lattice and $a, b$ label the two inequivalent orbitals. We assume the two orbitals have the same on-site potential through $\lambda_a = \lambda_b = \lambda$ . The second term in the first line corresponds to the nearest-neighbor hopping connecting the same orbital on different lattices. Strong anisotropy of the SRR (orbital) characterizes direction-dependent hopping parameters, such as $\lambda_{ax} \neq \lambda_{ay} \neq \lambda_{az} \left( a \leftrightarrow b \right)$ . From symmetry analysis of the unit cell, it is reasonable to define $\lambda_{ax} = \lambda_{by} = \lambda_1, \lambda_{bx} = \lambda_{ay} = \lambda_2$ . The second line in Eq. [3-15] represents coupling between the two orbital, where the first term shows the case when the two orbitals reside on the same lattice. In the second term, those hopping parameters can be further reduced to $\xi_{\pm x} = \xi_{\pm y} = \xi_{xy}$ . With above constraints from our structure, the tight binding Hamiltonian manifestly preserves crystal symmetry, especially for $D_{2d}$ point group

symmetry. The corresponding Bloch Hamiltonian is obtained by Fourier transformation,

$$
\begin{aligned}
&H_{\vec{k}} = \sum_{i=0,x,y,z} q_i\left(\vec{k}\right)\sigma_i \\
&q_0 = \lambda + \sum_{\mu=x,y,z}\left(\lambda_{a,\mu} + \lambda_{b,\mu}\right)\cos\left(k_\mu p_\mu\right) \\
&q_x = \xi\cos\left(2k_z\delta\right) + 2\xi_{xy}\cos\left(2k_z\delta\right)\sum_{\mu=x,y}\cos\left(k_\mu p_\mu\right) + \sum_{\upsilon=\pm}\xi_{\upsilon z}\cos\left[k_z\left(p_z - 2\upsilon\delta\right)\right] \\
&q_y = \xi\sin(2k_z\delta) + 2\xi_{xy}\sin\left(2k_z\delta\right)\sum_{\mu=x,y}\cos\left(k_\mu p_\mu\right) - \sum_{\upsilon=\pm}\upsilon\xi_{\upsilon z}\sin\left[k_z\left(p_z - 2\upsilon\delta\right)\right] \\
&q_z = \sum_{\mu=x,y,z}\left(\lambda_{a,\mu} - \lambda_{b,\mu}\right)\cos\left(k_\mu p_\mu\right)
\end{aligned}
\qquad [3\text{-}16]
$$

Where $\sigma_i$ is the Pauli matrix acting on sub-lattice space. This a sum of anti-commuting matrices, so that the energies can be written immediately,

$$\varepsilon_k = q_0 \pm \sqrt{\sum_{\mu=x,y,z} q_\mu^2} \qquad [3\text{-}17]$$

The band degeneracy must occur when $q_{\mu=x,y,z} = 0$. On the plane $k_z = 0$, $q_y = 0$. $q_z = 0$ shows $|k_x| = |k_y|$. Substitute it to $q_x = 0$, we obtain the coordinates of four Weyl points,

$$|k_x| = |k_y| = \frac{1}{p_x}\left|\arccos\left(-\frac{\xi + \xi_{+z} + \xi_{-z}}{4\xi_{xy}}\right)\right| \qquad [3\text{-}18]$$

which means the positions of Weyl points are mainly determined by coupling terms between the two orbitals.

## 3.10 Discussion and conclusion

The ideal Weyl system can also be realized in other space groups, such as P-42m (No. 111), where there possibly are existing four symmetry related type-II Weyl points (or transition between type-I and type-II) with few adjusting the structure parameters.

The observation can also be readily moved to terahertz range. For the optical band, an all dielectric realization with the same point group greatly facilitating nano-fabrication is promising with machine-learning [71,72] finding a set of appropriate parameters, as all dielectric induced bi-anisotropic effect has been proposed [44].

In this chapter, we observed for the first time to our knowledge, an ideal Weyl system which has not been realized previously in either condensed matter or classical systems. Ideal Weyl system opens up new opportunities for studying the intriguing physics [5]. In the absence of translation symmetry, Weyl nodes will be gapped and hybridized. Since these nodes are analogous to valley degree of freedoms in semiconductors, pump of photons between valleys of opposite chirality will show new physics. Introducing a synthetic vector potential (such as applying a uniaxial strain) in ideal Weyl system, Berry curvature induced anomalous velocity of wave packet (soliton in nonlinear context) could be observed in three dimensions. Topological gapless phase bridges topological trivial and nontrivial insulator phase. When Weyl nodes migrate across FBZ and annihilate with opposite chirality partners in pairwise fashion, distinct topological

phases occur, such as photonic topological Dirac phase and photonic topological insulator.

# Chapter 4. Photonic Dirac points protected by electromagnetic duality

Photonic crystal realizations of Dirac degeneracies are protected by various space symmetries [73], where Bloch modes span the spin and orbital subspaces. Here, we theoretically show that Dirac points can also be realized in effective media through the intrinsic degrees of freedom in electromagnetism under electromagnetic duality [39]. A pair of spin polarized Fermi arc like surface states is observed at the interface between air and the Dirac metamaterials. These surface states show linear k-space dispersion relation, resulting in nearly diffraction-less propagation. Furthermore, eigen reflection fields show the decoupling process from a Dirac point to two Weyl points. We also find the topological correlation between a Dirac point and vortex/vector beams in classic photonics. The theoretical proposal of photonic Dirac point lays foundation for unveiling the connection between intrinsic physics and global topology in electromagnetism [74]. This chapter includes passages from the publication [39].

## 4.1 Introduction

Dirac point is a four-fold band crossing defined in three dimensional momentum space,

away from which energy band exhibits linear dispersion along arbitrary direction. As a central gapless topological phase, Dirac semimetal bridges conventional insulator, topological insulators and Weyl semimetals. By breaking either time-reversal (*T*) or inversion symmetry (*P*), it may split into two opposite Weyl points (Weyl semimetal). Electronic realizations of Dirac point can be classified into two mechanisms, which are 'band inversion' and 'symmetry enforced', respectively [5]. In photonics, the latter mechanism is mostly used. Since Kramers theorem does not work in bosonic system with *T* constraint of $T^2 = 1$, the combined operations of *T* and *P* cannot offer double degeneracy in the reciprocal space. Thus, four-dimension degeneracy of Dirac point has to rely on various space symmetries in photonic crystals, where spatial degrees of freedom play vital roles.

## 4.2 Three dimensional Dirac points arising from intrinsic degrees of freedom

By studying the intrinsic polarization degrees of freedom in electromagnetism, we theoretically demonstrate a way to design photonic Dirac points protected by electromagnetic duality symmetry in a medium with homogeneous effective electromagnetic properties [22,44]. At the interface between air and the Dirac metamaterials, there exists spin dependent Fermi arc like surface states. Because of the linearity of their *k*-space dispersion, the surface waves propagate nearly without

diffraction, which is significant for the information transport and imaging applications. Due to the underlying topological relations, the topological charges discovered in classic photonics, such as vector/vortex beams, can be generated through the interaction of light with photonic Dirac points.

Here we consider a uniaxial metamaterial with realistic resonant features in both permittivity and permeability. Specifically, the effective parameters of Dirac metamaterials are taking the form of $\ddot{\varepsilon} = diag\{\alpha, \alpha, \varepsilon_z\}, \ddot{\mu} = diag\{\varsigma, \varsigma, \mu_z\}$ . For simplicity purpose we assume $\alpha = \varsigma = constant$ and,

$$\varepsilon_z = 1 + f_1\omega_0^2 / (\omega_0^2 - \omega^2), \mu_z = 1 + f_2\omega^2 / (\omega_0^2 - \omega^2). \qquad [4\text{-}1]$$

where $\omega_0$ indicates the resonance frequency and coefficients $f_1$ and $f_2$ are constants determined by the structure parameters which are adjustable. The resonance along *z* direction for both permittivity and permeability indicate that there exist two bulk plasmon modes, a longitudinal electric mode, and a longitudinal magnetic mode. From Eq. [4-1], it is straightforward to show that the degeneracy of the two longitudinal modes can be reached by setting $f_2 = 1 - 1/(1 + f_1)$ .

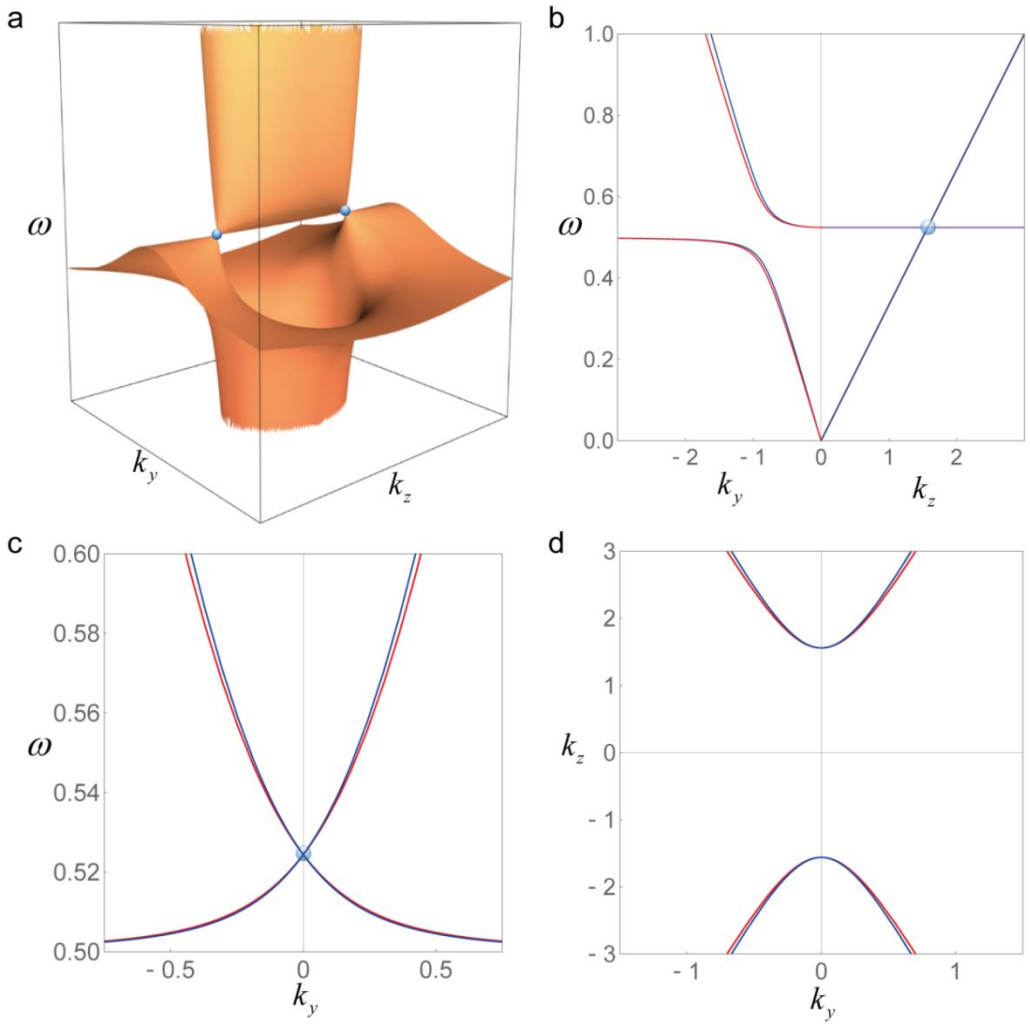


***Figure 4.1 Band structure of bulk states with α=ζ=3.***
(a) Effective bulk band structure on the $k_y$-$k_z$ plane with the Dirac points marked by blue sphere. (b) The dispersion relation along $k_y$ and $k_z$ direction respectively, while (c) gives the dispersion along $k_y$ direction with $k_z$ fixed at the Dirac point. In both (b) and (c) the Dirac Points are marked with the blue points. (d) Equi-frequency contour at a frequency below Dirac points, which indicates the hyperbolic property of the material corresponds to the Dirac cone. All units are arbitrary units.

The band structures for a specific set of realistic parameters satisfying the above condition are shown in ***Figure 4.1***. ***Figure 4.1***a shows the plot of band structures in the $k_y$ - $k_z$ plane, where two bands are nearly overlapping with each other. There are two

four-fold degeneracy points symmetrically displaced on $k_z$ axis, as marked by blue spheres. These two points are Dirac points that form the central focus of our study. ***Figure 4.1***b gives the dispersion relation of the material along $k_y$ and $k_z$ directions with $k_x$ equaling to zero. In the $k_z$ direction, the two longitudinal modes and the two transverse modes are perfectly degenerate, respectively, across the whole frequency range. The band crossing between the two transverse modes and the two longitudinal modes is guaranteed by the orthogonality between them. Very recently, the crossing between a single longitudinal plasmon mode and one circular polarization mode in hyperbolic chiral metamaterials [36] and magnetized plasma [34] is found to show topological nature, exhibiting exotic properties of Weyl quasi-particles.

***Figure 4.1***c shows the linear dispersions along $k_x$ or $k_y$ direction across the Dirac point, where bands are also degenerate in a frequency range around Dirac point. The linear dispersions along all directions reveal a massless Dirac collective excitation. In the momentum space, EFC corresponding to a frequency below the Dirac points is shown in ***Figure 4.1***d. One could see the EFC possesses double hyperbolas ($\varepsilon_z < 0, \mu_z < 0$), which is characteristic of a double hyperbolic metamaterial (DHM).

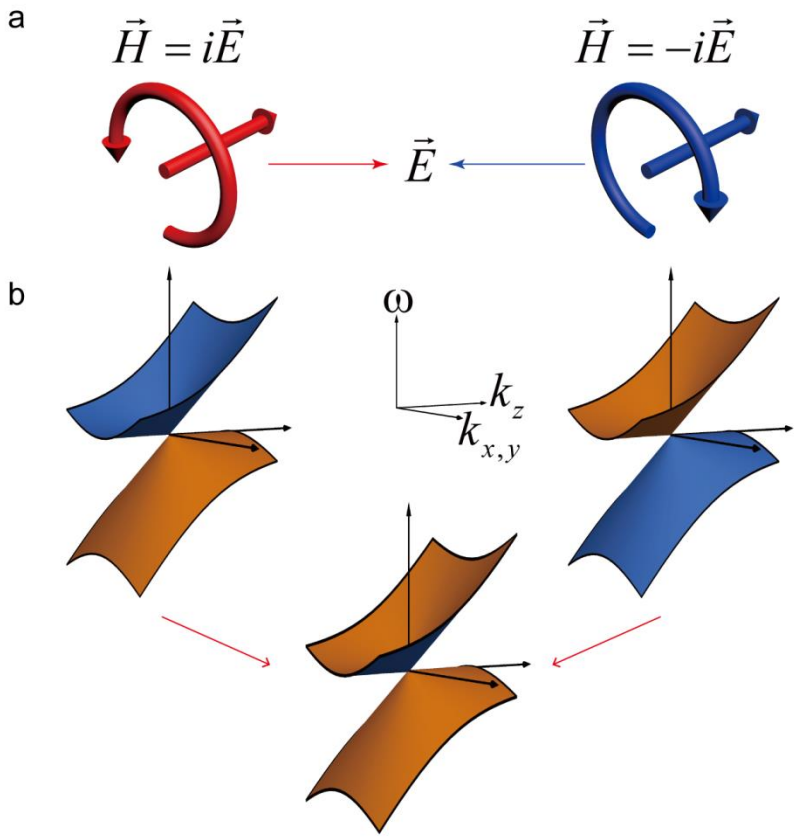


***Figure 4.2 Decouples of photonic Dirac point to two compensated Weyl points.***

(a) Two compensated Weyl points are constructed from LCP/RCP and the corresponding longitudinal modes. (b) Schematic view of E field corresponding to the Weyl points. Left/right circular polarization (LCP/RCP) and electric/magnetic longitudinal modes (L1/L2) are shown in red and blue, respectively.

Here, the 3D Dirac points are protected by electromagnetic duality $(\vec{\varepsilon} = \vec{\mu})$—an internal symmetry of the electromagnetism responsible for electromagnetic fields interchanging, such as $\vec{H} \leftrightarrow \pm i\vec{E}$ . Under the following set of basis,

$$\begin{aligned} &LCP: (\vec{E} = (\hat{x} - i\hat{y})/\sqrt{2}, \vec{H} = i\vec{E}), L_1(\vec{E} = \hat{z}, \vec{H} = i\vec{E}) \\ &RCP: (\vec{E} = (\hat{x} + i\hat{y})/\sqrt{2}, \vec{H} = -i\vec{E}), L_2(\vec{E} = \hat{z}, \vec{H} = -i\vec{E}) \end{aligned} \quad [4\text{-}2]$$

The Dirac Hamiltonian takes a block-diagonal form consisting of two Weyl degeneracies,

$$H_D\left(\vec{k}\right)=\begin{bmatrix} H_W\left(\vec{k}\right) & \\ & H_W^*\left(\vec{k}\right) \end{bmatrix}. \qquad [4\text{-}3]$$

where the induced Weyl Hamiltonian, arising from a longitudinal mode and a circularly polarized transverse mode [34], is given by

$$H_W\left(\vec{k}\right)=\begin{bmatrix} d_z k_z & d_x k_x - i d_y k_y \\ d_x k_x + i d_y k_y & 0 \end{bmatrix}, \qquad [4\text{-}4]$$

where $d_i$ is the corresponding velocity determined by specific material parameters. Each mentioned longitudinal mode combining with a transverse mode (LCP/RCP) span a two-dimension spin space. As schematically shown in ***Figure 4.2***, one Dirac point could be decoupled to two Weyl points with the chirality being $\pm 1$ respectively. Here, the chirality of each Weyl node is determined by the intrinsic spin $s=\pm 1$ of transverse modes, because both longitudinal modes are spinless $(s=0)$.

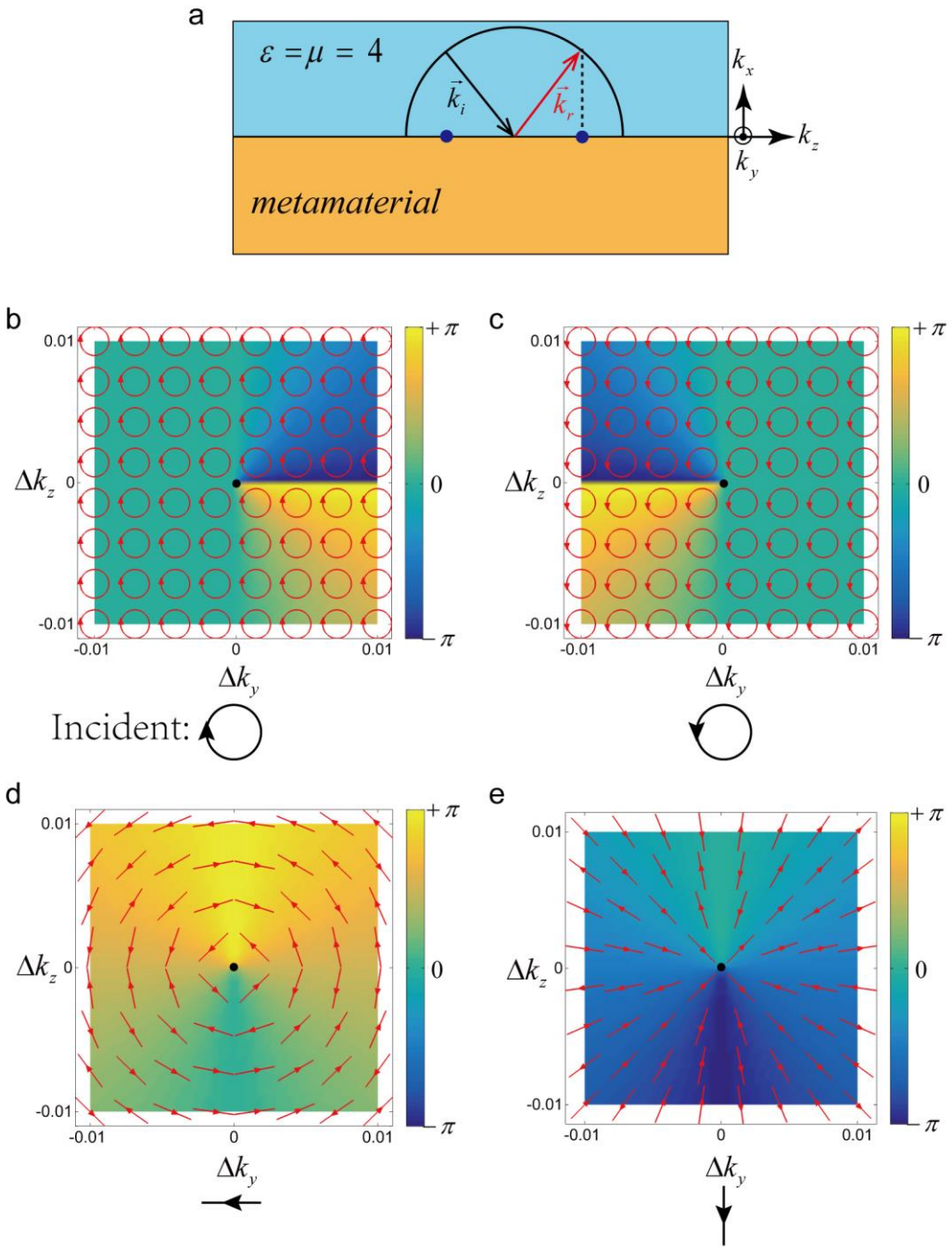


***Figure 4.3 Reflection spectrum around a Dirac point.***

(a) Configuration of the reflection calculatioin and Dirac points (two dots) in momentum space. One plane wave is incident $k_i$ from the backgroud material $y>0$ and totally reflected $k_r$ back at the interface as indicated. (b) and (c) show the reflected E-field with respect of right/left circular polarization incidence, respectively. (d) and (e) are similar to (b) and (c) with the incidences of two orthogonal linear polarizations. The incident

polarization state is illustrated on the bottom of each panel.

Angle-resolved reflectance spectrum gives us an intuitive way to show how the Dirac node decouples into two complex-conjugation related Weyl points. As shown in ***Figure 4.3***a, a plane wave with a specific polarization state is illuminated around the Dirac node (the blue points at the interface). Here we could assume an ideal case that the overall system is under electromagnetic duality close to the degenerate point. The Dirac metamaterials $\vec{\varepsilon} = \vec{\mu} = \{k_D, k_D, 0\}$ with Dirac points $(0, 0, \pm k_D)$ is located at $y < 0$, while the $y > 0$ semi-space is occupied by an isotropic medium with $\varepsilon^{iso} = \mu^{iso} > k_D$. ***Figure 4.3***b and c show the reflected polarization states and phases with RCP/LCP incidence, respectively. Obviously, circular polarizations are the eigenstates of the system due to the electromagnetic duality. In the momentum space, one anticlockwise loops around the Dirac point with RCP/LCP incidence acquires a $2\pi / -2\pi$ reflection phase leading to generation of vortex beam in reflection, which directly maps out the chirality of each Weyl points contained in the Dirac degeneracy. With linear polarization incidence, the reflection field is symmetric about the $\Delta k_z$ axis as shown in ***Figure 4.3*** d and e. This can be understood as the topological charge of a Dirac node being 0. Interestingly, angular and radial vector beams are generated by a Gaussian beam incidence with TE and TM polarization states, respectively (***Figure 4.3***d and e). Therefore, 3D photonic Dirac points are topologically related to the vector/vortex photonics. Dirac point degeneracy provides a novel method in generating vector and

vortex beams.

## 4.3 Topological surface-state arcs in three dimensional Dirac metamaterials

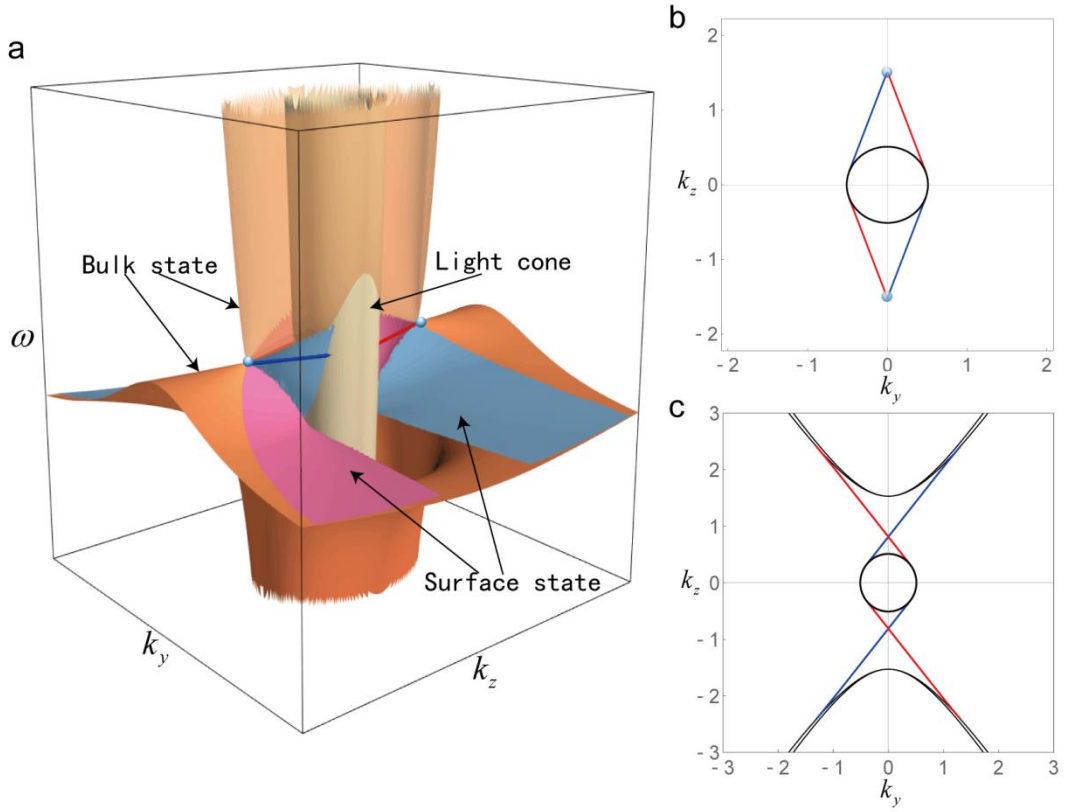


***Figure 4.4 Bulk and surface states of the effective medium.***
(a) 3D band structures of bulk and surface states of the effective medium. Spin-up (Spin-down) surface state between two Dirac points and vacuum is indicated by the red (blue) surface. The blue and red lines highlight the photonic 'Fermi arcs' at Dirac point. Equi-frequency contours at two different frequencies could be seen in (b) and (c) corresponding to the frequency at Dirac point and below it, respectively. The red and blue lines in (b) and (c) represent the spin up and spin down topological surface states, while the black lines represent the effective material and vacuum bulk states.

As mentioned above, Dirac point consists of two opposite Weyl points. A landmark of Weyl topological phase is the existence of Fermi arcs connecting projections of pairs of Weyl points. Therefore, a topologically nontrivial Dirac point should exhibit double Fermi arcs, which have been observed in electronic systems [75]. Here we calculate the topological surface states between the Dirac metamaterials and air, where air naturally has electromagnetic duality symmetry $\left(\varepsilon^{air}=\mu^{air}=1\right)$. Furthermore, owing to the transverse nature of electromagnetic waves, propagation of light in free space possesses Berry curvature in the momentum space given by $\vec{\Omega}=\sigma\vec{k}\Big/\left|\vec{k}\right|^3$, where $\sigma=\pm1$ indicates spin of RCP/LCP [76]. At the origin of momentum space, there exist singularities of Berry curvature, so called "Dirac monopoles". For LCP, the origin behaves like a sink of Berry flux, while for RCP it is the source. This nontriviality leads to the well-known spin-dependent Chern numbers 2σ. Thus, air provides topological nontriviality for the Fermi arcs connection.

As the duality symmetry between $\ddot{\varepsilon}$ and $\ddot{\mu}$ is preserved in both media, at the interface formed by these two media, the two spin states can be decoupled. One can analyse them separately. In ***Figure 4.4***a, we show two pairs of spin polarized Fermi arc like surface states. Each pair of surface states consists of spin $\sigma=+1$ (pink surface) and spin $\sigma=-1$ (cyan surface) surface states. ***Figure 4.4***b shows EFC of the Fermi arc like surface states at Dirac points. From each Dirac point, there are two "Fermi arcs"

connecting to the air light circle. In ***Figure 4.4***c, EFCs at a frequency below Dirac points is illustrated. Interestingly, by setting $\varepsilon_z = \mu_z = \beta$ with $(\alpha > 1, \beta \le 0)$, these "Fermi arcs" geometrically appear as straight line segments tangentially connecting air-circle and DHM-hyperbolas with linear dispersion relation in *k* space,

$$k_z = \pm \frac{\sqrt{\alpha^2 - 1}}{\sqrt{1 - \alpha\beta}} k_y \pm \frac{\sqrt{\alpha^2 - \alpha\beta}}{\sqrt{1 - \alpha\beta}} \qquad [4\text{-}5]$$

and the lengths of the segments are strictly related to the decay constant in both air and DHM. Moreover, the topological nontriviality of Dirac gapless phase can also be studied on $k_z \left(\in (-k_D, k_D)\right)$ fixed plane, where a 2D $Z_2$ invariant can be defined, and each $k_z$ fixed cut can be regarded as a 2D photonic topological insulator [76].

In order to demonstrate the topological protection and spin locking of the surface states, a full wave 3D simulation is performed using CST microwave studio with parameters of $\alpha = 3, \beta = 0$ (at the Dirac point frequency). The configuration is built by a cuboid-shaped Dirac metamaterials surrounded by air. A small port is positioned at the interface as the radiation source. ***Figure 4.5***a and b show the backscattering immune transportation of spin-dependent surface waves helically bending around *z*-invariant sharp corners, indicating the one way surface state is left/right handed polarization. These demonstrations confirm the robustness of spin "Fermi arcs" in the photonic Dirac metamaterials.

Another interesting property arising from linear *k*-space dispersion is the near diffraction-less propagation. To demonstrate this effect, we analyze the transverse profile of the propagating surface wave by setting $\alpha = 2, \beta = -3$. CST simulation in ***Figure 4.5***c shows the intensity of localized surface wave. At the two cross section planes indicated by A and B, the Gaussian-like beam profiles in real space are nearly diffraction-less, as shown in ***Figure 4.5***d. After propagating $\Delta L = 7\lambda$ in $z$ direction, the Full Width at Half Maximum (FWHM) of the surface beam only spreads $\Delta X \approx 1/40\ \lambda$.

Exploration of topological photonics protected by electromagnetic duality symmetry has introduced a number of intriguing optical phenomena [22,44,77]. However, due to the complexity of material realization and finely tuned photonic crystal design, up to now the experimental observation stills remains challenging, particularly in 3D. It is expected that well developed metamaterials theory and finely designed high-permittivity metacrystals [44] can provide an electromagnetic duality platform to discovery more new photonic topological phases.

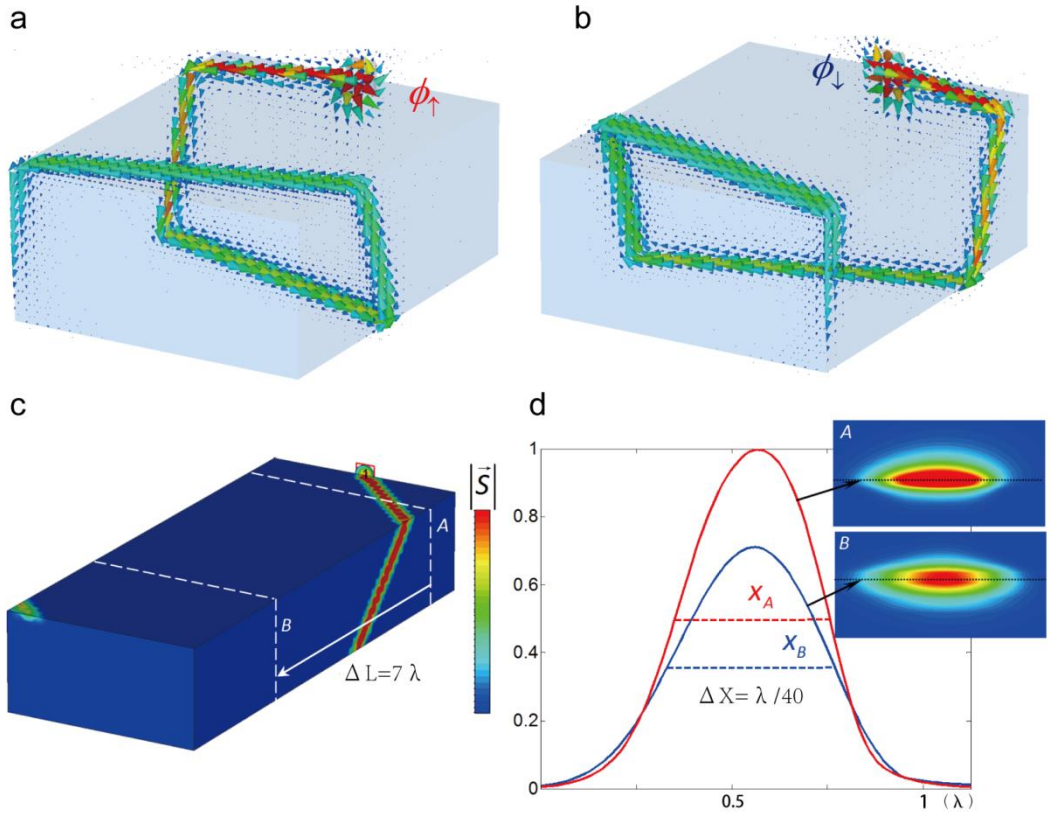


***Figure 4.5 Surface states indicated by power flow simulated in 3D by CST time domain.***

The (a) spin-up and (b) spin-down surface states propagate helically along *z* direction clockwise and anti-clockwise respectively, on the surface of cuboid effective material which is capsulated by vacuum. (c) Surface states simulated in 3D by CST time domain. The dashed white lines (A and B) show the cutting plane for (d) to confirm the nearly diffraction-less propagation of the surface states. By cutting the 3D field at A and B, two energy spatial distribution profiles are obtained. Further analyzing the FWHM of Gaussian style line graphs shows us the nearly diffraction-less property.

## 4.4 Effective Hamitonian of the theoretical model

Around the Dirac point $(0,0,k_D)$ with permittivity/permeability under electromagnetic duality symmetry (such as $\ddot{\varepsilon} = \ddot{\mu} = diag\{1,1,2\delta\omega + O(\delta\omega)^2\}$, where $\delta\omega$ is the

frequency shift away from the Dirac point frequency), a first-order perturbative Hamiltonian from analyzing Maxwell equation can be derived as [61],

$$H_I = \begin{bmatrix} 0 & 0 & 0 & 0 & k_z & -k_y & 0 & 0 \\ 0 & 0 & 0 & -k_z & 0 & k_x & 0 & 0 \\ 0 & 0 & 0 & k_y & -k_x & 0 & 0 & 0 \\ 0 & -k_z & k_y & 0 & 0 & 0 & 0 & 0 \\ k_z & 0 & -k_x & 0 & 0 & 0 & 0 & 0 \\ -k_y & k_x & 0 & 0 & 0 & 0 & 0 & 0 \\ 0 & 0 & 0 & 0 & 0 & 0 & 0 & 0 \\ 0 & 0 & 0 & 0 & 0 & 0 & 0 & 0 \end{bmatrix} \quad [4\text{-}6]$$

By choosing an appropriate set of bases within a four dimensioanl Hilber spaces as,

$$\begin{aligned} |\psi_1\rangle &= \left[\frac{1}{2}, -\frac{i}{2}, 0, \frac{i}{2}, \frac{1}{2}, 0, 0, 0\right] \\ |\psi_2\rangle &= \left[0, 0, \frac{1}{2}, 0, 0, \frac{i}{2}, \frac{i}{2}, -\frac{1}{2}\right] \\ |\psi_3\rangle &= \left[\frac{1}{2}, \frac{i}{2}, 0, -\frac{i}{2}, \frac{1}{2}, 0, 0, 0\right] \\ |\psi_4\rangle &= \left[0, 0, \frac{1}{2}, 0, 0, -\frac{i}{2}, \frac{i}{2}, \frac{1}{2}\right] \end{aligned} \quad [4\text{-}7]$$

where $|\psi_i\rangle = \left[\vec{E}, \vec{H}, dP_z/dt, dM_z/dt\right]$ and auxiliary component $P_z / M_z$ is electric/magnetic moment, the effective Hamiltonina can be built as $H_{D,ij}\left(\vec{k}\right) = \langle\psi_i | H_I | \psi_j\rangle$, leading to a block-diagonal form,

$$H_D\left(\vec{k}\right) = \begin{bmatrix} H_W\left(\vec{k}\right) & \\ & H_W^*\left(\vec{k}\right) \end{bmatrix} \quad [4\text{-}8]$$

where,

$$H_W\left(\vec{k}\right)=\begin{bmatrix} k_z & \frac{1}{2}\left(-k_x-ik_y\right) \\ \frac{1}{2}\left(-k_x+ik_y\right) & 0 \end{bmatrix} \qquad [4\text{-}9]$$

representing an induced Weyl Hamiltonian. As schematically shown in ***Figure 4.2***, one Dirac point could be decoupled to two Weyl points with the chirality being $\pm 1$ respectively.

The other Dirac point symmetrically displaced on $\left(0,0,-k_D\right)$ can be obtained after time-reversal operation of the present one. At the Dirac point frequency, EFC relation reads as, $k_x=-i\left|k_y\right|$. After substituting it into the Dirac Hamiltonian, the tangential electrical field eigen states are shown in ***Figure 4.6***, from boundary condition analysis (tangential electric field matching $E^i_{y,z}+E^r_{y,z}=E^t_{y,z}$), which can clearly explain the reflection vortex pantern of RCP/LCP incidence (***Figure 4.3***).

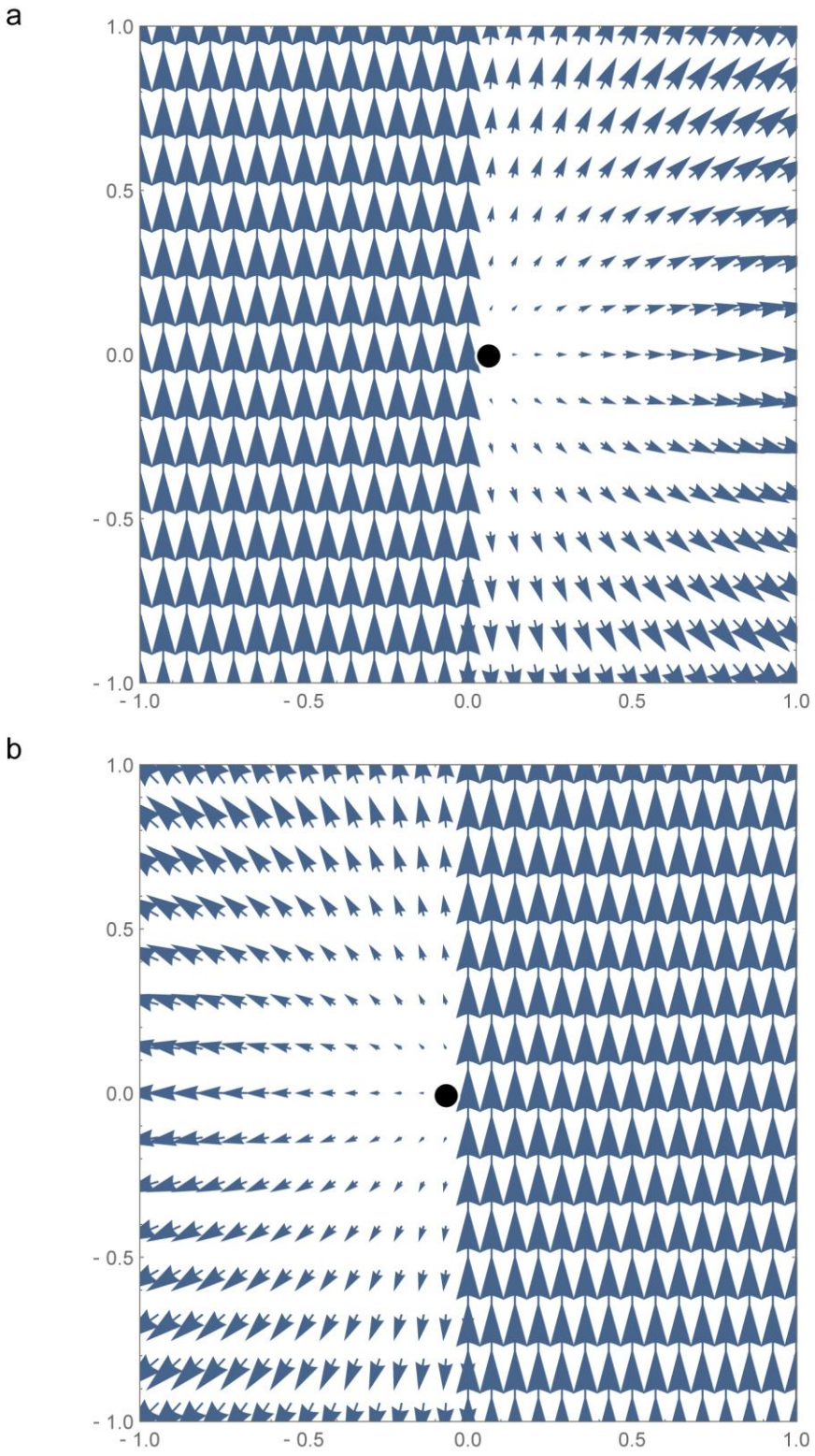


***Figure 4.6 Evanescent tangential eigen states of the Effective Dirac Hamitonian. (a) and (b) show the two degenerate cases.***

## 4.5 Non-triviality analysis of air - DHM system in momentum space

In order to understand the topological behavior of our effective material design, we now show how transforming an isotropic system to a double hyperbolic system results in a new topological phase. The evolution of the equi-frequency contours (EFCs) and analysis is shown in ***Figure 4.7***.

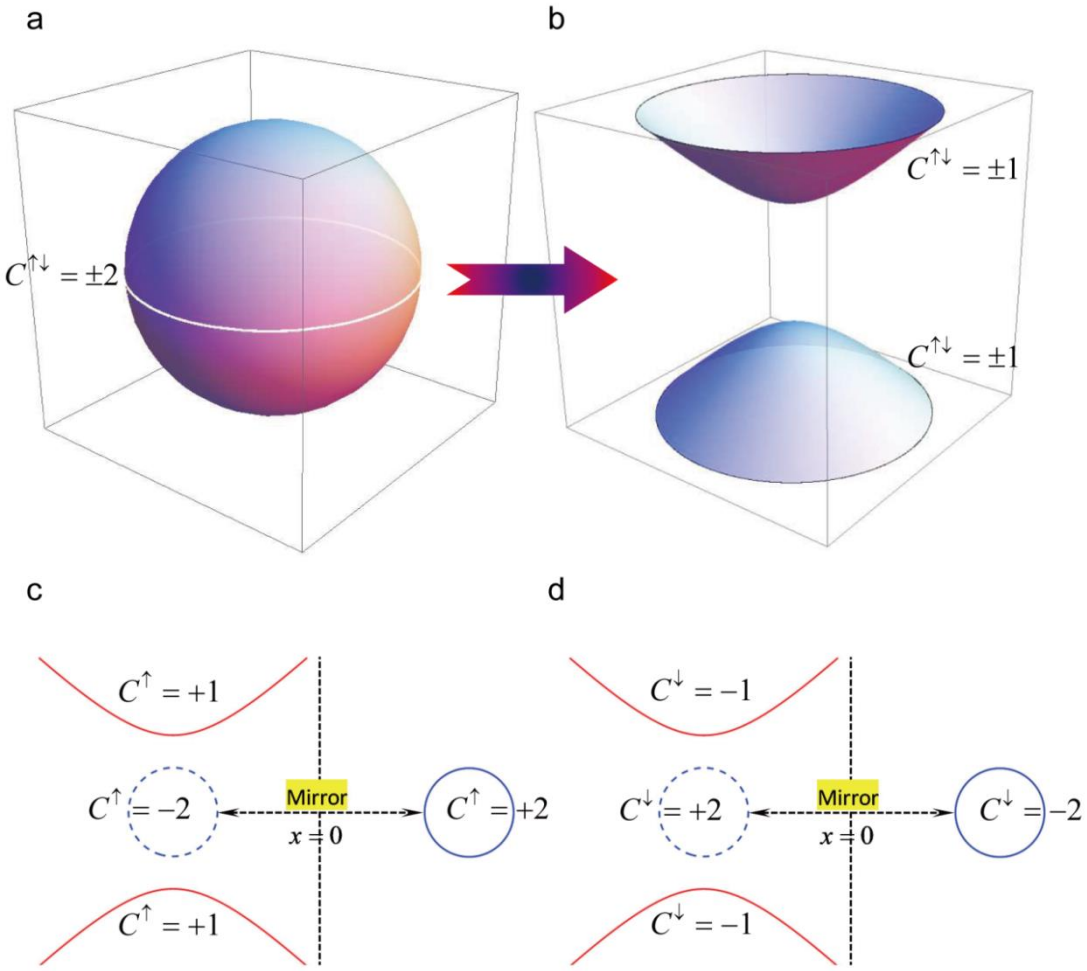


***Figure 4.7 EFCs transformation from air to degenerate DHM and mirror***

***operation.***

(a) *k*-sphere of air. (b) EFCs transformation from air to degenerate DHM. The spin Chern numbers are split into $\pm 1$. Obviously, a *k* space gap has been opened through this deformation, which is a necessary condition for Fermi arc like surface states. (c) , (d) Mirror operation with respect of x=0 plane flips the spin Chern numbers in *k* space.

For a transition from air to DHM with electromagnetic duality, the k-sphere is cut open along the equator into two sheets (***Figure 4.7***a), and the Gaussian curvatures of the two sheets are flipped, transforming into a degenerate two-sheet hyperboloid (***Figure 4.7***b). Consequently, the Chern numbers are equally split into half for each sheet as +1 and -1 for different helicity of light (***Figure 4.7***b). A degenerate DHM exhibits a distinct topological feature from that of air, both of which can be considered as metallic states for photons. As the dual symmetry between $\ddot{\varepsilon}$ and $\ddot{\mu}$ is preserved in both media, at the interface formed between these two media, the two spin states do not interact with each other and therefore the system can be considered to be two separate copies of spin states. Thus, we can separately analyse the surface states at the interface for each spin. For LCP, the EFCs across the interface show distinct topological features, with two hyperbolic sheets with Chern number of +1 on one side, and a sphere EFC with Chern number of +2 on the other side.

When analysing the system, one interesting point to note is that the LCP and RCP are mutually mirror partners, so the upper configuration setting can be seen as a mirror operation and just flipped the corresponding Chern numbers (***Figure 4.7***c and d). In

other words, for the global LCP or RCP, there should be a topological phase transition across the interface although the sum of Chern numbers vanishes.

## 4.6 Properties and analytical solution of the nontrivial surface states

Considering the more general effective medium with $\ddot{\varepsilon} = \ddot{\mu}/\eta = diag\{\alpha, \alpha, \beta\}$, where $\alpha > 0, \beta \le 0$, the EFCs of DHM can be expressed as,

$$\alpha\left(k_x^2 + k_y^2\right) + \beta(k_z^2 - \alpha^2\eta) = 0 \qquad [4\text{-}10]$$

where for simplicity, $\vec{k}$ is the wave vector normalized by $k_0 = \omega / c$.

Next we investigate the Fermi arc like surface states supported by the interface between an arbitrary isotropic medium $\ddot{\varepsilon} = \ddot{\mu} / \eta = \xi$ and the DHM. By assuming that the surface wave exponentially decays from the interface along both directions (i.e., the half space $x>0$ is occupied by isotropic medium and the half space $x<0$ is occupied by DHM), we follow the method [78] developed by Dyakonov in 1988 to calculate the nontrivial surface wave. The surface wave propagates along $\vec{q}$ direction which forms an angle $tan\varphi = k_y / k_z$ with the $z$ axis. We define a local coordinate $\hat{x}' = \hat{x}, \hat{y}' = 0, z' = \hat{q}$ for solving the dispersion relation of the surface states.

In the isotropic medium, the two orthogonal eigen modes (TE and TM) can be

expressed as,

$$\begin{bmatrix} E_1 & H_1 \\ E_2 & H_2 \end{bmatrix} = \begin{bmatrix} 0 & \eta\xi & 0 & -q & 0 & ik_x^{iso} \\ -iqk_x^{iso}/\xi & 0 & \eta\xi - q^2/\xi & 0 & -ik_x^{iso} & 0 \end{bmatrix} \quad [4\text{-}11]$$

where $k_x^{iso} = \sqrt{q^2 - \xi^2\eta} > 0$ represents the decay constant along $+x$ direction. Similarly, two eigen states of DHM side can be expressed as,

$$\begin{bmatrix} E_3 & H_3 \\ E_4 & H_4 \end{bmatrix} = \begin{bmatrix} 0 & \eta C_1 & \eta C_2 & -qC_1/\alpha & 0 & -ik_x^{DHM} \\ iqk_x^{DHM}/\alpha & \eta C_2 & \eta C_1' - q^2/\alpha & -qC_2/\alpha & ik_x^{DHM} & 0 \end{bmatrix} \quad [4\text{-}12]$$

where $k_x^{DHM} = \sqrt{q^2\left[\sin^2\varphi + (\beta/\alpha)\cos^2\varphi\right] - \alpha\beta\eta} > 0$ is the decay constant in the DHM side, and the three effective parameters $C_1$, $C_1'$ and $C_2$ are defined as,

$$\begin{aligned} C_1 &= \alpha\sin^2\varphi + \beta\cos^2\varphi \\ C_1' &= \alpha\cos^2\varphi + \beta\sin^2\varphi \\ C_2 &= (\alpha - \beta)\sin\varphi\cos\varphi \end{aligned} \quad [4\text{-}13]$$

The tangential components of these fields are continuous across the interface, leading to the determinant problem of a 4×4 constraint matrix $M$,

$$det[M] = \begin{vmatrix} \eta\xi & 0 & \eta C_1 & \eta C_2 \\ 0 & \eta\xi - q^2/\xi & \eta C_2 & \eta C_1' - q^2/\alpha \\ 0 & -ik_x^{iso} & 0 & ik_x^{DHM} \\ ik_x^{iso} & 0 & -ik_x^{DHM} & 0 \end{vmatrix} = 0 \quad [4\text{-}14]$$

which can be simplified as,

$$\left(\xi k_x^{iso} + \alpha k_x^{DHM}\right)^2 = \eta\left(\alpha^2 - \xi^2\right)\left(\xi^2 - \alpha\beta\right) = const \qquad [4\text{-}15]$$

Interestingly, these surface states can be expressed as four straight tangent line segments (exactly linear dispersion relation in $k$ space),

$$k_z = \pm\frac{\sqrt{\alpha^2 - \xi^2}}{\sqrt{\xi^2 - \alpha\beta}} k_y \pm \frac{\sqrt{\alpha^2 - \alpha\beta}}{\sqrt{\xi^2 - \alpha\beta}} \xi\sqrt{\eta} \qquad [4\text{-}16]$$

whose lengths are related to the total decay constant located in both sides.

$$\Delta = \Delta_1 + \Delta_2 = k_x^{iso} + \frac{\alpha k_x^{DHM}}{\xi} \qquad [4\text{-}17]$$

The corresponding total penetration depth

$$d^{iso} + d^{DHM} = \frac{k_x^{iso} + k_x^{DHM}}{k_x^{iso} k_x^{DHM}} \qquad [4\text{-}18]$$

has a minimum value of $2 / k_x^{iso}$ when $k_x^{iso} = k_x^{DHM}$, which means that under this condition the surface states are the most confined to the interface [79]. When either $k_x^{iso}$ or $k_x^{DHM}$ goes to zero, the surface states have infinite penetration depth into the isotropic surrounding medium or the DHM, and therefore they are merging into the bulk surface of the respective media.

Now we assume $\left(Ak_x^{DHM}, Bk_x^{DHM}, Ak_x^{iso}, Bk_x^{iso}\right)$ is a nonzero set of solution for the matrix

*M*, we can further reduce the order of the matrix, leading to a symmetric 2×2 matrix,

$$\begin{bmatrix} \eta\left(k_x^{iso}C_1 + k_x^{DHM}\xi\right) & \eta k_x^{iso}C_2 \\ \eta k_x^{iso}C_2 & k_x^{iso}(\eta C_1' - q^2/\alpha) + k_x^{DHM}\left(\eta\xi - q^2/\xi\right) \end{bmatrix} \begin{bmatrix} A \\ B \end{bmatrix} = 0 \qquad [4\text{-}19]$$

where,

$$\frac{A}{B} = -\frac{k_x^{iso}C_2}{k_x^{iso}C_1 + k_x^{DHM}\xi} \qquad [4\text{-}20]$$

is the ratio between the two independent eigen-states (i.e., $AE_1 + BE_2 = E_{surf}^{iso}$) forming the surface mode. Thus we can obtain the electric and magnetic fields and finally the following relationship between the Poynting vectors in the DHM and the surrounding medium $\vec{S}^{DHM} = \frac{\xi}{\alpha}\vec{S}^{iso}$.

Considering the properties of topological surface states at the interface between air and a DHM with $\alpha = 3, \beta = -2.5, \eta = 1$, the corresponding bulk and chiral surface states as plotted in ***Figure 4.8***a. An arbitrary wave vector $\vec{q}$ on the "Fermi arc" divides the it into two line segments whose lengths are related to the decay constant in air and in the DHM by $\Delta_1 = k_x^{iso}$ and $\Delta_2 = \alpha k_x^{DHM}/\xi$. Due to exact linear dispersion of the "Fermi arc", the group velocities of the surface states point to the same direction.

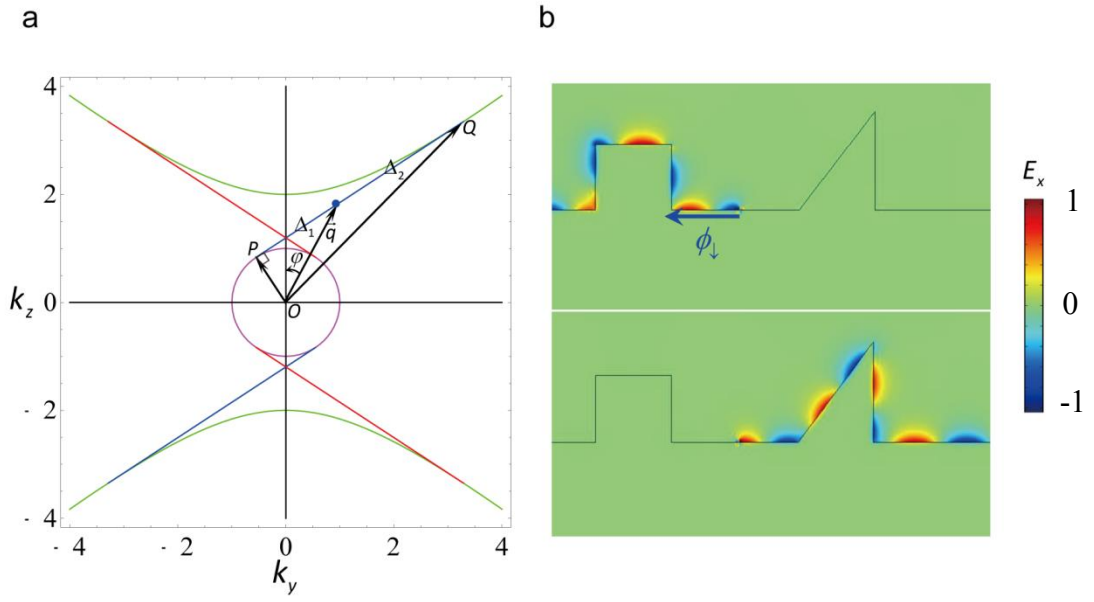


***Figure 4.8 Exhibition of linear Fermi arc like surface states.***
(a) Bulk and surface states in k space. Green line and the middle circle represent EFCs of DHM and air, respectively. The gapless Fermi arc like surface states colored with red (spin-up) and blue (spin-down) manifest the topology of this system. Spin up/down states are shown in the inset with local RCP/LCP definition related to energy propagating directions $S_z/S_y$=-*cotθ* for spin-down surface state. (b) Simulation of pseudo spin-up surface mode and spin-down surface mode with $k_z$ = *1.1* in 2D Comsol frequency domain.

According to the boundary condition it is easy to get that the electric field of the surface state presents strictly circular and elliptical (with ellipticity $\sqrt{\xi/\alpha}$) polarization in air and DHM side, respectively. The nontrivial surface wave supported by such an interface is investigated by full wave simulation software-COMSOL in the frequency domain for a fixed out-plane wave vector ($k_z$). Two orthogonally arranged electric dipoles with a phase difference of $\pi/2$ are used to excite the two chiral spin-up (RCP) and spin-down (LCP) surface states. ***Figure 4.8***b shows backscattering immune transportation of

spin-dependent surface states to any z-invariant disorders as long as time reversal and inversion symmetry are present.

## 4.7 Realistic metamaterial design

Having outlined the realization of Dirac point in metamaterials based on their effective parameters, we now demonstrate the experimental feasibility of our scheme by designing a realistic metamaterial structure. To simultaneously realize the required permittivity and permeability dispersion along *z* direction, we apply metallic helixes as shown in ***Figure 4.9***a, where two mirrored helixes along *z* direction (clockwise and anticlockwise rotated helix-pair) to introduce both electric and magnetic resonances along z direction, while eliminating the chiral response. In the *x*-*y* plane, we apply $C_4$ rotation symmetry to achieve in -plane isotropic electromagnetic response. Thus, each unit cell consists of eight helixes in total. By tuning the geometric parameters of the structure, such as radius *R*, height *h*, period *P* along x/y direction and $p_z$ along z direction, the dispersion of $\varepsilon_z$ and $\mu_z$ can be adjusted leading to the degeneracy of the two longitudinal modes. In the microwave regime, the designed Dirac metamaterial can be readily fabricated [36,80]. ***Figure 4.9***b and c present the dispersion curves of the bulk states of the proposed metamaterial along z and y directions, respectively. The presence of a four-fold crossing between two degenerate longitudinal modes and two degenerate transverse modes is observed.

The metamaterial design should support topology protected photonic surface states. To confirm this, a supercell calculation involving 20 metamaterial unit-cell sandwiched between air is performed. ***Figure*** 4.9d shows two 'Fermi arc' like surface states as expected. Its localization on the interface between the metamaterial and air is presented in ***Figure 4.10***(a). However, their impedances (the retrieved parameters [81] of the metamaterial at Dirac point frequency is $\alpha = 3.8, \beta = 0, \eta = 1/3.8$ as shown in ***Figure 4.10***d is not matched in fact. So the surface state wave propagation is not scattering-immune around corner of the cuboid as shown in ***Figure 4.10***b. In contrast, ***Figure 4.10***c shows spin dependent one way propogation when the system is impedance matched.

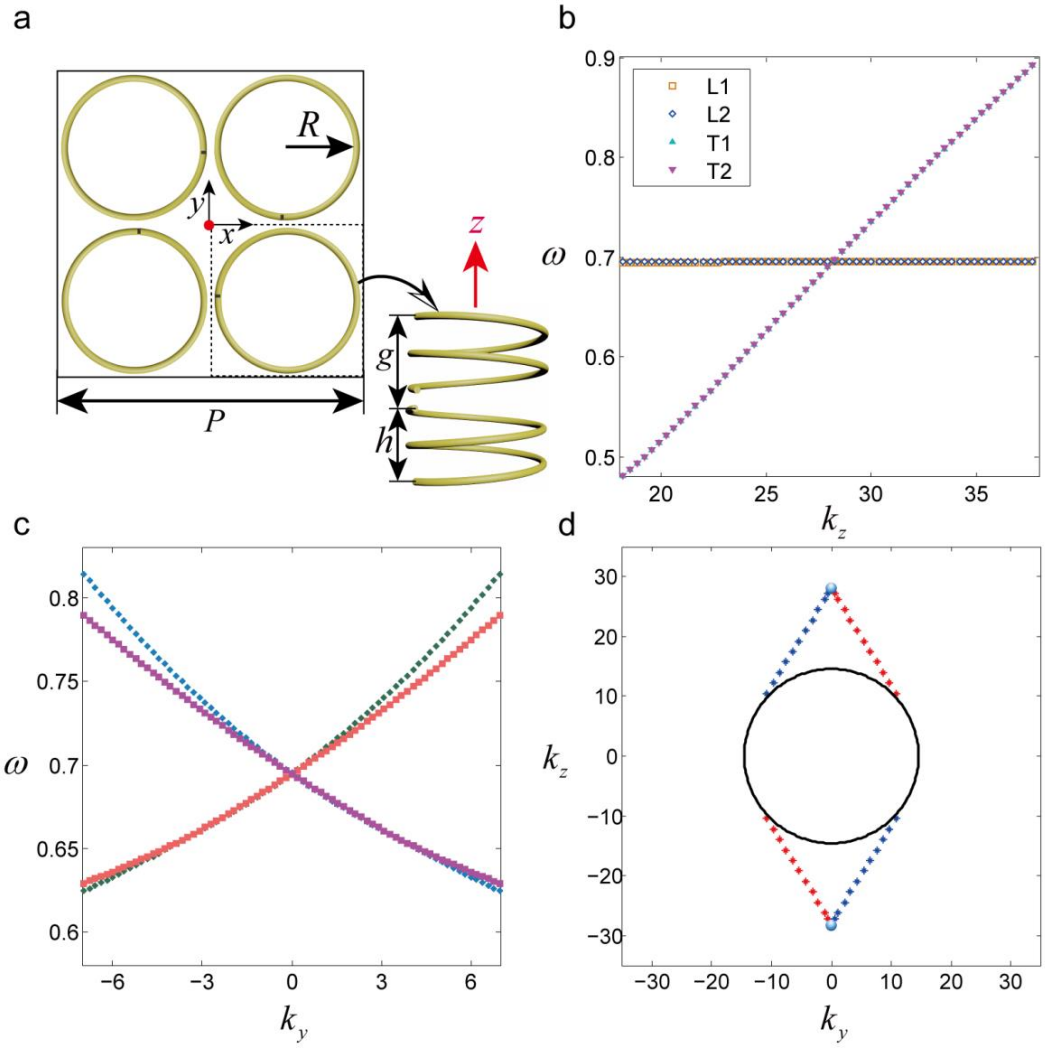


***Figure 4.9 Dirac points with realistic metamaterial structure.***

(a) The metamaterial structure with top view of one unit cell composed with $C_4$ symmetry distributed helix-pairs, and the front view of a pair of mirrored helixes with opposite rotation direction with parameters $R=20$mm, $p_x=p_y=P=90mm$, $p_z=50mm$, $g=20mm$, $h=25mm$. (b) and (c) are the simulated band structure of the metamaterial along $k_z$ and $k_y$ direction respectively. (d). Surface state dispersion at Dirac poin frequency (0.695GHz).

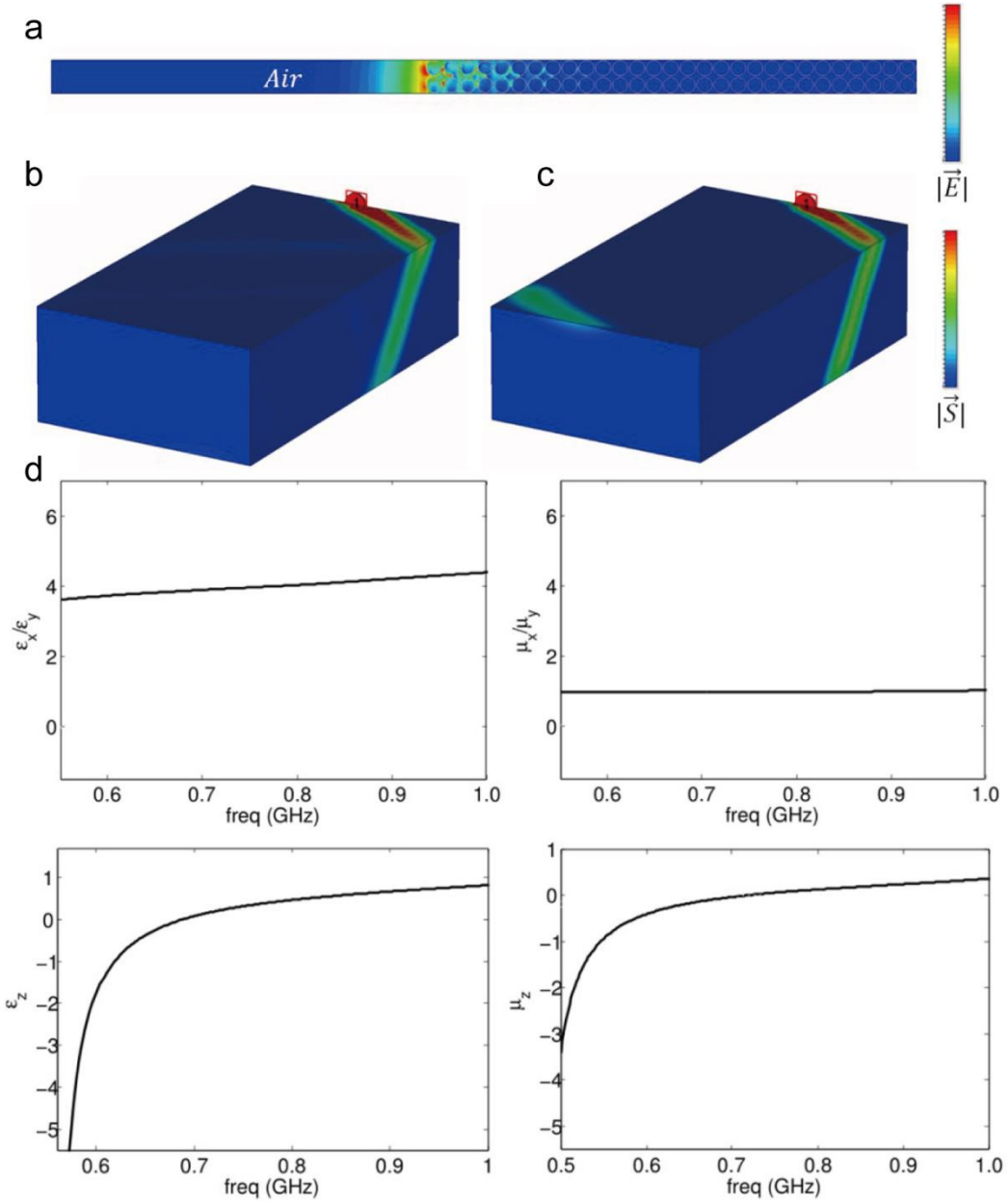


***Figure 4.10 Surface state confinement and scattering.***

(a) Surface state E-field patterns at the interface between air and the metamaterial with respect of $k_y = 33.4m^{-1}$, $k_z = 50m^{-1}$ and frequency=0.695GHz, (b) 3D surface state between air and the Dirac metamaterial simulated from CST with the effective permittivity and permeability ( $\alpha = 3.8, \beta = 0, \eta = 1/3.8$ ) retrieved from the real metamaterial structures. (c) similar to (b) but with impedance matched surrounding medium ( $\alpha = 1.8, \beta = 0, \eta = 1/3.8$ ). (d) Retrieved effective parameters of the realistic metamaterial for reference.

## 4.8 Conclusion

By considering electromagnetic duality symmetry, we theoretically proposed the realization of photonic Dirac degeneracy and spin-dependent Fermi arc like surface states. This theoretical model is of great importance in understanding fundamental topological photonics, such as exhibiting transition from $Z_2$ topological insulator to Weyl degeneracies [5]. Furthermore, the fundamental link between photonic Dirac points and vector/vortex optics has been established through optical reflection with in-plane momentum matching the Dirac points.

# Chapter 5. Conclusion and future work

Topological phases have renewed our understanding upon physics. With exotic topological responses, large amount of applications are very promising. For example, robust surface/edge states without any back-scattering provide us a dissipationless information channel. In photonics, topological photonics offers a new degree in manipulating electromagnetic wave. So far, topological phases are classified into two main classes: topological gapless phases and topological gapped phases. In this thesis, we mainly focus on photonic topological gapless phase realization based on the metamaterials approach. Described by an effective model, it is relatively simple in the designs and realizations of different topological phases. Without the constraints of high dielectric-constant and strict periodicity, as required in photonic crystals, it is also more feasible to be fabricated and assembled. Furthermore, owing to the advantage of deep sub-wavelength in metamaterials, surface waves are usually well-confined on the interface. Thus, near-field scanning greatly facilitates the measurements and discoveries of novel surface states in various topological photonic metamaterials. Although metallic elements are very lossy in the optical band, the same design can be transferred to terahertz system, where a nonmagnetic terahertz topological surface-state arcs can be observed.

Different from dielectrics, metallic structures with bounded current irradiating electromagnetic field have intuitive connection with atomic orbitals in condensed matter. Most of topological condensed matter proposal can be transferred into photonics following the shape and symmetry of underlying individual bonds through tight-binding analysis. Furthermore, the development of vectorial maximally localized Wannier function in 3D photonic crystal can provide a theoretical support and promote these implementations [82]. In addition, meta-crystal shows advanced concepts regarding photonic topological phase realizations due to strong light-matter interaction within resonant metallic structures, and thus an excess of spatial symmetry analysis is omitted. Through this meta-crystal platform, a new wave of experimental activities in topological photonics arises.

Topological gapless phase bridges topological trivial and nontrivial insulator phase. When a Weyl nodes migrate across FBZ and annihilate with opposite chirality partners in pairwise fashion, distinct topological phases occur, such as photonic topological Dirac phase and photonic topological insulator [83].

Especially, ideal Weyl systems can introduce some interesting physics/phenomena as listed below:

1. As all the four Weyl points occur at the same frequency, the density of states

(DOS) strictly approaches zero at the Weyl frequency. This leads to many interesting DOS governed optical phenomena such as spontaneous emission, blackbody radiation, scaling law of resonant scattering, and some interesting physics related to zero index material.

2. The demonstrated ideal Weyl system leads to the first observation of the helicoid surface state ever in both condensed matter and optical systems. The helicoid surface state spinning around each Weyl point represents one of the most striking manifestations of the chiral nature of the Weyl nodes.

3. All the Weyl points in our ideal Wey system are well separated in the momentum space, meaning that the Fermi arcs are very long. Slightly above the Weyl frequencies, the Fermi arcs are very straight. These features lead to nearly diffraction-less propagation of the surface wave, which are very beneficial for many applications.

4. Again, due to the large separation between the Weyl nodes of opposite chirality, the Weyl nodes are extremely robust and cannot be easily annihilated by the imperfection of the structures.

5. The ideal Weyl systems provide a new platform for studying all angle negative refraction without requiring negative permittivity and negative permeability.

Beyond the traditional classification preserving Lorentz symmetry, the realizations of other topological gapless phases using the meta-crystal configuration, such as spin-1 Weyl point [40,41], are very promising.

In addition, other topological systems also attract much attention very recently, such as non-Hermitian, disordered and nonlinear topological phases.

# Appendix

## A.1 Berry phase calculation

Considering a non-reciprocal, uniaxial, chiral medium with,

$$\vec{\vec{\varepsilon}}=\begin{bmatrix} \alpha & i\delta & \\ -i\delta & \alpha & \\ & & \beta \end{bmatrix}, \mu = 1, \gamma = 1, \begin{cases} \vec{D} = \vec{\vec{\varepsilon}}\vec{E} + i\vec{\vec{\gamma}}\vec{H} \\ \vec{B} = \vec{\vec{\mu}}\vec{H} - i\vec{\vec{\gamma}}\vec{E} \end{cases} \qquad [6\text{-}1]$$

By solving Maxwell's equations with harmonic space and time dependence, $\vec{E}, \vec{H} \to \vec{E}, \vec{H}e^{i\left(\vec{k}\cdot\vec{r}-\omega t\right)}$ for this set of material parameters, the polarization eigen-states and corresponding dispersion relations $\omega\left(k_x, k_y, k_z\right)$ can be found. At a fixed frequency a set of k-surfaces can thus be defined, describing the directional dependence of the allowed propagating modes.

The topological properties of surface states can be investigated by calculating the geometric (or Berry) phase accumulated upon traversing a closed path in *k* space.

$$\phi_B = i\oint \vec{A}_k \cdot d\vec{k} \qquad [6\text{-}2]$$

in which,

$$A_l = \frac{\begin{bmatrix} \vec{E}^* & \vec{H}^* \end{bmatrix} \vec{\vec{B}} \nabla_l \begin{bmatrix} \vec{E} \\ \vec{H} \end{bmatrix}}{\begin{bmatrix} \vec{E}^* & \vec{H}^* \end{bmatrix} \vec{\vec{B}} \begin{bmatrix} \vec{E} \\ \vec{H} \end{bmatrix}}, l = x, y, z, \qquad [6\text{-}3]$$

and,

$$\vec{\vec{B}} = \frac{\partial}{\partial \omega}\left[\omega \begin{pmatrix} \vec{\vec{\varepsilon}} & i\gamma \\ -i\gamma & 1 \end{pmatrix}\right]. \qquad [6\text{-}4]$$

Working in cylindrical coordinates and looping around $k_\varphi$, for fixed $k_z$ and $k_r$, Berry phase can be written as,

$$\phi_B = i\oint \frac{\begin{bmatrix} \vec{E}^* & \vec{H}^* \end{bmatrix} \vec{\vec{B}} \nabla_\varphi \begin{bmatrix} \vec{E} \\ \vec{H} \end{bmatrix}}{\begin{bmatrix} \vec{E}^* & \vec{H}^* \end{bmatrix} \vec{\vec{B}} \begin{bmatrix} \vec{E} \\ \vec{H} \end{bmatrix}} \cdot dk_\varphi \qquad [6\text{-}5]$$

where, due to the cylindrical symmetry of the problem,

$$\begin{bmatrix} \vec{E} \\ \vec{H} \end{bmatrix} = \begin{bmatrix} E_r \cos\varphi - E_\varphi \sin\varphi & E_r \sin\varphi + E_\varphi \cos\varphi & E_z \\ H_r \cos\varphi - H_\varphi \sin\varphi & H_r \sin\varphi + H_\varphi \cos\varphi & H_z \end{bmatrix} \qquad [6\text{-}6]$$

with,

$$\begin{bmatrix} E_r \\ H_r \end{bmatrix} = \begin{bmatrix} E_y \\ H_y \end{bmatrix}, \begin{bmatrix} E_\varphi \\ H_\varphi \end{bmatrix} = -\begin{bmatrix} E_x \\ H_x \end{bmatrix}, \begin{bmatrix} E_z \\ H_z \end{bmatrix} = \begin{bmatrix} E_z \\ H_z \end{bmatrix} \left(k_x = 0\right) \qquad [6\text{-}7]$$

## A.2 Calculation of surface states [78]

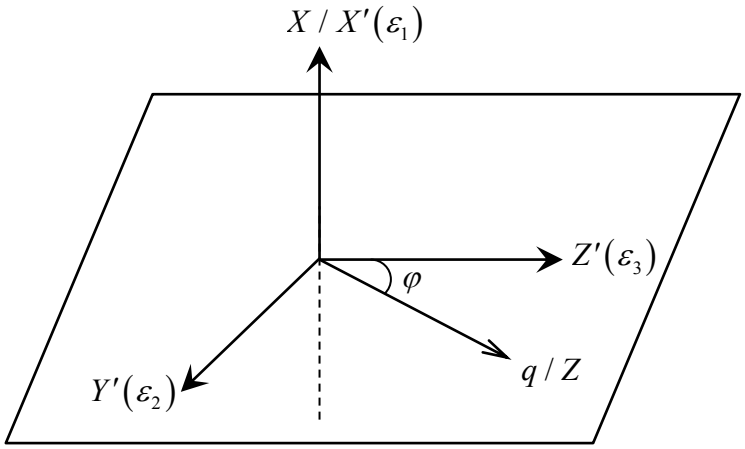


First we solve Maxwell equations in the form of a monochromatic wave travelling along the $Y'OZ'$ plane and characterized by a wave vector $\vec{q}$, this wave decays along the X axis in either direction away from the interface. The half space X>0 is occupied by the isotropic medium, whereas the designed homogeneous medium is in the half space X<0. In the isotropic medium, there are two independent solutions with different polarizations and with the wave vector $\vec{q}_1 = (ik_1, 0, q)$, where,

$$q^2 - k_1^2 = \omega^2 \varepsilon \mu \qquad [6\text{-}8]$$

The two independent solutions will be assumed to represent TM and TE waves:

TE:

$$\begin{cases} \vec{E} = (0,1,0) \\ \vec{H} = (-q,0,ik_1) \end{cases} \qquad [6\text{-}9]$$

TM:

$$\begin{cases} \vec{E} = (q, 0, -ik_1) \\ \vec{H} = (0, \varepsilon, 0) \end{cases} \quad [6\text{-}10]$$

$k_1$ should be positive and real here.

In the designed homogeneous medium, two independent solutions have the wave vectors,

$$\begin{cases} \vec{q}_2 = (-ik_2, 0, q) \\ \vec{q}_3 = (-ik_3, 0, q) \end{cases} \quad [6\text{-}11]$$

And by deducing Maxwell Equation,

$$\nabla \times \left( \ddot{\mu}^{-1} \nabla \times \vec{E} \right) - \omega \nabla \times \left( \ddot{\mu}^{-1} \ddot{\gamma} \vec{E} \right) - \omega^2 \ddot{\varepsilon} \vec{E} - \omega \ddot{\gamma} \ddot{\mu}^{-1} \nabla \times \vec{E} + \omega^2 \ddot{\gamma} \ddot{\mu}^{-1} \ddot{\gamma} \vec{E} = 0 \quad [6\text{-}12]$$

To guarantee Eq.[6-12] contains non-zero solutions,

$$\ddot{M} \vec{E} = 0, \det(\ddot{M}) = 0 \quad [6\text{-}13]$$

From this Eq.[6-13], we could get $k_2$ and $k_3$. By substituting them to Eq.[6-9], Eq.[6-10] and Eq.[6-13], we get $\vec{E}$.

The relationship between $\vec{H}$ and $\vec{E}$,

$$\vec{H} = \frac{-i}{\omega} \ddot{\mu}^{-1} \nabla \times \vec{E} + i \ddot{\mu}^{-1} \ddot{\gamma} \vec{E} \quad [6\text{-}14]$$

We shall now find linear combinations of the solutions for X<0 and of the ones for X>0, and we shall postulate that the tangential components of the fields $\vec{E}$ and $\vec{H}$ are continuous at the interface. This gives the equation,

$$\det \begin{bmatrix} E_{1y} & E_{2y} & E_{3y} & E_{4y} \\ E_{1z} & E_{2z} & E_{3z} & E_{4z} \\ H_{1y} & H_{2y} & H_{3y} & H_{4y} \\ \underbrace{H_{1z}}_{x<0} & \underbrace{H_{2z}}_{x<0} & \underbrace{H_{3z}}_{x>0} & \underbrace{H_{4z}}_{x>0} \end{bmatrix} = 0 \quad [6\text{-}15]$$

From Eq.[6-15], we can get the relation between $q$ and $\varphi$ . Transform them to rectangular base,

$$\begin{cases} k_{Y'} = q\sin\varphi \\ k_{Z'} = q\cos\varphi \end{cases} \qquad [6\text{-}16]$$

Finally, edge states of *k*-space have been calculated.

# Reference

[1] Xiao, D., Chang, M. C. & Niu, Q. Berry phase effects on electronic properties. *Rev. Mod. Phys.* **82**, 1959 (2010).

[2] Hasan, M. Z. & Kane, C. L. Colloquium: Topological insulators. *Rev. Mod. Phys.* **82**, 3045-3067 (2010).

[3] Qi, X.-L. & Zhang, S.-C. Topological insulators and superconductors. *Rev. Mod. Phys.* **83**, 1057-1110 (2011).

[4] Chiu, C.-K., Teo, J. C. Y., Schnyder, A. P. & Ryu, S. Classification of topological quantum matter with symmetries. *Reviews of Modern Physics* **88**, 035005 (2016).

[5] Armitage, N. P., Mele, E. J. & Vishwanath, A. Weyl and Dirac Semimetals in Three Dimensional Solids. *arXiv:1705.01111 [cond-mat.str-el]* (2017).

[6] Kane, C. L. & Mele, E. J. Z2 Topological Order and the Quantum Spin Hall Effect. *Phys. Rev. Lett.* **95**, 146802 (2005).

[7] Kane, C. L. & Mele, E. J. Quantum Spin Hall Effect in Graphene. *Phys. Rev. Lett.* **95**, 226801 (2005).

[8] Fu, L., Kane, C. L. & Mele, E. J. Topological Insulators in Three Dimensions. *Physical Review Letters* **98**, 106803 (2007).

[9] Wang, Z., Alexandradinata, A., Cava, R. J. & Bernevig, B. A. Hourglass fermions. *Nature* **532**, 189-194 (2016).

[10] Dong, X.-Y. & Liu, C.-X. Classification of topological crystalline insulators based on representation theory. *Physical Review B* **93**, 045429 (2016).

[11] Schnyder, A. P., Ryu, S., Furusaki, A. & Ludwig, A. W. W. Classification of topological insulators and superconductors in three spatial dimensions. *Phys. Rev. B* **78**, 195125 (2008).

[12] Fruchart, M. & Carpentier, D. An introduction to topological insulators. *Comptes Rendus Physique* **14**, 779-815 (2013).

[13] Wan, X., Turner, A. M., Vishwanath, A. & Savrasov, S. Y. Topological semimetal and Fermi-arc surface states in the electronic structure of pyrochlore iridates. *Physical Review B* **83**, 205101 (2011).

[14] Burkov, A. A. & Balents, L. Weyl Semimetal in a Topological Insulator Multilayer. *Phys. Rev. Lett.* **107**, 127205 (2011).

[15] Xu, G., Weng, H., Wang, Z., Dai, X. & Fang, Z. Chern Semimetal and the Quantized Anomalous Hall Effect in $HgCr_2Se_4$. *Phys. Rev. Lett.* **107**, 186806 (2011).

[16] Haldane, F. D. M. & Raghu, S. Possible Realization of Directional Optical Waveguides in Photonic Crystals with Broken Time-Reversal Symmetry. *arXiv:cond-mat/0503588 [cond-mat.mes-hall]* (2005).

[17] Haldane, F. D. M. & Raghu, S. Possible Realization of Directional Optical Waveguides in Photonic Crystals with Broken Time-Reversal Symmetry. *Phys. Rev. Lett.* **100**, 013904 (2008).

[18] Wang, Z., Chong, Y. D., Joannopoulos, J. D. & Soljačić, M. Reflection-Free One-Way Edge Modes in a Gyromagnetic Photonic Crystal. *Phys. Rev. Lett.* **100**, 013905 (2008).

[19] Wang, Z., Chong, Y., Joannopoulos, J. D. & Soljacic, M. Observation of unidirectional backscattering-immune topological electromagnetic states. *Nature* **461**, 772-775 (2009).

[20] Lu, L., Joannopoulos, J. D. & Soljacic, M. Topological photonics. *Nat. Photonics* **8**, 821-829 (2014).

[21] Poo, Y., Wu, R.-x., Lin, Z., Yang, Y. & Chan, C. T. Experimental Realization of Self-Guiding Unidirectional Electromagnetic Edge States. *Phys. Rev. Lett.* **106**, 093903 (2011).

[22] Khanikaev, A. B. *et al.* Photonic topological insulators. *Nat. Mater.* **12**, 233-239 (2013).

[23] Wu, L.-H. & Hu, X. Scheme for Achieving a Topological Photonic Crystal by Using Dielectric Material. *Physical Review Letters* **114**, 223901 (2015).

[24] He, C. *et al.* Photonic topological insulator with broken time-reversal symmetry. *Proceedings of the National Academy of Sciences* **113**, 4924-4928 (2016).

[25] Chen, W.-J. *et al.* Experimental realization of photonic topological insulator in a uniaxial metacrystal waveguide. *Nat. Commun.* **5** (2014).

[26] Yves, S. *et al.* Crystalline metamaterials for topological properties at

subwavelength scales. **8**, 16023 (2017).

[27] Lu, L., Fu, L., Joannopoulos, J. D. & Soljacic, M. Weyl points and line nodes in gyroid photonic crystals. *Nat. Photon.* **7**, 294-299 (2013).

[28] Lu, L. *et al.* Experimental observation of Weyl points. *Science* **349**, 622-624 (2015).

[29] Chen, W.-J., Xiao, M. & Chan, C. T. Photonic crystals possessing multiple Weyl points and the experimental observation of robust surface states. *Nat. Commun.* **7**, 13038 (2016).

[30] Chang, M.-L., Xiao, M., Chen, W.-J. & Chan, C. T. Multiple Weyl points and the sign change of their topological charges in woodpile photonic crystals. *Physical Review B* **95**, 125136 (2017).

[31] Noh, J. *et al.* Experimental observation of optical Weyl points and Fermi arc-like surface states. *Nat Phys* **13**, 611-617 (2017).

[32] Rechtsman, M. C. *et al.* Photonic Floquet topological insulators. *Nature* **496**, 196-200 (2013).

[33] Gao, W. *et al.* Topological Photonic Phase in Chiral Hyperbolic Metamaterials. *Phys. Rev. Lett.* **114**, 037402 (2015).

[34] Gao, W. *et al.* Photonic Weyl degeneracies in magnetized plasma. *Nat. Commun.* **7**, 12435 (2016).

[35] Xiao, M., Lin, Q. & Fan, S. Hyperbolic Weyl Point in Reciprocal Chiral

Metamaterials. *Phys. Rev. Lett.* **117**, 057401 (2016).

[36] Yang, B. *et al.* Direct observation of topological surface-state arcs in photonic metamaterials. *Nature Communications* **8**, 97 (2017).

[37] Wang, H., Xu, L., Chen, H. & Jiang, J.-H. Three-dimensional photonic Dirac points stabilized by point group symmetry. *Physical Review B* **93**, 235155 (2016).

[38] Wang, H.-X., Chen, Y., Hang, Z. H., Kee, H.-Y. & Jiang, J.-H. Type-II Dirac Photons. *arXiv:1703.09899* (2017).

[39] Qinghua Guo, B. Y., Lingbo Xia, Wenlong Gao, Hongchao Liu, Jing Chen, Yuanjiang Xiang, Shuang Zhang. Three dimensional photonic Dirac points in metamaterials. *arXiv:1706.08173 [physics.optics]* (2017).

[40] Bradlyn, B. *et al.* Beyond Dirac and Weyl fermions: Unconventional quasiparticles in conventional crystals. *Science* (2016).

[41] Lv, B. Q. *et al.* Observation of three-component fermions in the topological semimetal molybdenum phosphide. *Nature* **546**, 627-631 (2017).

[42] Chen, F., Hongming, W., Xi, D. & Zhong, F. Topological nodal line semimetals. *Chinese Physics B* **25**, 117106 (2016).

[43] Lu, L. *et al.* Symmetry-protected topological photonic crystal in three dimensions. *Nat Phys* **12**, 337-340 (2016).

[44] Slobozhanyuk, A. *et al.* Three-dimensional all-dielectric photonic topological insulator. *Nat Photon* **11**, 130-136 (2017).

[45] Ochiai, T. Gapless surface states originated from accidentally degenerate quadratic band touching in a three-dimensional tetragonal photonic crystal. *arXiv:1705.11006 [physics.optics]* (2017).

[46] Mechelen, T. V. & Jacob, Z. Dirac-Maxwell correspondence: Spin-1 bosonic topological insulator. *arXiv:1708.08192 [cond-mat.mes-hall]* (2017).

[47] Yang, B. *et al.* Discovery of ideal Weyl points with helicoid surface states. *arXiv:1709.06065 [cond-mat.mtrl-sci]* (2017).

[48] Liu, Z. K. *et al.* Discovery of a Three-Dimensional Topological Dirac Semimetal, $Na_3Bi$. *Science* **343**, 864 (2014).

[49] He, Q. L. *et al.* Chiral Majorana fermion modes in a quantum anomalous Hall insulator–superconductor structure. *Science* **357**, 294 (2017).

[50] Xu, S.-Y. *et al.* Discovery of a Weyl fermion semimetal and topological Fermi arcs. *Science* **349**, 613 (2015).

[51] Weng, H., Fang, C., Fang, Z., Bernevig, B. A. & Dai, X. Weyl Semimetal Phase in Noncentrosymmetric Transition-Metal Monophosphides. *Phys. Rev. X* **5**, 011029 (2015).

[52] Haldane, F. D. M. Model for a Quantum Hall Effect without Landau Levels: Condensed-Matter Realization of the "Parity Anomaly". *Phys. Rev. Lett.* **61**, 2015-2018 (1988).

[53] Young, S. M. *et al.* Dirac Semimetal in Three Dimensions. *Phys. Rev. Lett.* **108**, 140405 (2012).

[54] Soluyanov, A. A. *et al.* Type-II Weyl semimetals. *Nature* **527**, 495-498 (2015).

[55] Nielsen, H. B. & Ninomiya, M. Absence of neutrinos on a lattice. *Nuclear Physics B* **193**, 173-194 (1981).

[56] Huang, L. *et al.* Spectroscopic evidence for a type II Weyl semimetallic state in MoTe2. *Nature materials* **advance online publication** (2016).

[57] Yang, B., Lawrence, M., Gao, W., Guo, Q. & Zhang, S. One-way helical electromagnetic wave propagation supported by magnetized plasma. *Scientific Reports* **6**, 21461 (2016).

[58] Demetriadou, A. & Pendry, J. B. Taming spatial dispersion in wire metamaterial. *Journal of Physics: Condensed Matter* **20**, 295222 (2008).

[59] Zhang, S. *et al.* Photoinduced handedness switching in terahertz chiral metamolecules. *Nat. Commun.* **3**, 942 (2012).

[60] Zhao, R., Koschny, T. & Soukoulis, C. M. Chiral metamaterials: retrieval of the effective parameters with and without substrate. *Optics Express* **18**, 14553-14567 (2010).

[61] Raman, A. & Fan, S. Photonic Band Structure of Dispersive Metamaterials Formulated as a Hermitian Eigenvalue Problem. *Physical Review Letters* **104**, 087401 (2010).

[62] Wang, L., Jian, S.-K. & Yao, H. Topological photonic crystal with equifrequency Weyl points. *Physical Review A* **93**, 061801 (2016).

[63] Zhou, M. *et al.* Electromagnetic Scattering Laws in Weyl Systems. *arXiv:1705.05059 [physics.optics]* (2017).

[64] Ruan, J. *et al.* Symmetry-protected ideal Weyl semimetal in HgTe-class materials. *Nat Commun* **7** (2016).

[65] Ruan, J. *et al.* Ideal Weyl Semimetals in the Chalcopyrites $CuTlSe_2$, $AgTlTe_2$, $AuTlTe_2$, and $ZnPbAs_2$. *Physical Review Letters* **116**, 226801 (2016).

[66] Fang, C., Lu, L., Liu, J. & Fu, L. Topological semimetals with helicoid surface states. *Nat Phys* **12**, 936-941 (2016).

[67] Guo, Q., Gao, W., Chen, J., Liu, Y. & Zhang, S. Line Degeneracy and Strong Spin-Orbit Coupling of Light with Bulk Bianisotropic Metamaterials. *Physical Review Letters* **115**, 067402 (2015).

[68] Castro Neto, A. H., Guinea, F., Peres, N. M. R., Novoselov, K. S. & Geim, A. K. The electronic properties of graphene. *Reviews of Modern Physics* **81**, 109-162 (2009).

[69] Wakabayashi, K., Takane, Y., Yamamoto, M. & Sigrist, M. Edge effect on electronic transport properties of graphene nanoribbons and presence of perfectly conducting channel. *Carbon* **47**, 124-137 (2009).

[70] Fu, L. Topological Crystalline Insulators. *Physical Review Letters* **106**, 106802 (2011).

[71] Zhang, Y. & Kim, E.-A. Quantum Loop Topography for Machine Learning. *Physical Review Letters* **118**, 216401 (2017).

[72] Shen, Y. *et al.* Deep learning with coherent nanophotonic circuits. *Nat Photon* **11**, 441-446 (2017).

[73] Yang, B.-J. & Nagaosa, N. Classification of stable three-dimensional Dirac semimetals with nontrivial topology. *Nat. Commun.* **5** (2014).

[74] Bradlyn, B. *et al.* Topological quantum chemistry. *Nature* **547**, 298-305 (2017).

[75] Xu, S.-Y. *et al.* Observation of Fermi arc surface states in a topological metal. *Science* **347**, 294-298 (2015).

[76] Bliokh, K. Y., Smirnova, D. & Nori, F. Quantum spin Hall effect of light. *Science* **348**, 1448-1451 (2015).

[77] Dong, J.-W., Chen, X.-D., Zhu, H., Wang, Y. & Zhang, X. Valley photonic crystals for control of spin and topology. *Nature materials* **16**, 298-302 (2017).

[78] Dyakonov, M. I. New type of electromagnetic wave propagating at an interface. *Soviet Physics JETP* **67**, 714-716 (1988).

[79] Wada, M., Murakami, S., Freimuth, F. & Bihlmayer, G. Localized edge states in two-dimensional topological insulators: Ultrathin Bi films. *Physical Review B* **83**, 121310 (2011).

[80] Bingnan, W., Jiangfeng, Z., Thomas, K., Maria, K. & Costas, M. S. Chiral metamaterials: simulations and experiments. *Journal of Optics A: Pure and Applied Optics* **11**, 114003 (2009).

[81] Smith, D. R., Schultz, S., Markoš, P. & Soukoulis, C. M. Determination of effective

permittivity and permeability of metamaterials from reflection and transmission coefficients. *Physical Review B* **65**, 195104 (2002).

[82] Wolff, C., Mack, P. & Busch, K. Generation of Wannier functions for photonic crystals. *Physical Review B* **88**, 075201 (2013).

[83] Huang, S. M. A Weyl Fermion semimetal with surface Fermi arcs in the transition metal monopnictide TaAs class. *Nat. Commun.* **6**, 7373 (2015).